UNIVERSITÀ DEGLI STUDI DI MESSINA

DIPARTIMENTO DI SCIENZE MATEMATICHE E INFORMATICHE, SCIENZE FISICHE
E SCIENZE DELLA TERRA
PHYS-03/A

Maria Laura Amoruso

Superconducting Thin Films for Magnetic Confinement Fusion: Growth, Electrical and TEM Microstructural Characterization, with Insights into Ion Irradiation

PhD Cordinator:
Prof. Salvatore Savasta

Tutor:
Prof. Fortunato Neri
Dott. Mario Scuderi
Dott. Antonio Trotta

Accademic Year 2024-2025

(XXXVIII Cycle)

“Le microscope électronique est une fenêtre
ouverte sur les structures et les formes qui
composent le monde invisible à l'œil nu”

(Pierre-Gilles de Gennes)

INDEX

ABSTRACT

The ongoing climate and energy crisis has made it urgent to identify new renewable energy sources capable of replacing non-renewables while minimizing environmental impact. For this reason, the development and research of new superconducting materials for fusion applications are currently of great relevance.

Among renewable alternatives, nuclear fusion energy stands out for its high energy yield and the absence of long-lived radioactive waste. In a fusion reactor, the nuclei of two atoms fuse to form the nucleus of a new element, releasing energy and free neutrons; unlike the waste produced in fission processes, these neutrons are not toxic to the environment or to living organisms. However, the realization of fusion plants capable of meeting global energy demand remains a complex challenge, both from an economic-logistical and engineering perspective.

In this context, Italy plays a leading role, in line with other countries contributing to the advancement of nuclear fusion: at the national level, research institutions (INFN, CNR, ENEA, universities) and private entities (such as Eni), through the EUROfusion consortium, are conducting advanced studies on magnetic confinement reactors and are actively involved in major European projects. Furthermore, one of the key facilities in the European fusion roadmap—the Divertor Tokamak Test facility

(DTT)—is currently under construction at the ENEA Research Center in Frascati.

Among the various experimental magnetic confinement reactors currently under study, one of the most well-known is the "Tokamak"[1]. with a main magnetic field in a toroidal geometry. However, the superconducting coil materials in a Tokamak are exposed to intense radiation: damage levels of 25 dpa/FPY (displacements per atom per full power year) from fast neutrons are expected inside the chamber, making it essential to thoroughly study the effects of such irradiation on superconducting materials. This is crucial to minimizing neutron-induced degradation and ensuring the long-term efficiency of the reactor [2].

Within the group of the materials potentially suitable for this purpose, the various known families of superconductors differ in multiple properties. However, these materials must meet a series of specific requirements, including the ability to carry high currents in the presence of strong magnetic fields, mechanical strength, long-term stability, and low energy losses. From a practical standpoint, the main challenge in the application of superconducting materials lies not only in achieving a higher critical temperature (T_c) but also in maximizing the critical current density (J_c). This condition is governed by extrinsic defects in the material, which result both from the growth technique and from the existence or introduction of defects within the material itself.

Currently, superconducting magnets for fusion plants still employ conventional low-temperature superconductors (LTS), although high-temperature superconductors (HTS) are becoming a promising alternative thanks to the development of coated conductors (CCs). [3]. A relevant example is YBCO (Yttrium Barium Copper Oxide), which, thanks to its performance in high magnetic fields at relatively elevated temperatures (50–77 K) and its good mechanical strength, remains one of the most extensively studied materials [4].

To date, attention is also focusing on a different class of superconducting materials — iron-based superconductors (IBS) — further expanding the prospects for their use in energy applications, thanks to their promising properties. These materials can tolerate high current densities in magnetic fields up to 30 T and operate over a wide temperature range (from 20 K to 60 K), using cryocoolers as a cooling system [5].

It should also be emphasized that the economic accessibility of these materials remains a critical challenge for their large-scale industrial application.

The aim of this doctoral thesis is to describe the characterization of two different families of superconducting materials (YBCO and IBS) in the form of thin films deposited on specific substrates, with the objective of evaluating their suitability for the fabrication of superconducting coils for magnetic confinement in nuclear fusion reactors.

The thesis is structured into three main parts. The first part is dedicated to the introduction, focusing on the selection of the materials studied and the techniques used for their deposition and characterization. The second part will concentrate on the YBCO superconductors, and the results obtained during the analysis of these samples. The third part will be devoted to the description and in-depth study of the IBS samples and the related information. Finally, the data obtained, future perspectives, and potential applications will be discussed.

This thesis will therefore provide an overview of synthesis techniques and the effects of irradiation on YBCO and IBS, starting from a critical comparison between the two material families. Moreover, guidelines will be offered to optimize the fabrication of superconducting coils, considering the Italian and European contexts and the role of Eni in promoting fusion applications at an industrial level.

The goal is to contribute to the validation of superconducting materials capable of withstanding the extreme conditions of a fusion reactor, thus accelerating progress toward commercial plants able to provide an extensive supply of clean, safe energy from inexhaustible resources.

1. INTRODUCTION

1.1 General Overview of Superconductivity

Superconductivity is a quantum phenomenon that occurs in certain materials which, below a specific critical temperature (T_c), exhibit a complete absence of electrical resistance. Under these conditions, electrons form Cooper pairs and behave as a single quantum entity capable of moving through the crystal lattice without energy dissipation, thereby generating a lossless electric current. This transition to the superconducting state is also accompanied by the Meissner effect, namely the expulsion of magnetic fields from the material — a property that clearly distinguishes superconductors from ordinary conductors and semiconductors.

The phenomenon of superconductivity was first discovered in 1911 by **H. K. Onnes**, who observed it in mercury at temperatures below 4.2 K. Initially, known superconductors were limited to conventional metals and alloys, such as lead and niobium, now classified as low-temperature superconductors (LTS). However, a breakthrough occurred in the 1980s with the discovery of high-temperature superconductors (HTS), such as YBCO (Yttrium Barium Copper Oxide). These materials can maintain their superconducting state at much higher temperatures, up to 138 K, significantly reducing reliance on costly liquid helium-based cooling systems and thereby opening new possibilities for practical applications.

Scientific and industrial interest in superconductors has grown considerably due to their potential applications in advanced technological fields, including energy production and transmission, magnetic resonance imaging, magnetic levitation for transportation, and particularly the development of magnetic coils for plasma confinement in nuclear fusion reactors.

In this context, the study and characterization of superconducting materials are essential to assess their operational suitability under extreme conditions, such as those expected in future fusion power plants. This doctoral thesis fits into this framework by addressing the analysis of two different families of superconducting materials — YBCO and IBS — with the aim of understanding their structural, electrical, and magnetic behaviour and contributing to the selection of advanced materials for strategic energy applications [6].

1.2 Theory of Superconductivity

The understanding of superconductivity made a significant leap forward in 1957 with the development of the Bardeen-Cooper-Schrieffer (BCS) theory, which is based on several key concepts:

- **Cooper pairs**: In a superconductor, electrons with opposite spin and momentum can pair up to form so-called Cooper pairs. This pairing mechanism is mediated by lattice vibrations, known as *phonons*.
- **Energy gap**: The formation of Cooper pairs creates an energy gap (Δ) where no available excited states exist. At temperatures below this gap, the usual mechanisms that would lead to energy dissipation —and thus electrical resistance— are strongly suppressed, allowing Cooper pairs to carry current without resistance.
- **BCS wavefunction**: The wavefunction that describes Cooper pairs is coherent over macroscopic distances, meaning that all pairs move in a synchronized and collective manner, giving rise to the supercurrent.
- While the BCS theory has been remarkably successful in explaining superconductivity in conventional metals such as aluminium and lead, it falls short in describing the behaviour of HTS discovered later. HTS materials may exhibit:

- **Alternative pairing mechanisms**: In HTS, electron pairing may not be mediated by phonons but by alternative excitations, such as spin fluctuations. This has led to the development of new theoretical frameworks, including spin density wave theory and the *t-J* model [7].
- **Anisotropy and structural complexity**: HTS materials have complex and anisotropic, often layered, crystal structures that strongly affect their electronic and superconducting properties. The resonating valence bond (RVB) theory proposed by Anderson is one of the models that aims to explain these phenomena. [8]

1.3 Classification and Families of Superconductors

Superconductors can be classified not only according to their structural characteristics but also based on their critical temperature ranges. We can distinguish:

A. Low-Temperature Superconductors (LTS): These materials, generally elements or alloys such as mercury, lead, and niobium, were the first to be discovered. They exhibit low critical temperatures, typically below 10 K, and their superconducting behaviour is well described by BCS theory.

B. High-Temperature Superconductors (HTS): Discovered in the 1980s, this class includes cuprates (e.g., $YBa_2Cu_3O_{7-\delta}$) and iron-based superconductors. They exhibit significantly higher critical temperatures, in some cases exceeding 100 K. The mechanisms behind superconductivity in these materials are not yet fully understood and remain an active area of research.

C. Unconventional Superconductors: This category includes materials that do not conform to BCS theory, such as organic superconductors, heavy fermion superconductors, and several iron-based compounds. These materials often exhibit exotic properties that require new theoretical models to be properly explained.

The classification of superconductors is further enriched by the identification of different material families, as illustrated in Figure 1. 1.

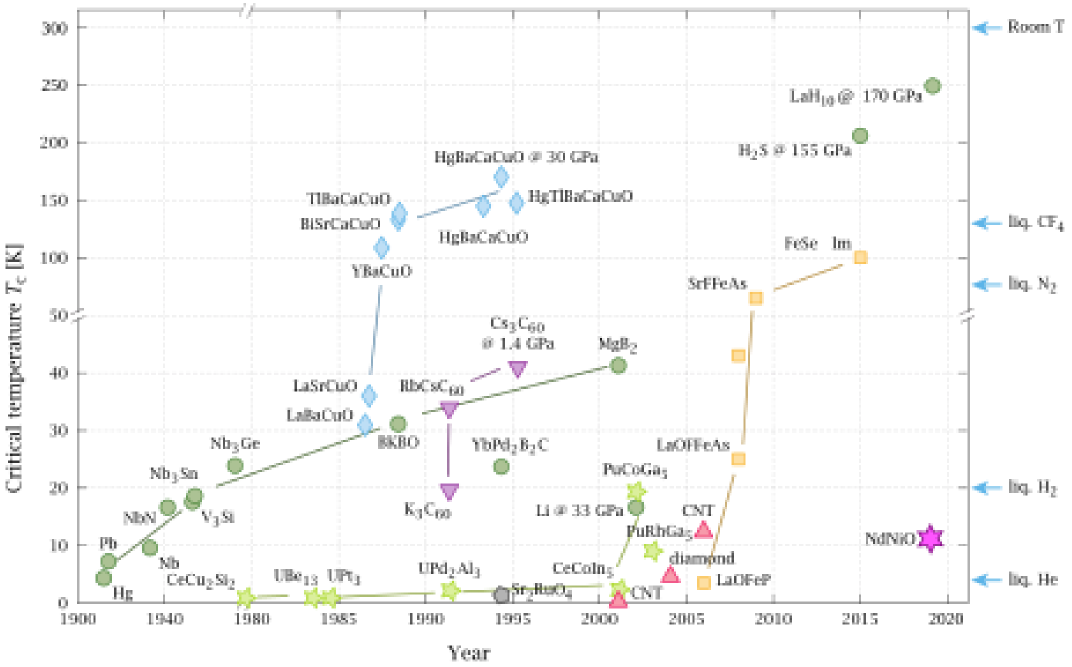

Figure 1.1 Critical temperature (T_c) of different superconductor families over time, showing the rise of HTS like cuprates and iron-based compounds

These families encompass a wide range of superconducting materials, some of which are adequately described by BCS theory, while others necessitate complementary or alternative models for a comprehensive understanding. Among the main families, we can mention:

I. Elemental Superconductors: Including the first discovered superconductor, mercury (Hg), with a T_c of 4.2 K, and niobium (Nb), which has the highest T_c among elemental superconductors at 9.3 K.

II. Alloy and Intermetallic Superconductors: Examples include Nb-Ti (niobium-titanium), widely used for superconducting magnets, and Nb_3Sn (niobium-tin), with a T_c of about 18 K, used in particle accelerator magnets.

III. Copper-Oxide (Cuprate) Superconductors: Among the most studied and widely used due to their high T_c (92 K), $YBa_2Cu_3O_{7-\delta}$ (YBCO) is a key example. Other subclasses include Ba- or Sr-doped La_2CuO_4 (LBCO, LSCO), with critical temperatures dependent on the doping level, and $Bi_2Sr_2CaCu_2O_8$ (BSCCO).

IV. Iron-Based Superconductors: These materials are based on conducting layers of iron and a pnictide (such as arsenic or phosphorus), or oxypnictides like LaOFeAs. More recent research also focuses on arsenic-free subclasses, such as the various derivatives of FeSe.

Analogously to cuprates, the superconducting properties of iron-based materials vary significantly with doping.

Another important classification distinguishes between **Type I and Type II superconductors**:

- **Type I superconductors** (Figure 1.2a) exhibit an abrupt loss of superconductivity when exposed to magnetic fields greater than the critical field H_c.

- **Type II superconductors** (Figure 1.2b), on the other hand, allow partial penetration of magnetic fields in the form of quantized vortices when the applied field exceeds the lower critical field H_{c1}. Above the upper critical field H_{c2}, superconductivity is destroyed, and the material returns to the normal state [9]

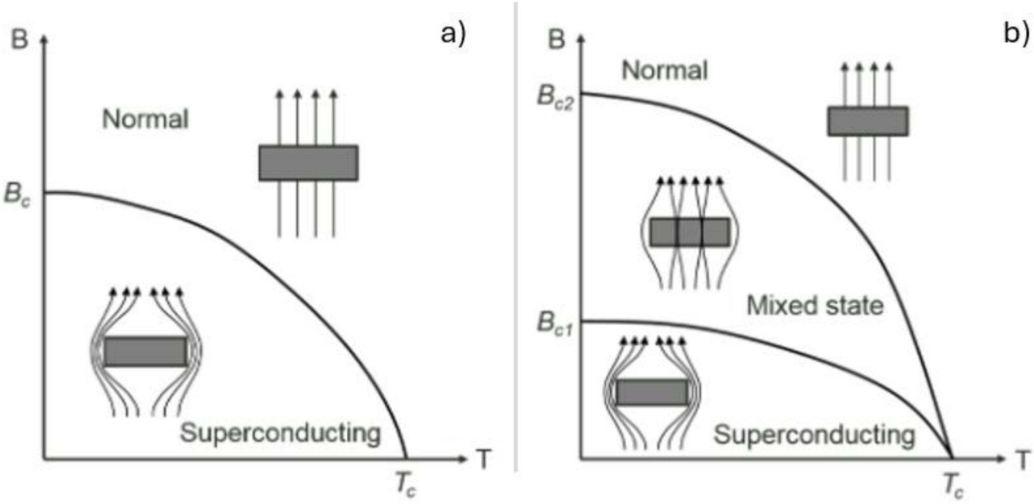

Figure 1. 2 Temperature dependence of the critical magnetic field describing the superconducting, normal, and mixed states in a) type I and b) type II superconductors.

1.4 Propriety of superconductivity- Pinning centres

Pinning centres are defects or heterogeneities in the superconductor's microstructure (point vacancies, dislocations, precipitates, grain boundaries, non-superconducting inclusions) that interact with quantized magnetic flux vortices [10]. Because each vortex carries a flux quantum Φ_0, their motion under an applied current produces dissipation and destroys superconductivity. Pinning centres "anchor" the vortices, preventing this motion and allowing the material to carry very high currents without quenching.

The J_c is the maximum current density the superconductor can sustain before vortices begin to move. To first order (Eq. 1.1)

$$\boldsymbol{J}_\mathbf{c} \approx \mathbf{F}_\mathbf{p}/\Phi_0 \text{ (eq. 1.1)}$$

where F_p is the total pinning force exerted by the defects [11]. The critical current can be further increased by deliberately introducing new pinning centres into the superconducting phase: enhancing the capacity to trap vortices—and thus increasing F_p—allows a larger current to flow.

There are two main methods to create artificial pinning centres in a superconductor:

1. **Doping** – incorporation of compounds, nanoparticles or nanowires into the superconducting matrix, which act as strong point- or line-like pinning sites [12];

2. **High-energy irradiation** – bombardment with protons or heavy ions to induce point-defect clusters or columnar tracks in the lattice.

To understand the nature of the pinning at work, one computes the pinning force

$$\mathbf{F_p}=\boldsymbol{J_c}\times\mathbf{B} \text{ (eq.1.2)}$$

from measurements of J_c. By applying the Dew–Hughes model, the shape of the normalized pinning-force curve—plotted versus reduced field—and the position of its peak can be correlated with the type and size of the pinning centres. This approach yields quantitative guidance on which defects—point, surface, or volume—are most effective in anchoring vortices and how to optimize the microstructure to maximize J_c [1].

Thanks to well-engineered pinning centres, superconductors can maintain high current densities in strong magnetic fields, anchoring vortices and pushing J_c as close as possible to its theoretical limit. Moreover, they greatly improve the cyclic stability of magnets, preserving performance over many field-ramp cycles.

1.5 The roles of substrates

The choice of substrate in the deposition of superconducting films plays a pivotal role in determining their final quality—governing crystal structure, orientation, defect density, and electronic behaviour—and thus directly impacts superconducting performance. A substrate must offer a well-defined crystalline orientation to promote epitaxial alignment and minimize disorder, and its in-plane lattice parameter must closely match that of the film to control strain, which in turn can enhance both the T_c and the vortex-pinning force. Equally important is a close match of thermal expansion coefficients between substrate and film since mismatch-induced stress during cooling can generate cracks or delamination. Chemical stability—avoiding interdiffusion or reactions at the interface—is essential to preserve a clean superconducting phase, and a low surface roughness ensures uniform nucleation and smooth film growth. In applications or measurements where parasitic conduction must be avoided, an electrically insulating substrate is preferred. Finally, for scalable, industry-level production, the substrate's cost, commercial availability, and ease of large-area fabrication must be balanced against its crystallographic and mechanical merits. By carefully optimizing all these factors—epitaxial compatibility, lattice and thermal matching, chemical inertness, surface quality, electrical insulation, and cost—one can tailor substrate selection to achieve the desired superconducting properties in the deposited film.

1.6 Effects of Irradiation on Superconducting materials

The study of irradiation effects on superconducting materials is of fundamental importance from both scientific and industrial-application perspectives. On the one hand, it is crucial to evaluate the resistance of these materials to radiation exposure, particularly in harsh environments such as nuclear fusion reactors, particle accelerators, and space-based devices. In these contexts, irradiation can introduce defects into the crystalline structure of the superconductor, significantly altering key superconducting properties such as the T_c, resistivity, and J_c. On the other hand, irradiation may also be employed in a controlled manner as a defect-engineering technique to enhance material performance where necessary. Specifically, the intentional introduction of defects can act as pinning centres for magnetic vortices, thereby increasing J_c and improving the stability of the superconductor under applied magnetic fields.

It has been observed that the substrate on which the superconducting film is deposited may itself undergo structural changes following irradiation, indirectly influencing the properties of the film through variations in mechanical strain. Such residual stress can lead to degradation of the superconducting parameters and should therefore be carefully assessed. In the case of thin films, this effect is particularly significant: while T_c is only slightly affected by irradiation, the residual resistivity ρ_0 increases significantly. [13]

In this framework, irradiation is regarded not only as an external stressor to be evaluated, but also as a potential tool for the fine tuning of the functional properties of superconducting materials. [14,15]

However, an excessive density of irradiation-induced defects may lead to a deterioration of superconducting coherence and connectivity, requiring a fine balance to optimize performance. In addition, the energy of the irradiating ions plays a crucial role in determining the extent and nature of the induced damage. An increase in ion energy generally accelerates the degradation of the T_c with increasing displacements per atom (dpa). This behaviour can be attributed either to different efficiencies in defect production at various energies, or to the fact that dpa alone does not fully capture the structural consequences of ion irradiation. For high-energy heavy ions, an additional mechanism becomes relevant: the deposition of energy via ionization. Once the electronic stopping power exceeds a certain threshold, it can induce local lattice distortions or even transient melting along the ion track. This process, well documented in the literature, is responsible for the formation of linear defects and continuous columnar tracks in a wide range of materials, including iron-based superconductors.

In the present study, two different irradiation strategies were applied to the superconducting thin films under investigation: for the YBCO film we used

1.2 GeV Pb ions, corresponding to a matching field of 3 T, whereas Au ions at 230 MeV were employed for the FeSeTe film.

1.7 HTS in the Context of Magnetic Confinement

The interest in superconductors for fusion devices arises from the need to confine plasma using intense magnetic fields, which are essential to sustain high plasma temperatures without physical contact with the reactor walls.

From a technological development standpoint, the first tokamak to employ superconducting toroidal and poloidal magnets was the Experimental Advanced Superconducting Tokamak (EAST), also known as HT-7U (Hefei Tokamak 7 Upgrade), an experimental magnetic fusion reactor located in Hefei, China.

Operated by the Hefei Institutes of Physical Science for the Chinese Academy of Sciences, EAST began operations in 2006 and is an integral part of the ITER (International Thermonuclear Experimental Reactor) initiative.

However, the superconducting material used in EAST is a niobium-titanium alloy, classified as a LTS, which limits the maximum applicable magnetic field to approximately 7 T.

By contrast, HTS materials offer substantial advantages over LTS, enabling higher magnetic fields, typically around 12 T [16].

Moreover, due to their ability to carry current without resistance, HTS materials can generate such magnetic fields with lower energy losses compared to conventional magnets.

For this reason, particular attention has been directed toward the **SPARC** project (Smallest/Soonest Possible ARC) [17], a magnetic confinement fusion tokamak developed by the U.S.-based company Commonwealth Fusion Systems (CFS) in collaboration with the Plasma Science and Fusion Centre at the Massachusetts Institute of Technology (MIT).

The project is funded by several research institutions, among which **Eni** plays a prominent role [18,19].

Currently, SPARC employs HTS superconducting magnets based on YBCO, which maintain superconductivity up to 77 K. [20]

In September 2021, a prototype high-field magnet coil was successfully evaluated, setting a record for HTS magnets, with a field strength of 20 T at a temperature of 20 kelvin. [21]

These achievements, however, highlight the next set of technological challenges required for full-scale deployment.

However, to fully exploit the potential of HTS materials in fusion devices, the magnets must be scaled to high magnetic fields (over 20 T on-coil) and large apertures (greater than 1 m); this entails numerous structural and integration challenges, including the management of Lorentz forces, tape quality assurance, cryogenics, and fabrication processes.

The continuous and large-scale production of HTS represents a new challenge, requiring new materials, manufacturing techniques, integration methods, and testing procedures.

Furthermore, the use of HTS materials also presents challenges related to the operating environment of fusion reactors, particularly exposure to neutron radiation; it is therefore important to consider the effect of high-energy neutron irradiation on the superconducting properties of coated conductors.

The fusion reaction between deuterium and tritium in a tokamak plasma emits neutrons with energies between 12 and 20 MeV.

Thus, a fusion-relevant neutron spectrum must contain a significant fraction of high-energy neutrons, which may degrade superconductor performance.

Since no current neutron sources provide both the flux and energy appropriate to fusion conditions, previous experimental studies have focused on analysing the effects of irradiation on the superconducting properties of coated conductors (CC) using:

- fission-spectrum neutrons,
- heavy ions,
- light ions/protons.

These experiments have shown that—except in low magnetic fields—an initial increase in J_c is observed as the irradiation dose increases, followed by a decrease in both J_c and T_c, eventually leading to a complete loss of superconductivity.

Among the various challenges for the realization of full-scale fusion plants, economic factors also play a significant role, as in the case of YBCO, which—despite its promising electrical and magnetic properties—remains expensive and difficult to produce on a large scale. For these reasons, other superconducting materials are also being considered, such as iron-based superconductors (IBS) in the form of Fe(Se,Te), as discussed in this study.

These materials are mechanically more robust and more resistant to thermal and mechanical stress compared to YBCO, and they are often easier to synthesize in the laboratory than cuprates, although large-scale production of technologically reliable tapes remains a challenge.

1.8 State of the Art: YBCO Superconducting Films

$YBa_2Cu_3O_{7-x}$ (YBCO) represents one of the most extensively studied high-temperature superconducting materials since its discovery. The growth of YBCO thin films on $SrTiO_3$ (STO) substrates has been widely investigated since the early 1990s, with numerous studies focusing on the optimization of deposition parameters and substrate preparation methods. [22,23]

Critical parameters for high-quality YBCO film growth include substrate surface termination, deposition temperature, oxygen partial pressure, and post-deposition annealing conditions. The STO substrate surface chemistry, particularly the balance between SrO and TiO_2 terminations, plays a crucial role in determining nucleation sites and subsequent epitaxial quality. Studies have shown that controlled chemical etching can achieve single-termination surfaces, leading to improved crystalline quality and superconducting properties. [24]

The structural defects commonly observed in YBCO films include antiphase boundaries, stacking faults, misoriented grains, and twin boundaries. These defects significantly influence the critical current density (J_c) and can act as flux pinning centers, thereby affecting the film's performance in high magnetic fields.

1.9 State of the Art: Iron-Based Superconducting Films (FeSeTe)

Iron-based superconductors, discovered in 2008, represent the second family of high-temperature superconductors after cuprates. Among them, $FeSe_{1-x}Te_x$ has attracted significant attention due to its relatively simple crystal structure and tunable superconducting properties through Te substitution. [25, 26]

The optimal Te doping level for maximizing T_c typically ranges between $x = 0.5$ and 0.7, where critical temperatures up to 15-18 K have been reported. The superconducting properties are highly sensitive to the Se/Te ratio, crystalline quality, and interfacial strain when grown as thin films.

Recent studies have demonstrated that the use of non-superconducting FeSeTe seed layers can significantly improve the structural quality of subsequently deposited superconducting layers. This approach helps to accommodate lattice mismatch with the substrate and provides a template for improved epitaxial growth. The choice of substrate (CaF_2, MgO, or CeO_2/YSZ buffered substrates) and deposition technique (primarily Pulsed Laser Deposition, PLD) critically influences the final film properties. [27]

2. EXPERIMENTAL METHODS FOR SYNTHESIS AND CHARACTERIZATION

2.1 Deposition Techniques

The deposition of superconducting thin films is organized into three main families of techniques. Physical Vapor Deposition (PVD) methods—such as Pulsed Laser Deposition (PLD), magnetron sputtering (DC for conductive films, RF for insulating oxides), thermal or electron-beam evaporation, and Molecular Beam Epitaxy (MBE)—exploit the ablation or evaporation of a source material and vapor-phase transport to recondense atoms or molecules onto the substrate with high control over crystalline quality [28]. Chemical Vapor Deposition (CVD) techniques include Metal-Organic CVD (MOCVD), conventional CVD, and Atomic Layer Deposition (ALD): in these processes gaseous precursors decompose or react near the heated substrate to form atomic or multilayer films with excellent uniformity and conformality on complex geometries [29,30].

Among solution-based deposition methods, the sol-gel route and Metal-Organic Deposition (MOD) stand out; these involve applying a liquid precursor (via spin-coating, dip-coating, or spray) followed by pyrolysis and annealing steps to convert the organic film into a ceramic oxide, as well as inkjet printing and spray pyrolysis variants, which are particularly suited to flexible substrates and highly scalable processes [31]. Finally, electrodeposition represents an electrochemical approach in which metal ions in solution are reduced directly onto a conductive substrate, allowing precise control of film composition and thickness via electrical parameters. Each of these techniques offers a different balance between epitaxial quality, uniformity, growth rate, and equipment cost, and is selected according to the desired superconducting properties and specific applications.

The superconducting materials described in subsequent chapters were obtained via PVD techniques; specifically, DC sputtering was used for YBCO and PLD for Fe(Se,Te) [31, 28].

2.1.1 Sputtering DC

The Direct Current Sputtering (or *DC sputtering*) is a Physical Vapor Deposition (PVD) technique in which one or more targets made of the material of interest are subjected to a continuous current inside a vacuum chamber. The process relies on the energy of accelerated ions to dislodge atoms from the target, which are then deposited onto a substrate. The process consists of three main stages:

a. Presputtering: This is a preparatory step aimed at removing surface contaminants from the target before the actual deposition. A plasma is generated using an inert gas (typically argon); the plasma ions bombard the target, eliminating impurities such as oxides or particles and stabilizing the plasma.

b. Deposition: Under specific temperature and pressure conditions—depending on the nature of the material being sputtered—a continuous current is applied between the anode (target) and the cathode (substrate) in the presence of a flow of inert gas. At the start of this stage, the plasma is ignited by applying specific voltage and current values such that the power does not exceed 40 W. This ensures a stable plasma suitable for YBCO deposition while avoiding damage to the target or substrate. The deposition time can directly influence the thickness of the resulting film.

c. Cooling and Oxygenation: In the case of superconducting materials, this is the most critical step. The deposited film is brought back to room temperature very slowly to avoid thermal shock and, where necessary, to stabilize the material's phase.

This technique was used to deposit YBCO films on STO substrates, employing a non-superconducting YBCO target and a gas mixture of argon and oxygen.

The choice of this mixture proved essential, as the oxygen in the plasma helps ensure that the thin film becomes properly oxidized during deposition. Without the presence of oxygen, the film could be oxygen-deficient or have an incorrect stoichiometry, thus compromising its superconducting properties.

However, to obtain a superconducting film, the oxygenation phase proved to be the most critical step. By applying a controlled cooling rate under a continuous flow of an $Ar:O_2$ gas mixture, it was possible to induce the transformation of YBCO from its tetragonal, non-superconducting phase into its orthorhombic, superconducting phase.

The operating parameters of the entire process are reported in Table 2.1. These parameters were selected based on previous optimization studies that demonstrated optimal crystalline quality and superconducting properties at these conditions.

The deposition of YBCO films was carried out at 900 °C and 2.8 mbar, conditions that provide sufficient surface mobility of the deposited species, thereby promoting epitaxial growth and the formation of the orthorhombic superconducting phase in the thin films. The choice of sputtering parameters, such as substrate temperature, working pressure, and Ar/O_2 gas ratio, is a critical factor for achieving good structural and electrical properties in HTS films, as demonstrated in studies optimizing these parameters for YBCO films on crystalline substrates.

In particular, the oxygen partial pressure during deposition and the subsequent controlled cooling under an oxidizing environment help stabilize the stoichiometry and promote the transition to the superconducting phase [32].

Moreover, the pre-deposition preparation of the $SrTiO_3$ substrate is essential for epitaxial nucleation and the film's microstructure, as the surface termination directly affects defect density and grain alignment, and various pre-etching treatments can significantly improve the crystalline quality of YBCO films deposited by sputtering [33].

Operating T (C°)	**Gas Pressure (mbar)**	**Power (W)**	**Cooling rate (°C/min)**
900	2.8	40	4 °C/min

Table 2.1 Summary of the operating parameters of Sputtering DC for YBCO.

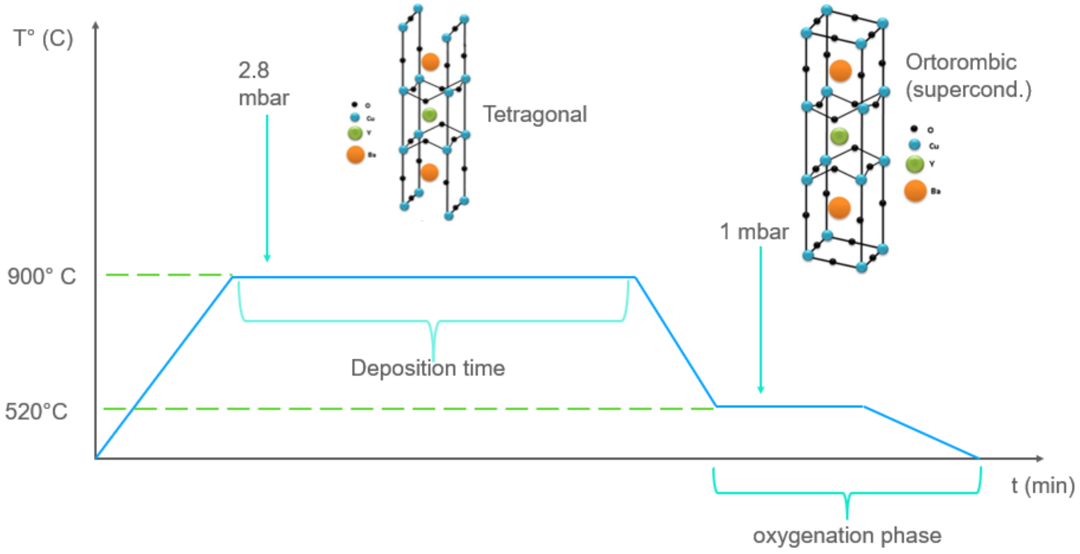

Figure 2.1 Temperature profile during YBCO film deposition and post-deposition oxygenation. The deposition is carried out at 900 °C and 2.8 mbar, leading to a tetragonal (non-superconducting) phase. After deposition, the sample undergoes a controlled cooling and oxygenation step at 520 °C and 1 mbar, which induces the transition to the orthorhombic superconducting phase.

Several YBCO superconducting films were successfully obtained and analysed, with the technical details reported in Table 2.2. As shown in the Table, the samples labelled MLY#1 and MLY#2 differ respectively by the absence of a pre-deposition etching process in the first case and by a prolonged etching (over 10 s) in the second. The aim of adopting these procedures was to evaluate the influence of substrate etching on the resulting film and to determine whether a short etching could be more effective than a longer one.

Sample	Standard Cleaning	SC+ etching 12 h	SC+ etching 10 s	T_c	TEM	Litography
MLY#1	x			82.8	x	
MLY#2		x		89.7	x	
MLY#5			x	89.9	x	x
MLY#6			x	78.0	x	
MLY#8			x	89.6		x
MLY#9			x	90.2	x	

Table 2.2 Summary of the cleaning/etching procedures, critical temperature T_c, and characterization steps (TEM, lithography) for the MLY samples.

It was observed that the samples subjected to either long etching (MLY#2) or short etching (except for sample MLY#6) exhibit very similar R(T) behaviours, although with different T_c values. Based on these results, the discussion presented here will focus on three representative samples, renamed as follows:

- **Smp_$_{NE}$ (No Etching):** substrate without any etching treatment.
- **Smp_$_{LE}$ (Long Etching):** substrate subjected to prolonged etching (>10 s).
- **Smp_$_{SE}$ (Short Etching):** substrate subjected to a very short etching process (10 s).

The selection of these samples is primarily due to the quality of the deposited film, which exhibits sufficiently good superconducting properties according to the Van der Pauw measurements described in 3.9.

The deposition of the YBCO film was carried out at the ***CNR-SPIN laboratory in University of Salerno.***

2.1.2 Pulsed Laser Deposition

Pulsed Laser Deposition is a Physical Vapor Deposition (PVD) method in which a high-power pulsed laser beam is focused inside a vacuum chamber to strike a target composed of the material to be deposited. This material is vaporized from the target (forming a plasma plume), which then deposits as a thin film onto a substrate. The process can take place either in ultra-high vacuum or in the presence of a background gas [34].

The PLD process can generally be divided into four main stages:

1. Laser absorption on the target surface and laser ablation of the target material, resulting in plasma generation

2. Plasma dynamics

3. Deposition of the ablated material onto the substrate

4. Nucleation and growth of the film on the substrate surface

Each of these steps is critical for determining the crystallinity, uniformity, and stoichiometry of the resulting film.

This technique was employed for the deposition of FeSeTe films on YSZ substrates. In this context, the deposition was carried out in an ultra-high vacuum chamber (residual pressure during deposition ~10^{-8} mbar) equipped with a Nd:YAG laser operating at 1024 nm, using a polycrystalline target with nominal composition $FeSe_{0.5}Te_{0.5}$, synthesized through a two-step method [35].

The synthesis and deposition of the FeSeTe film was carried out at the CNR-SPIN laboratory in Genoa [36] by three steps:

1) CZO (buffer) is deposited on the YSZ single crystal substrate by spin coating at 2000 rpm for 60 seconds and dried for 5 minutes at 120°C in air. The pyrolysis heat treatment is carried out in static air (30 min at 450°C) and the crystallization treatment in flowing 5% Ar-H_2 (30 min at 950°C).

2) The Fe(Se,Te) non-superconducting seed layer (≈100 nm thick) is deposited at 400°C at a high laser repetition rate (10 Hz). The insertion of this seed layer serves to promote epitaxial alignment and improve the crystalline quality of the subsequent superconducting top layer. By providing a template with lattice parameters closer to the film, the seed layer reduces the formation of misoriented grains and structural defects, thus enhancing the uniformity and superconducting properties of the FeSeTe layer .

3) The Fe(Se,Te) films are deposited by PLD with the parameters reported in Table 2.3. The choice of deposition temperature, laser fluence, repetition rate, and background pressure was guided by previous

literature and preliminary optimization experiments, aimed at achieving the optimal Se/Te stoichiometry, epitaxial growth, and overall crystalline quality [27].

The choice of these parameters was guided by previous literature results and preliminary optimization experiments aimed at achieving the optimal Se/Te ratio and crystalline quality.

Operating T (C°)	**Pressure (mbar)**	**Laser Power (Nd:YAG)**	**Laser Fluence**	**Target**	**Target–substrate distance**
200	10^{-8}	1024 nm	2 J/cm^2	$FeSe_{0.5}Te_{0.5}$	5 cm

Table 2.3 Summary of the operating parameters of PLD for Fe(Se,Te)

2.2 Evaluation of Superconducting Properties

To initially identify the superconducting properties of certain materials, they can be used two electrical characterization techniques: ***Van der Pauw*** methods and the four-wire technique (also known as ***Kelvin connection***).

The Van der Pauw method can be used to measure the resistivity and electrical conductivity of thin, homogeneous materials.

This method involves using four contacts placed at the corners of the sample if it has a square or rectangular shape, how showed in Fig 2.2.

The resistivity (ρ) is determined by measuring two characteristic resistances, R_A and R_B, obtained by switching the current and voltage electrodes positioned at the corners, and applying the associated relation show in eq.2.1:

$$e^{(-\frac{\pi R_A}{R_s})}+e^{(-\frac{\pi R_B}{R_s})}=1 \quad \text{(eq.2.1)}$$

where R_s is the sheet resistance of the material. Knowing the sample thickness (d), the bulk resistivity can be obtained by equation 2.2:

$$\rho = R_s \cdot d \quad \text{(eq.2.2)}$$

This method is widely used for the characterization of superconducting materials, but it also applies to semiconductors and thin metallic films, providing accurate measurements even independently of the sample geometry, provided the applicability conditions are met.

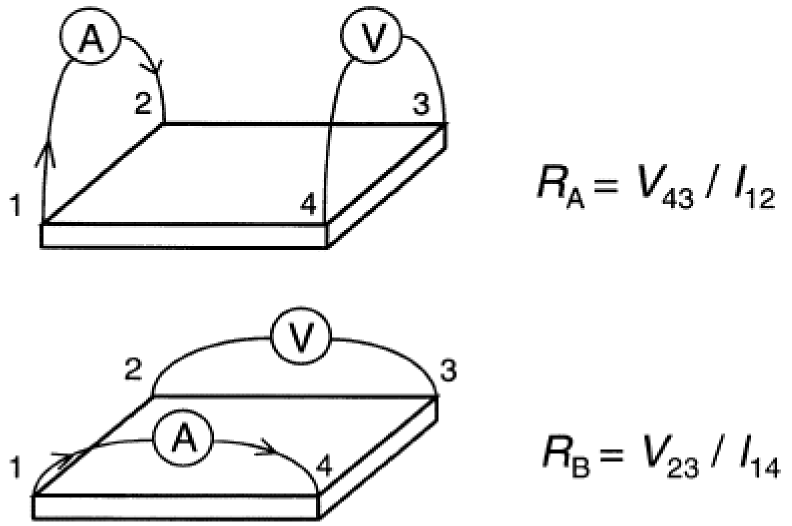

Figure 2.2 Schematic representation of two measurement configurations used in the Van der Pauw method to determine the sheet resistance of a thin film sample.

To evaluate the superconducting properties of this type of films—specifically, the Fe(Se,Te) film deposited on CZO— the four-wire technique was employed. In the context of experimental characterization, this measurement enables the acquisition of current–voltage (I–V) curves that are essential for accurately determining the material's J_c in the presence of high magnetic fields, while eliminating errors caused by contact resistances and cables.

From a practical standpoint, the technique uses two wires (referred to as "force") to supply current to the sample, and two wires (referred to as "sense") to measure the voltage drop solely across the sample, independent of any resistance in the cables or connectors, as schematically shown in Fig. 2.3.

By applying a constant current (I) through the force wires, the voltage (V) across the sample is measured using the sense wires. The resistance is then determined using Eq. 2.3:

$$R = V / I \quad \text{(eq.2.3)}$$

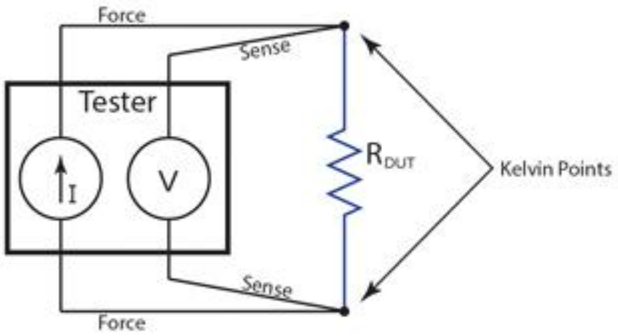

Figure 2.3 Schematic of 4-point resistance measurement setup.

Since the sense wires carry no current, any voltage drop due to their resistance is negligible. Measuring the voltage exclusively across the sample to yield the intrinsic resistance, free from errors introduced by cable or contact resistances.

2.3 XRD

X-ray diffraction (XRD) is one of the fundamental techniques for the structural characterization of superconducting thin films. In fact, it allows verification of the formation of the desired crystalline phase, as well as the identification of any secondary phases or impurities that may arise during the deposition process.

In the case of thin and epitaxial films, XRD enables precise analysis of the crystallographic orientation, with particular attention to preferential growth along a specific axis.

Moreover, the possible observation of interference fringes around the main diffraction peaks can provide additional information on the uniformity of the film thickness and the quality of the film–substrate interface. However, for films thinner than approximately 50 nm, the XRD signal can be very weak, making the use of more sensitive measurement techniques or complementary methods necessary [37].

Structural characterization through **θ–2θ scans** represents an essential tool for evaluating the film. During this analysis, the sample is positioned so that the X-ray beam impinges perpendicularly on the film surface, while both the source and the detector rotate simultaneously, maintaining the θ–2θ angular relationship.

The identification of diffraction peaks corresponding to the (00ℓ) planes confirms c-axis-oriented growth and allows the exclusion of undesired secondary phases.

The precise position of the intensity maxima is used to determine the lattice parameters of the film and to assess any strain induced by lattice mismatch with the substrate.

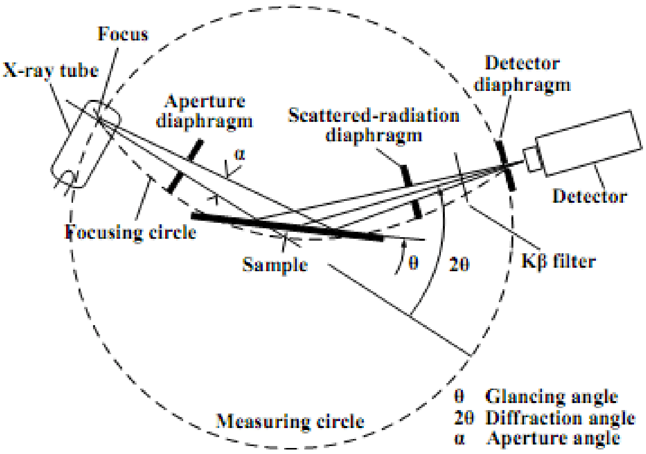

Figure 2.4. Schematic diagram of XRD (Connolly, 2007)

Moreover, the **full width at half maximum (FWHM)** of the peaks provides valuable information on defect density and the degree of crystalline order in the material. A generic schematic of the system is shown in Figure 2.4.

2.4. FIB

The FIB technique employs an ion column that generates and focuses Ga^+ ions onto a small area of the sample, as schematized in Fig. 2.5.

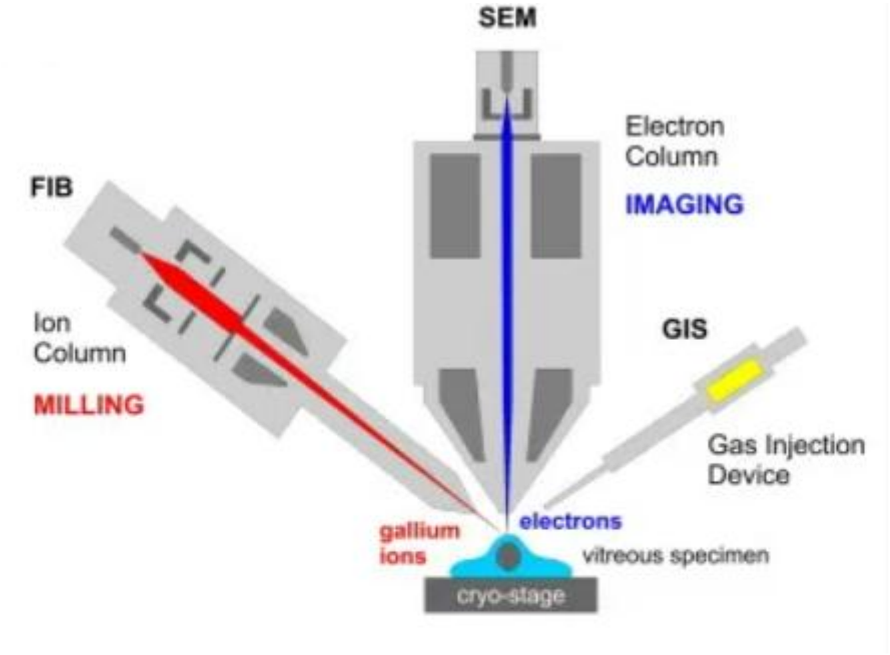

Figure 2.5 Schematics of a dual-beam FIB/SEM system showing the ion column used for milling, the electron column used for imaging, and the gas injection system (GIS)

These ions, with energies ranging from 1 to 30 keV, strike the surface and transfer energy to the atoms of the target material, causing their ejection (sputtering). This process allows for precise milling of the sample and the preparation of cross-sections or lamellae. Before thinning begins, a protective layer of platinum (Pt), carbon (C), or Pt/C is deposited on the sample to shield the area of interest from sputtering damage.

Once the lamella is mounted on the TEM grid, it is further thinned using a low-energy ion beam (typically <5 keV) to reduce irradiation damage and Ga ion implantation. This step enhances sample quality by minimizing structural defects and achieving a final thickness suitable for TEM observation. This process is referred to as the In-Situ Lift-Out technique [38].

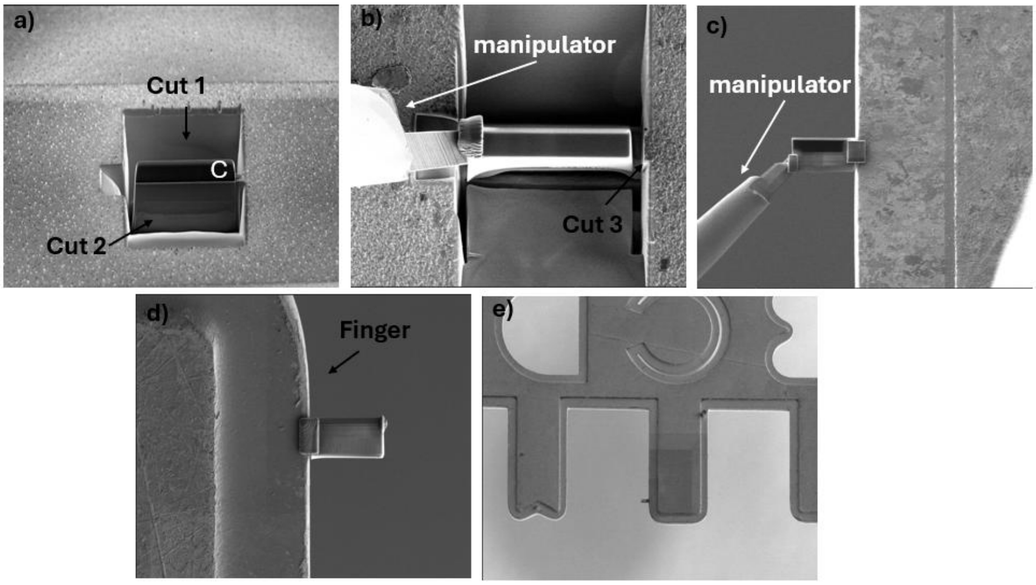

Figure 2.6 Steps involved in TEM specimen preparation using FIB-SEM: (a) Lateral and frontal cuts to isolate the region of interest of the sample.
(b) Lift-out of the lamella using the micromanipulator after separation cuts.
(c) Transfer of the lamella onto the support grid with the micromanipulator.
(d) Attachment of the lamella to the finger of the support.
(e) Final view of the lamella mounted on the grid, ready for subsequent thinning and TEM analysis.

Figure 2.6 (a–e) shows the typical in-situ lift-out sequence performed in this work and illustrates the steps relevant to that stage. After deposition of a protective carbon layer over the area of interest, trenches are milled on two sides of the C deposit to shape the specimen (Fig. 2.6a–c). The largest trench (cut 1), located away from the specimen, is made at high current (e.g., 9 or 20 nA) to remove bulk material rapidly; the current is then progressively reduced as milling approaches the specimen to minimize the risk of Ga implantation. The micromanipulator is then attached to the specimen using C (Fig. 2.6c) and the final edge is milled (cut 4) to completely detach the lamella from the parent material. After transfer, the lamella is mounted on a TEM grid and subjected to low-energy polishing: the final polishing steps are often performed at energies down to a few 2 keV, to remove the damaged surface layer and optimize sample quality.

In our case, the samples were prepared using a **Thermo Fisher Helios 5UC FIB** at **CNR-IMM Catania**, and a **Helios Nanolab 600i FIB** at **CNRS-CEMES Toulouse**.

The FIB system incorporates a Scanning Electron Microscope (SEM) in both instruments described, which allows real-time observation of the sample surface and monitoring of the lamella preparation and thinning process. This combined approach ensures precise control over milling and helps achieve the desired sample geometry for TEM analysis.

2.5 Irradiation of Superconducting Materials

As previously mentioned, in fusion reactors the materials used for the fabrication of superconducting magnets are exposed to intense radiation fluxes, particularly of neutronic origin, which can compromise the structural and electronic properties of the compounds involved. In this context, studying the effects of irradiation on high-temperature superconductors (HTS) is crucial for assessing their reliability under extreme operating conditions. Ion irradiation represents a key experimental tool to investigate the radiation tolerance of superconducting materials designed for fusion applications, as it allows controlled introduction of damage under well-defined conditions.

Irradiation can generate crystalline defects through both nuclear (ballistic collisions) and electronic (ionization) energy loss mechanisms, which, if properly controlled, may function as effective pinning centres for magnetic flux vortices, thereby enhancing the critical current density J_c. However, such microstructural modifications can also lead to a degradation of superconducting properties, such as a reduction in the critical temperature T_c.

In this study, irradiation experiments were carried out using 230 MeV Au ions at the Tandem accelerator of the **INFN–Legnaro National Laboratories (Italy),** with a fluence of $\Phi = 4.84 \times 10^{11}$ ions/cm^2. The choice of ion species, energy, and fluence was guided by the need to reproduce, as closely as possible, the neutron-induced damage conditions expected in fusion reactor environments.

SRIM (Stopping and Range of Ions in Matter) simulations were employed to estimate the nuclear and electronic stopping powers as well as the depth distribution of implanted ions, thereby supporting the experimental design. It should be noted, however, that SRIM calculations provide only indirect information on damage, as they do not directly predict the nature or density of the defects formed. Therefore, the actual defect structures and their impact on superconducting properties must be assessed through complementary techniques, such as transmission electron microscopy (TEM) and electrical transport measurements. [39]

The analysis of the post-irradiation behaviour of YBCO and Fe(Se,Te) thus enables an investigation of the delicate balance between irradiation-induced damage and performance enhancement, depending on the radiation parameters and the morphology of the induced defects.

2.6 Lithography

To realize a geometry of YBCO film we used a standard photolithographic process where a UV source and a collimating optical system are used to project the image of a mask with a specific pattern onto a substrate coated with a layer of photosensitive polymer (photoresist).

The illuminated pattern is then transferred onto the substrate through a subsequent etching process.

The entire process consists of several sequential steps, each carried out under specific conditions and for a predetermined duration, depending on the desired pattern objective. This technique is suitable for studying flat substrates but is not suitable for patterning on highly curved surfaces or for fabricating complex 3D structures.

Specifically, the process involves the following steps:

- **Substrate preparation:** cleaning to remove organic, metallic, and particulate contaminants to ensure adhesion and uniformity of the photoresist.
- **Photoresist deposition:** applying a thin and uniform layer of photosensitive resin by spin coating, which will then be exposed to UV light.

- **Soft bake (prebake):** the sample is heated (e.g., 90–100 °C) for several minutes to evaporate residual solvents and activate the photoresist sensitivity.
- **UV exposure:** the photoresist is irradiated through a mask with the geometric pattern to be transferred. The light modifies the solubility of the resist in the exposed areas.
- **Photoresist development:** the development removes the resist regions solubilized by the exposure (positive or negative depending on the type), revealing the pattern on the surface.
- **Wet etching:** the sample is immersed in a chemical solution that selectively etches the exposed material, physically transferring the pattern onto the underlying film.
- **Resist removal (stripping):** the residual resist is eliminated using specific solvents, leaving only the material etched according to the desired design visible.

The masked sample is thus ready for analysis by other techniques [40;41].

To observe the behaviours of the superconducting YBCO film on STO after irradiation, a mask was applied using the wet-etch photolithography technique, with a quartz and silicon oxide mask and a Hall geometry, as shown in Fig. 2.7. The selected mask is highlighted with a red box.

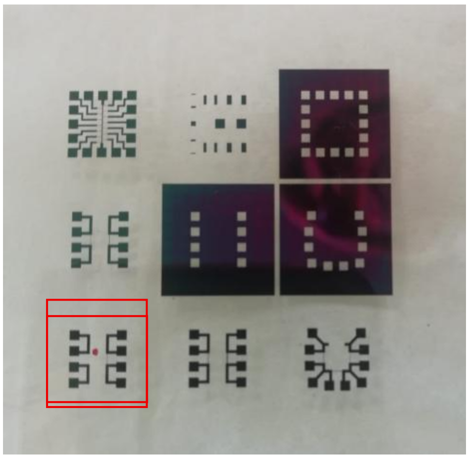

Figure 2.7 Quartz slide containing the various masks used during the lithography steps for the pattern definition on the substrate. The mask used is highlighted in red

The lithographic process was carried out at the Photolithography laboratories of ***CNR-SPIN and University of Salerno*** in a Clean Room class 1000, using a Maskaligner Karl SUSS MJB3 and a positive photoresist AZ 1518. The photoresist was deposited by spin coating at 4000 rpm for 30 seconds. After that, the samples underwent a pre-bake at 80 °C for 20 minutes and then exposed to the UV radiation of the Maskaligner.

A developing with AZ-Developer for 30 seconds allowed the geometry to show up and a post-bake at 120 °C for 20 minutes was performed to improve the resist's performance and stability. This bake step enhances the resist's resistance to etchants and improves its adhesion for subsequent processes like etching. The wet etching was performed with a solution of 60 ml deionized H_2O + 5 ml H_3PO_4, for approximately 25 seconds.

2.7 Characterization by electron microscopy

The use of electron microscopy techniques—particularly Scanning Electron Microscopy (SEM), Transmission Electron Microscopy (TEM), and Scanning Transmission Electron Microscopy (STEM)—is of fundamental importance in the study of superconducting films deposited on substrates. These films, often with nanometric thicknesses (even <100 nm), exhibit extremely complex structural, morphological, and chemical characteristics that directly influence their superconducting properties, such as T_c, critical current density, and the presence of pinning centres.

Scanning Electron Microscopy (SEM) is especially useful for evaluating the surface morphology of superconducting films. This technique provides high-resolution images of the sample’s topography, offering information on homogeneity, roughness, the presence of secondary particles, or macroscopic defects. SEM typically operates at accelerating voltages ranging from a few tens of volts up to 30 kV and can also be used on thin samples in transmission mode. The spatial resolution depends on the electron beam diameter, which is determined by the source and lens configuration, but is also limited by the beam/specimen interaction volume. Depending on the detector configuration, the SEM can collect secondary, backscattered, or transmitted electron signals, as well as additional information from techniques such as Electron Backscatter Diffraction

(EBSD), Cathodoluminescence (CL), or Electron Beam Induced Current (EBIC).

Transmission Electron Microscopy (TEM) allows for ultra-high-resolution analysis, down to the atomic scale. TEM instruments with field emission sources typically achieve a resolution of ~1.2 Å, and modern aberration-corrected systems can reach up to 0.5 Å. However, samples must be extremely thin (less than 100 nm) to be transparent to the high-energy electrons, which can have accelerating voltages up to 1 MeV. TEM enables detailed analysis of the internal microstructure of the film, highlighting crystalline defects, dislocations, inclusions, and grain boundary morphology. Crystallographic information is obtained via selected area or convergent beam diffraction modes.

Scanning Transmission Electron Microscopy (STEM) combines the functionality of TEM with high-precision beam scanning. An exceptionally fine electron probe (as small as 1 Å) is rastered across the thin sample. STEM typically operates at accelerating voltages between 80 and 300 kV and can detect elastically scattered electrons at high angles (High-Angle Annular Dark Field or HAADF), providing Z-contrast—that is, information on atomic number distribution. The integration of Energy Dispersive X-ray Spectroscopy (EDS) and Electron Energy Loss Spectroscopy (EELS) spectrometers further enhances the capabilities of the microscope, allowing for site-specific chemical and structural analysis at the level of individual atomic columns, making STEM an extremely powerful tool for advanced studies of superconducting materials.

The differences between the three techniques, in terms of the electron gun and internal components, are illustrated in Fig.2.8.

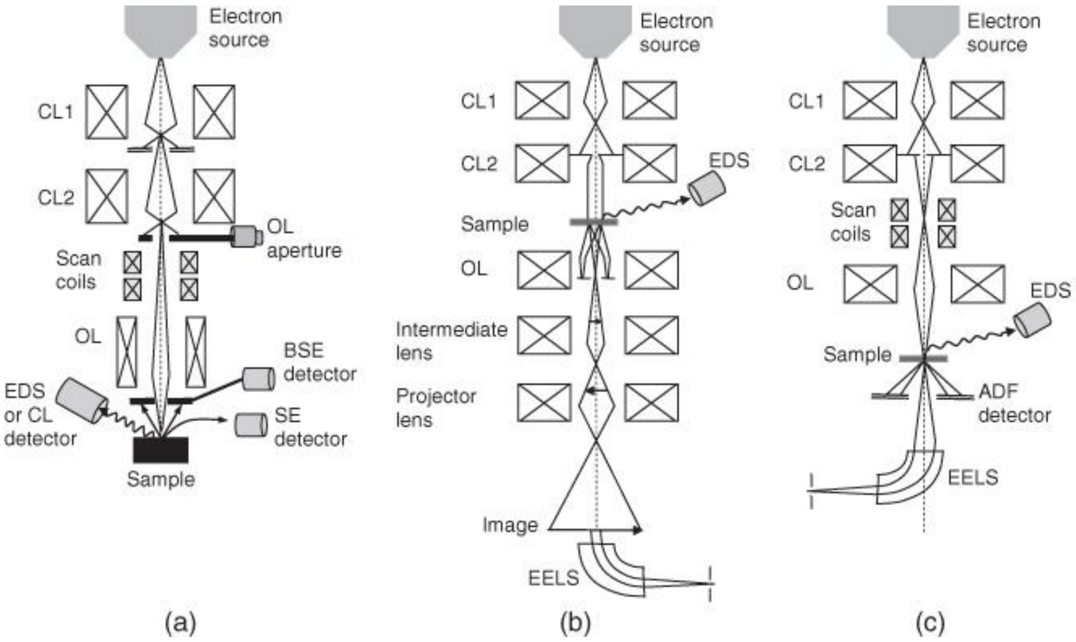

Figure 2.8 Simplified schematic cross-sections of an (a) SEM, (b) TEM and (c) STEM instrument.

2.7.1 Scanning Electron Microscopy

The scanning electron microscope ***(SEM),*** Figure 2.9, is a powerful tool for surface observation of specimens, providing high-resolution, grayscale images with a three-dimensional appearance. Electrons generated by a source and focused onto the surface under observation—via a series of electromagnetic lenses and an objective lens—interact with the specimen, producing a variety of localized signals. These signals are collected and processed, and their intensities are used to generate an enlarged image displayed on a monitor.

The SEM operates under high column vacuum conditions (typically 10^{-5}–10^{-7} mbar), which are essential to prevent electron beam scattering and to maintain focus stability.

The main signals used in SEM are:

- **Backscattered electrons (BSE)**: Produced by elastic interactions between incident electrons and the nuclei of atoms in the specimen. Detected by the Backscatter Detector (BSD), BSEs yield compositional images in which grayscale contrast is a function of atomic number (heavier elements appear lighter, lighter elements appear darker).
- **Secondary electrons (SE)**: Emitted from the specimen following inelastic interactions with the incident beam. Because they have low energy, only those generated within a few tens of nanometres of the surface

can escape and reach the Secondary Electron Detector (SED). SE images emphasize topographic and morphological surface details, giving a more three-dimensional effect.

- **X rays – Energy-Dispersive Spectroscopy (EDS):** Characteristic X rays emitted by the specimen allow both qualitative and semi-quantitative elemental identification. Integration of an EDS detector also enables two-dimensional elemental mapping of the surface.

The final magnification of the image depends on the ratio between the display screen size and the actual area of the specimen being scanned: the smaller the scanned area, the higher the magnification. Additionally, longer dwell times at each scanned point improve image sharpness.

SEM is widely used in combination with a Focused Ion Beam (FIB) system, which permits targeted material removal via an ion beam to prepare cross sections or specific surfaces of the specimen. This integration allows highly precise analysis of internal structures and defects.

Compared to transmission electron microscopy (TEM), SEM primarily observes specimen surfaces without requiring ultrathin sections. TEM, by contrast, demands specimens thinner than about 100 nm to allow electron transmission and provides atomic-scale imaging of internal and crystallographic structures, but with more complex and less versatile sample preparation.

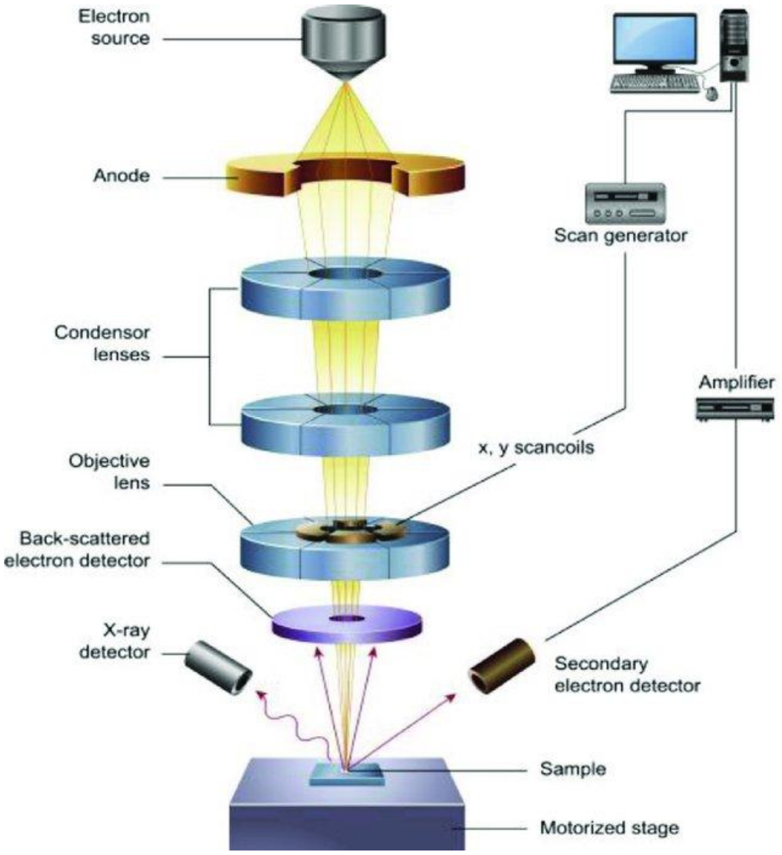

Figure 2.9 Simplified block diagram of a Scanning Electron Microscope (SEM): an electron gun generates a focused beam, refined by condenser and objective lenses, and directed in a raster pattern by X–Y scan coils.

2.7.2 Transmission Electron Microscopy

Electron microscopy is a fundamental tool for the nanoscale characterization of many materials, offering significantly higher resolution than traditional optical microscopy. This technique enables a detailed analysis of the morphological, chemical, and structural properties of samples, and has revolutionized fields such as materials science, biology, and physics.

A simplified diagram illustrating image formation in TEM mode is shown in Figure 2.10. A beam of electrons is transmitted through a thin sample held under high vacuum, generating an image. The incident electrons are focused onto the sample by condenser lenses, while the objective lens forms an initial inverted image. Subsequently, intermediate and projector lenses further magnify the image, which is acquired by a Charge-Coupled Device (CCD) camera.

In conventional TEM, image intensity is related to the amplitude of the electron wave, which is modified by the interaction of electrons with the atoms in the sample. Amplitude contrast arises from variations in the diffracted intensity, caused by absorption, dynamic scattering, and microstructural features.

The TEM can also be used in diffraction mode to obtain crystallographic information. In this configuration (Figure 2.10b), the power of the intermediate lens is adjusted to visualize the electron diffraction pattern. **Selected Area Diffraction (SAD)** images are acquired using an aperture that selects a region of interest in the sample and reduces the electron beam intensity, preventing damage to the CCD camera.

This approach allows determining the grain orientation, identifying the present phases, and measuring the characteristic d-spacings. In well-aligned crystalline samples, diffraction spots appear sharp and bright, while structural distortions such as stacking faults or lattice parameter variations result in broader or more diffuse reflections.

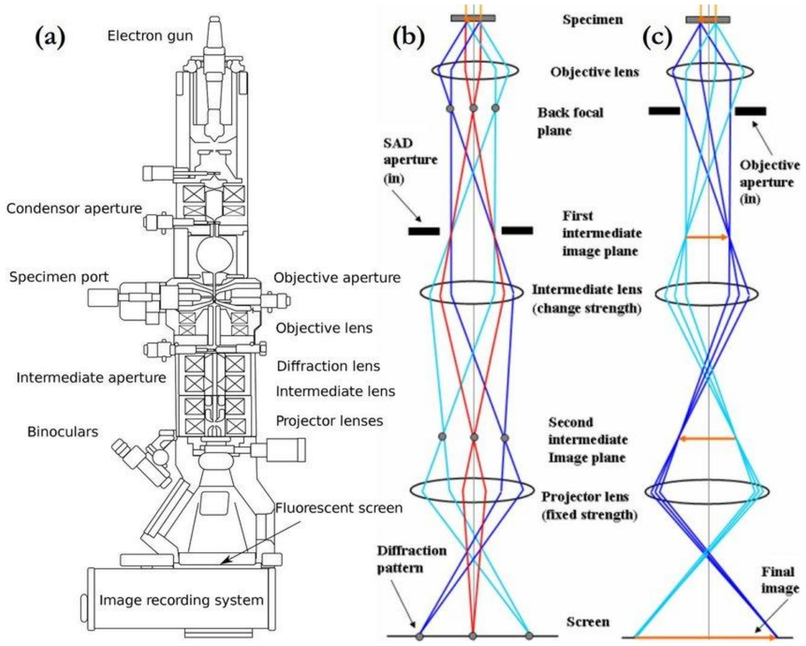

Figure 2.10 Simplified schematic of a Transmission Electron Microscope (TEM) column with beam path diagrams for both imaging and diffraction modes: (a) shows the overall layout—electron gun, condenser aperture and lenses, specimen stage, objective/intermediate/projector lenses, and the imaging/diffraction detectors. (b) and (c) illustrates the electron trajectories: on the left, the path for forming a diffraction pattern at the back focal plane of the objective lens; on the right, the path for imaging mode, where the transmitted beam is focused and magnified through subsequent lenses onto the imaging plane.

2.7.3 Scanning Transmission Electron Microscopy

In STEM mode, the electron beam is focused into a fine probe that scans the specimen. Images are acquired using diverse types of detectors, depending on the scattering angle considered and on the type of physical information to be obtained from the analysis. We can therefore cite:

- **Bright Field (BF):** Collects electrons transmitted directly through the sample. The resulting images reflect the local electron density, with denser areas appearing darker.
- **Annular Dark Field (ADF):** Collects scattered or diffracted electrons at medium angles. These images provide contrast based on electron scattering, which is influenced by the sample's structure and composition.
- **High-Angle Annular Dark Field (HAADF):** Collects electrons scattered at high angles. The resulting images offer mass-thickness contrast (Z-contrast), making them particularly useful for highlighting local variations in atomic number (Z), with higher-Z areas appearing brighter.

- **High-resolution imaging (HR)**: can be performed in both TEM and STEM modes. HR-TEM relies on phase contrast and is highly dependent on focus and sample thickness. In contrast, HR-STEM—using, for instance, high-angle detectors—enables the acquisition of mass-contrast images at high magnification.

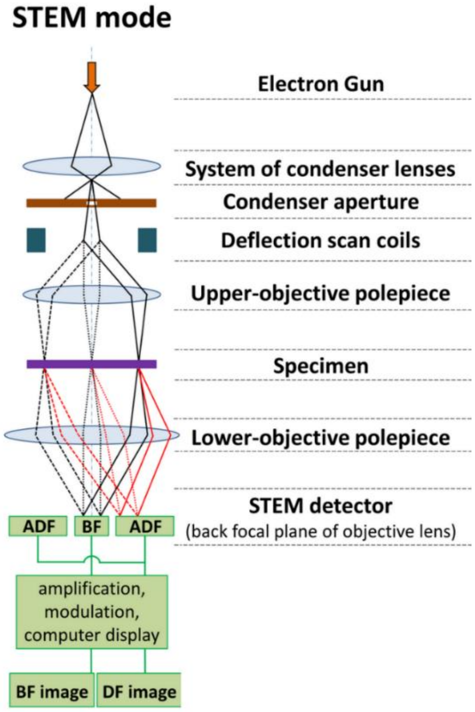

Figure 2.11 Schematic representation of the operating principle in STEM mode. The focused electron probe is scanned across the sample, and the transmitted electrons are collected by different detectors to obtain images under various contrast conditions.

Electron microscopy techniques, especially STEM, are often combined with analytical tools such as Energy Dispersive X-ray Spectroscopy (EDS) and Electron Energy Loss Spectroscopy (EELS).

These allow for elemental and chemical mapping at the nanoscale, providing crucial information about composition and electronic structure, in combination with morphological and crystallographic data.

ABSTRACT OF CHAPTERS III AND IV

In the third chapter, a comprehensive discussion will be presented regarding the research activities conducted on the HTS based on YBCO, epitaxially deposited on a $SrTiO_3$ (STO) substrate. The structural and electrical properties of the material will be described in detail, along with the deposition technique used, namely DC sputtering. The substrate preparation phase will also be covered, focusing on chemical treatments aimed at promoting homoepitaxial growth of the superconducting film.

Electrical characterization will be conducted using the Van der Pauw method, measuring resistivity as a function of temperature to verify the presence of the superconducting transition and to compare it with expected values for YBCO-based material. Experimental results will be shown through R(T) graphs, from which the T_c of the examined sample can be identified.

The crystal structure of the film will be evaluated by X-ray diffraction (XRD) analysis, with diffraction patterns reported and discussed, paying particular attention to the preferential grain orientation and any presence of secondary phases.

Following this, surface morphological analyses of the film will be presented using scanning electron microscopy (SEM), useful for assessing surface roughness, the presence of secondary particles or defects, and growth uniformity.

The preparation methods for samples analysed by transmission electron microscopy (TEM), conducted using Focused Ion Beam (FIB) to obtain cross-sections of the YBCO/STO film, will also be described. The obtained TEM images will be thoroughly analysed, including observations made in Scanning Transmission Electron Microscopy (STEM) mode, to highlight possible structural defects, the quality of the film/substrate interface, and the distribution of crystal planes within the material.

Finally, analyses performed by off-axis holography technique will be described, with observations conducted both at room temperature and at low temperatures. These analyses will allow studying the material’s behaviour from the perspective of internal electrostatic potential and possible magnetic fields, thus providing a more complete view of the functional properties of the superconductor.

In chapter IV, the focus will shift to the investigation of the superconducting thin film based on Fe(Se,Te), deposited on two different substrates. This chapter will cover the deposition technique employed, as well as the rationale behind the choice of the two distinct substrates for comparison, including the use of auxiliary materials to optimize film growth and properties.

The preparation of samples for Transmission Electron Microscopy (TEM) and Scanning Transmission Electron Microscopy (STEM) analyses will be described, with particular emphasis on the mechanical thinning method used to obtain electron-transparent regions suitable for detailed microstructural characterization.

Comprehensive TEM and STEM analyses will be presented, revealing the microstructure and crystallinity of the Fe(Se,Te) films on the different substrates. Elemental composition and chemical state will be investigated through Energy Dispersive X-ray Spectroscopy (EDX) and Electron Energy Loss Spectroscopy (EELS), providing insight into the film's chemical homogeneity and elemental distribution.

3. YBCO SUPERCONDUCTING FILM

3.1 Superconducting Materials

Yttrium barium copper oxide ($YBa_2Cu_3O_{7-x}$), commonly referred to as YBCO or Y123 (from the stoichiometry of yttrium, barium, and copper), is a high-temperature superconductor that crystallizes in a layered, perovskite-derived structure with variable oxygen content. The oxygen stoichiometry ($7-x$) strongly affects its crystal symmetry and electronic doping: the oxygen-rich, orthorhombic phase ($x \approx 0$) is superconducting with $T_c \approx 92$ K, whereas oxygen depletion drives a transition toward a non-superconducting tetragonal phase. YBCO was the first material found to exhibit superconductivity above the boiling point of liquid nitrogen (77 K), marking a breakthrough in the field. [42].

The superconducting properties of YBCO are strongly dependent on the oxygen content (x). At optimal doping, when $x \approx 0.15$, the structure is orthorhombic, and the T_c reaches a maximum of approximately 93 K [18]. In this regime, the Cu–O chains play a critical role in hole-doping the CuO_2 planes, which is essential for superconductivity. As oxygen is removed, the disruption of the Cu–O chains reduce the hole concentration and suppresses superconductivity. When x exceeds roughly 0.5–0.6, the compound undergoes a transition toward the tetragonal phase [43], in which the Cu–O chains are largely destroyed, and the material becomes non-superconducting.

The crystal structure of Y123, shown in Fig. 3.1, can be described as a triple perovskite, composed of a central CuO_2–Y–CuO_2 layer (conduction block) and two outer CuO_2–BaO–CuO layers (charge reservoir blocks). The presence of both CuO_2 planes and Cu–O chains is fundamental to achieving high-T_c superconductivity [44].

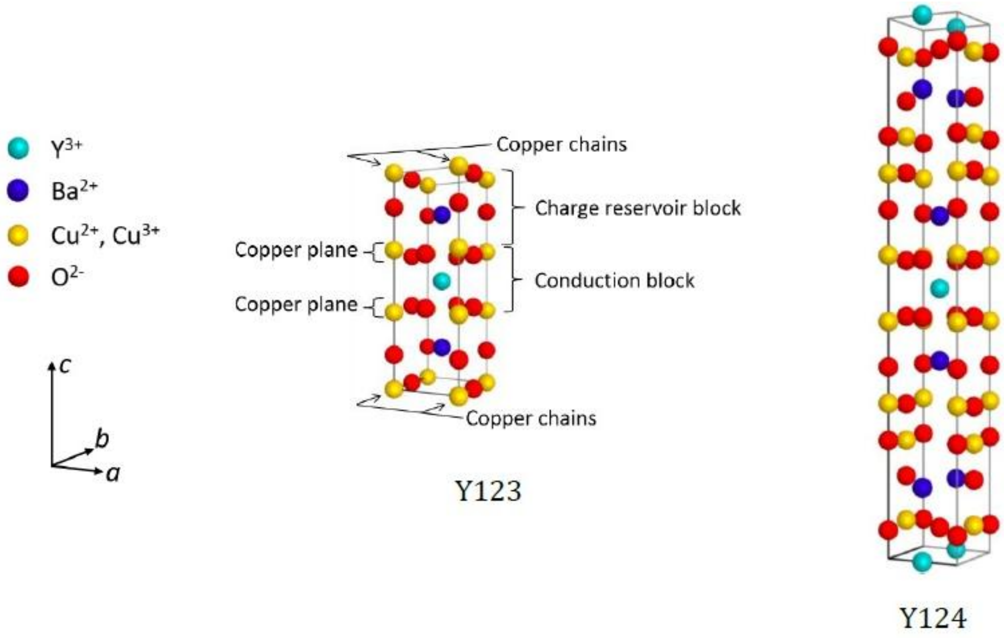

Figure 3.1 Crystal structures of the $YBa_2Cu_3O_{7-x}$ (Y123) and $YBa_2Cu_4O_8$ (Y124) HTS.

In addition to the Y123 structure, other configurations can also be encountered, such as Y124. This is a derivative of Y123, featuring two Cu–O planes between the Y123 units and a different stacking of the unit cells, as shown in Fig. 3.1. These structural modifications can influence both the electronic properties and the superconducting behaviour of the material.

Unlike conventional superconductors, the mechanism of superconductivity in YBCO is not fully explained by BCS theory. It is believed to arise from strong electron correlations and spin fluctuations, making it an example of unconventional superconductivity.

3.2 Structural and Superconducting Properties of $YBa_2Cu_3O_{7-x}$ Thin Films Grown on $SrTiO_3$

$YBa_2Cu_3O_{7-x}$ (YBCO) is one of the most extensively studied high-temperature superconductors, owing to its relatively high superconducting transition temperature ($T_c \approx 90$ K), chemical stability, and suitability for thin-film growth [45].

Among the various substrates employed for epitaxial growth, $SrTiO_3$ (STO) has emerged as a model system due to its perovskite structure, close lattice match, and well-defined surface terminations.

As a result, YBCO/STO heterostructures constitute a benchmark platform for investigating the interplay between epitaxial strain, microstructure, and superconducting properties in cuprate thin films, as well as for the development of superconducting electronic devices. [46]

3.3 Structural Compatibility and Epitaxy

STO crystallizes in a cubic perovskite structure with a lattice parameter of approximately 3.905 Å, which provides a reasonable lattice match to the in-plane lattice constants of orthorhombic YBCO.

This compatibility promotes high-quality epitaxial growth, typically with the YBCO c-axis oriented perpendicular to the STO (001) substrate surface. X-ray diffraction and transmission electron microscopy studies consistently report well-defined epitaxial relationships. [47]

Despite the relatively small lattice mismatch, epitaxial strain plays a significant role, particularly in ultrathin films. For thicknesses below approximately 10–15 nm, YBCO films may experience partial suppression of orthorhombicity, tending toward a more tetragonal-like structure.

As the film thickness increases, strain relaxation mechanism, such as misfit dislocations, allow the lattice parameters to approach their bulk values, restoring full orthorhombic symmetry.

3.4 Growth Techniques and Microstructural Features

Direct current (DC) sputtering is a widely employed technique for the growth of YBCO thin films, owing to its good thickness uniformity, scalability, and compatibility with large-area deposition. When optimized growth conditions are adopted—typically involving substrate temperatures in the range of 700–800 °C and controlled oxygen partial pressures during deposition and post-annealing—DC sputtering enables the growth of epitaxial YBCO films with high crystalline quality and well-defined interfaces. [48]

To investigate the structural quality of these epitaxial films, high-resolution TEM studies have revealed atomically abrupt YBCO/STO interfaces, although interfacial reconstruction and local chemical rearrangements have been reported, particularly depending on whether the STO surface is TiO_2- or SrO-terminated. Structural defects such as stacking faults, anti-phase boundaries, and twin domains are frequently observed, reflecting both the orthorhombic nature of YBCO and the strain accommodation mechanisms operative during growth. These microstructural features are known to influence vortex pinning and current transport properties. [49]

3.5 Superconducting Properties

3.5.1 Superconducting Transition Temperature

One of the key advantages of STO as a substrate is the ability to achieve superconducting transition temperatures close to the bulk value of optimally oxygenated YBCO. High-quality films typically exhibit Tc values in the range of 88–92 K, with narrow transition widths ($\Delta T_c \lesssim 1$ K), indicating good homogeneity and oxygenation.

In ultrathin films, however, a systematic suppression of Tc is often observed. This reduction has been attributed to a combination of factors, including epitaxial strain, reduced dimensionality, disorder, and modifications of the oxygen sublattice near the interface. The sensitivity of Tc to structural distortions underscores the strong coupling between lattice parameters and electronic properties in cuprate superconductors. [50].

3.5.2 Critical Current Density

The critical current density (J_c) is a crucial figure of merit for both fundamental studies and technological applications. Epitaxial YBCO films on STO routinely exhibit J_c values exceeding 10^6 A/cm^2 at 77 K in self-field conditions. Such high values are indicative of excellent crystalline quality and strong flux pinning. [51].

Microstructural defects inherent to epitaxial growth, such as twin boundaries and threading dislocations can act as effective pinning centers, enhancing J_c under applied magnetic fields. Conversely, excessive defect densities or poorly controlled interfaces may degrade current transport, highlighting the need for precise control over growth parameters and film thickness. [52].

3.6 Role of Epitaxial Strain

Epitaxial strain imposed by the STO substrate has a profound impact on both the structural and superconducting properties of YBCO films. Strain-induced modifications of the CuO_2 plane spacing and Cu–O bond lengths can alter the electronic bandwidth and carrier concentration, thereby influencing T_c and the superconducting gap. [53].

3.7 Substrates

A variety of single-crystal substrates are used for the epitaxial growth of high-T_n superconducting films.

Pseudo cubic or perovskite oxides such as $YAlO_3$(110) (YAO), $LaAlO_3$(001) (LAO) and $(LaAlO_3)_{0.3}(Sr_2TaAlO_6)_{0.7}$(001) (LSAT) exhibit in-plane lattice constants (3.71–3.87 Å) closely matching those of YBCO and many iron-based superconductors, thereby reducing lattice mismatch to below approximately 2 % and promoting homogeneous, defect-free film growth [54]. Spinel and rock-salt substrates like $MgAl_2O_4$ (001) (MAO) and MgO (001), while presenting a slightly larger mismatch (5–9 %), offer excellent chemical and thermal stability at typical deposition temperatures.

Among all these options, $SrTiO_3$ (001) was selected as the substrate for this work due to its near-ideal lattice match with YBCO, excellent chemical and thermal stability under growth conditions, and its widespread availability in high crystalline quality.

This substrate is primarily characterized by a cubic perovskite crystal structure. At room temperature, it behaves as a paraelectric material but undergoes a ferroelectric phase transition at low temperatures.

The unit cell of STO is shown in Fig. 3.2. Sr ions occupy the corners of the cubic cell, the Ti ion is located at the center of the cell, and O ions are positioned at the centers of the faces. Along the (001) direction, the crystal consists of an alternating sequence of SrO and TiO_2 layers.

From an application standpoint, STO is widely used for the growth of thin oxide films, such as YBCO (Yttrium Barium Copper Oxide). Thanks to its lattice constant of approximately 3.905 Å—which closely matches the lattice constant of YBCO, around 3.89 Å at room temperature—it is possible to achieve epitaxial growth of this superconducting material on STO without significant crystalline dislocations [55].

The substrate used for the deposition of these films was purchased from the company **Crystal** and is a 10x10x1 mm^3, one side epi polished.

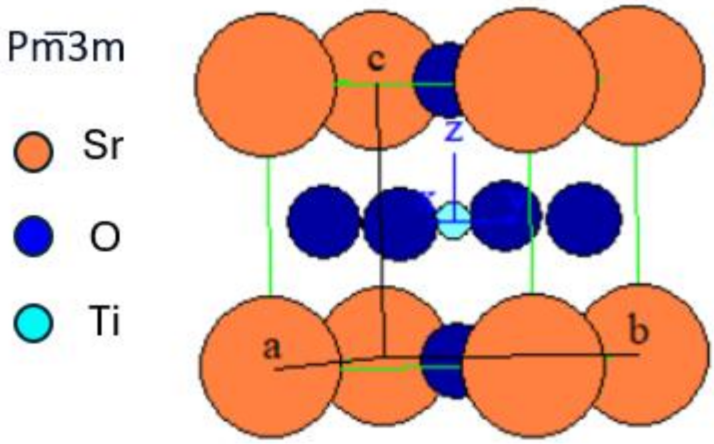

Figure 2.8 Simplified schematic cross-sections of an (a) SEM, (b) TEM and (c) STEM instrument.

3.8 Etching process

$SrTiO_3$ (STO) surfaces can be terminated with either a TiO_2 or SrO layer or may exhibit a mixed termination. However, to obtain a homoepitaxially grown YBCO thin film, it has been demonstrated that not only does the presence of an SrO termination drastically reduce the interfacial conductivity [56], but it also leads to the formation of a film characterized by island growth.

Consequently, it becomes clear that optimizing the chemical preparation of $SrTiO_3$ (STO) substrate surfaces is crucial to obtain atomically flat step-and-terrace surfaces with a single termination (TiO_2 or SrO), which are essential for the growth of high-quality epitaxial films.

Specifically, for the samples examined here, obtaining a surface rich in TiO_2 termination is preferable, as it facilitates the formation of oxygen vacancies and may promote electronic phenomena; SrO termination, on the other hand, inhibits these processes and may hinder regular epitaxial growth.

A substrate with a random (mixed SrO/TiO_2) termination leads to non-homoepitaxial growth of the overlying film, resulting in the formation of inhomogeneous grains and island growth.

To prepare such atomically flat surfaces with a single, controlled TiO_2 termination, etching techniques can be applied using acids or acidic solutions such as HNO_3, HCl, or NH_4-HF solutions.

Moreover, it should be noted that the various crystallographic orientations of STO ((100), (110), (111)) react anisotropically to etching: etch rates, pit formation, and under etching vary with orientation and the possible presence of defects. Therefore, identifying the optimal etching formula capable of producing a substrate as suitable as possible for superconducting film deposition is of utmost importance [57].

In the specific case of the substrate used for the samples described here, we treated an STO (100) substrate with HF at pH 4.4, as widely reported in the literature [58;59]. A schematic representation of the etching process is shown in Figure 3.3.

More specifically, to evaluate the proper exposure to the exfoliating action of the acid used and the resulting surface termination, two different durations were tested:

- Etching longer than 10 seconds
- Etching of only 10 seconds

This was done immediately after the standard substrate cleaning process, consisting of:

- Immersion in deionized water and sonication for 10 minutes

- Drying with nitrogen flow
- Immersion in propanol and sonication for 10 minutes
- Drying with nitrogen flow to remove any impurities and debris generated during the substrate cutting process.

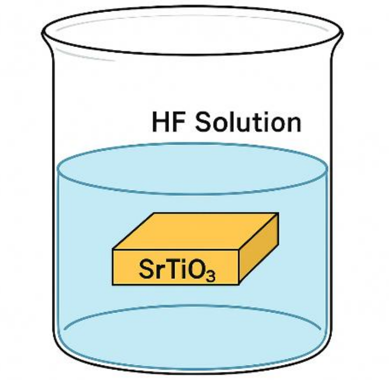

Figure 2.9 Simplified block diagram of a Scanning Electron Microscope (SEM): an electron gun generates a focused beam, refined by condenser and objective lenses, and directed in a raster pattern by X–Y scan coils.

The etching process, under both conditions listed above, caused an opacification of the epi-polished surface of the substrate. However, in the case of the 10-second etch, the surface brightness was restored by repeating the post-etching cleaning process. In contrast, this restoration did not occur for the substrate subjected to prolonged etching.

3.9 Evaluation of Superconducting Properties: Van der Pauw Method

The resistivity measurements, carried out using the Van der Pauw method described in Paragraph 2.2, were performed at the CNR-SPIN laboratories in Salerno, using a Cryogenic Ltd. cryogenic measurement system equipped with a variable temperature insert operating in the 1.6–300 K range, with a temperature stability of 0.01 K, and a superconducting magnet capable of generating fields up to 16 T.

According to the literature, the R(T) curves of YBCO films typically show a nearly linear behaviour (or a plateau) in the normal state up to temperatures close to the transition; as the temperature decreases, the resistivity rapidly drops around 88–92 K [60]. The samples analysed here, however, do not always exhibit this reference trend (see Graph 3.1), and the measured T_c values vary among those reported in Table 3.1.

Graph 1 shows the comparison of resistivities normalized to their values at 100 K as a function of temperature for the different samples listed in Table 1. Normalization at 100 K, which is above the superconducting transition of YBCO (~90–92 K), allows easy comparison of the relative changes in resistivity among the samples while ensuring that the material is in the normal phase.

As can be observed, only four samples show a curve trend close to the expected one, although one of them is the sample labelled Smp$_{\mathbf{LE}}$, as reported in Table 3.1.

Sample MLY#6, on the other hand, shows a trend far from the expected value, even though it underwent the same procedures as the other samples; this result could be attributed to the fact that the cooling process was not always carried out at 4 °C. From Graph 1, the three curves corresponding to the samples analysed in this thesis were extracted. The corresponding curves are shown in the underlying Graph 3.2.

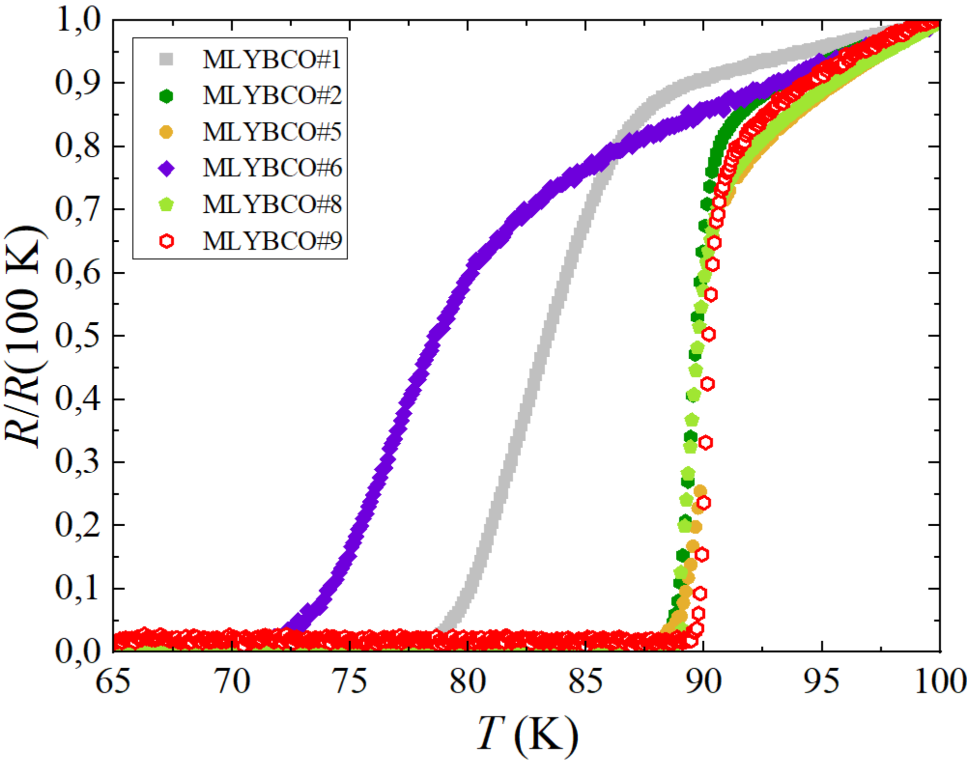

Graph. 3.1 Normalized resistivity at 100 K as a function of temperature for the different samples analyzed.

The electrical transport measurements clearly reveal that substrate surface preparation has a profound impact on the superconducting transition characteristics of YBCO films. Films grown on etched substrates exhibit sharper superconducting transitions and critical temperatures approaching the bulk value of YBCO (~92 K), whereas films grown on non-etched substrates show a marked degradation of superconducting properties.

It can be observed that Smp_**NE** (grey line) reaches a T_c^0 of 78.4 K, with a sigmoidal drop occurring well before the expected T_c.

For Smp_**LE** (Graph 3.2, green line), the measured R(T) values are closer to the expected T_c, with a T_c^0 of 87.7 K.

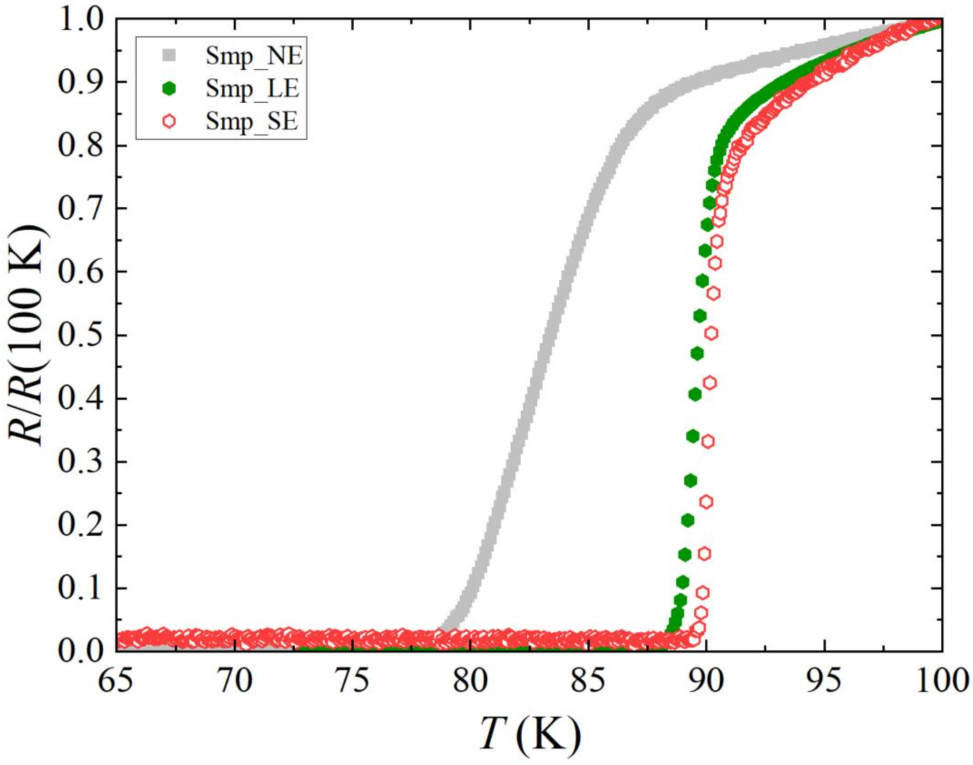

Graph. 3.2 Normalized resistivity at 100 K as a function of temperature for the three most representative samples.

Smp$_{SE}$ (Graph 3.2, red line), corresponding to the sample grown on a short-etched substrate, exhibits the most favourable superconducting behaviour, with a sharp transition and a measured T_{c0} of 89.5 K, which is the closest to the expected bulk value. This result indicates that controlled substrate etching leading to optimal surface termination is crucial for obtaining high-quality YBCO films with superior superconducting performance.

To fully assess the homogeneity of the samples, the width of the superconducting transition, ΔT, is determined. This is defined as the difference between two T_c values calculated according to different criteria, depending on the parameters considered and the chosen measurement technique. The most common definitions are $\Delta T = T_c^{\,onset} - T_c^{\,offset}$ or the difference between temperatures corresponding to 90% and 10% of the resistivity drop. Other approaches, such as using derivatives of the resistivity or magnetic susceptibility curves, sigmoidal fitting, or calorimetric measurements, are also employed in literature to characterize the transition width and the sample homogeneity.

In this work, the determination of ΔT, i.e., the transition width, was carried out according to the 90%–10% criterion, which measures the transition width using two relative points on the $R(T)$ curve, as shown in Grap. 3.3. The analysed points are defined as:

- **$T_{90\%}$**: the temperature at which the resistance $R(T)$ equals 90% of the normal-state resistance R_n.
- **$T_{10\%}$**: the temperature at which the resistance $R(T)$ equals 10% of R_n.

The determination of $\Delta T = T_{90}\% - T_{10}\%$ thus allowed for the analysis of the sample homogeneity and a discussion of the effects of irradiation on the quality of the transition.

A similar approach is systematically adopted in the literature for the determination of T_c [59].

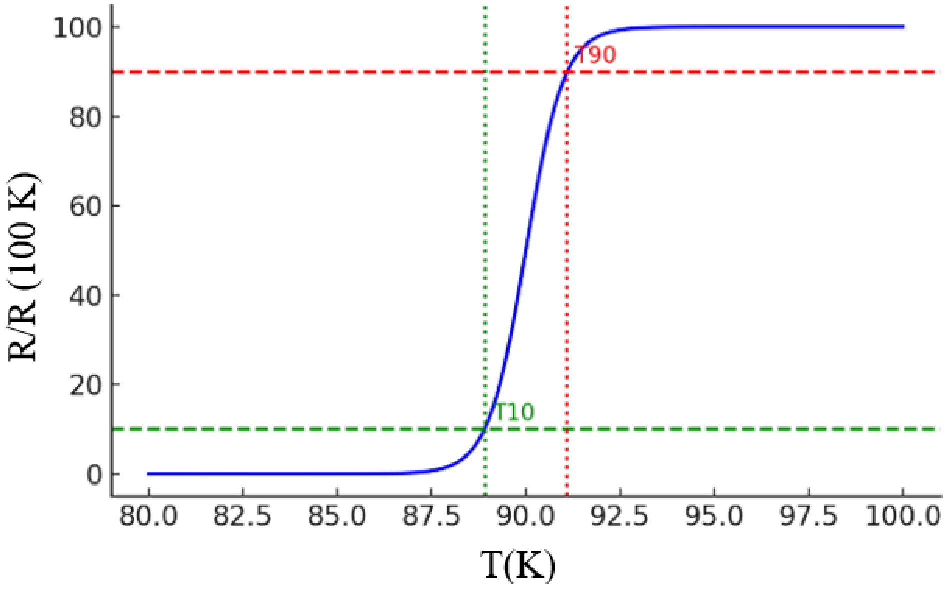

Graph. 3.3 Example of a normalized resistivity curve highlighting the temperatures corresponding to 90% ($T_{90\%}$) and 10% ($T_{10\%}$) of the normal-state resistivity.

The importance of this parameter lies in the fact that ΔT values ≤ 2 K indicate that the transition from the normal to the superconducting state occurs over a very narrow temperature range, suggesting a film grown uniformly, with consistent thickness, low defect density, and optimal superconducting properties. However, a transition spread of a few degrees still indicates a well-oxygenated and largely homogeneous film, although local defects or slight composition gradients may be present. Films with ΔT between 2 and 5 K are still considered of high quality [61]. To obtain a reduced ΔT, the oxygen-annealing protocol can be optimized, or the deposition parameters, such as substrate temperature, chamber pressure, and growth rate, can be fine-tuned. The values for the samples analysed in this work are reported in Table 3.1.

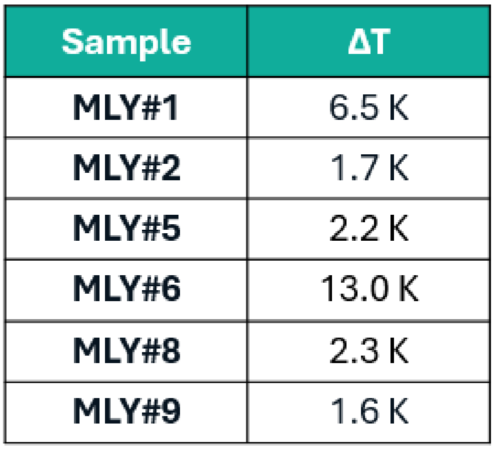

Sample	ΔT
MLY#1	6.5 K
MLY#2	1.7 K
MLY#5	2.2 K
MLY#6	13.0 K
MLY#8	2.3 K
MLY#9	1.6 K

Table 3.1 ΔT values of the deposited samples.

3.10 Lithographically patterned samples

As shown in the Figure 3.4, two bridges of different widths were fabricated on Smp_SE: one 50 µm wide and one 100 µm wide. The first bridge was not subjected to irradiation, while the second was irradiated to study the material's behaviour before and after irradiation.

After lithography, performed according to the procedure described at the beginning of this paragraph, the sample was re-evaluated for its R(T) behaviours using the Van der Pauw method.

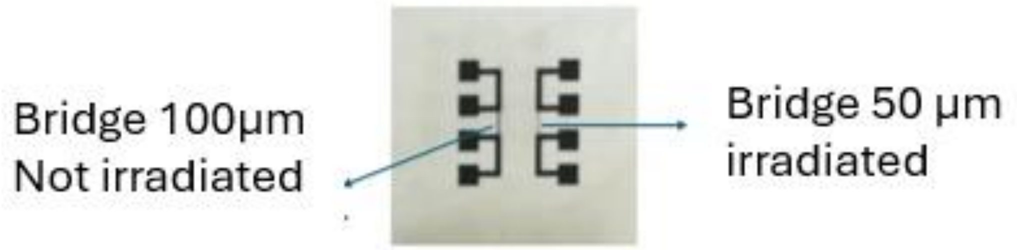

Figure 3.4 Mask applied to the sample. We observe the presence of two different bridges, measuring 100 and 50 micrometres respectively.

In Graph.3.4, we can observe the comparison between the R(T) curves of Smp_SE before and after lithography, as well as before and after irradiation. As can be seen from the graph 4, the comparison of the R(T) curves shows an almost identical behaviour, highlighting the high quality of the sample and its ability to maintain superconducting properties even after irreversible processes such as lithography.

The T_c was determined from the resistance versus temperature curves of the analysed samples. The measured T_c and ΔT values, before and after irradiation (abbreviated as Smp$_{\mathbf{SE\_N.I.}}$ for *not irradiated* and Smp$_{\mathbf{SE\_I.}}$ for *irradiated*), are reported in Table 3.2.

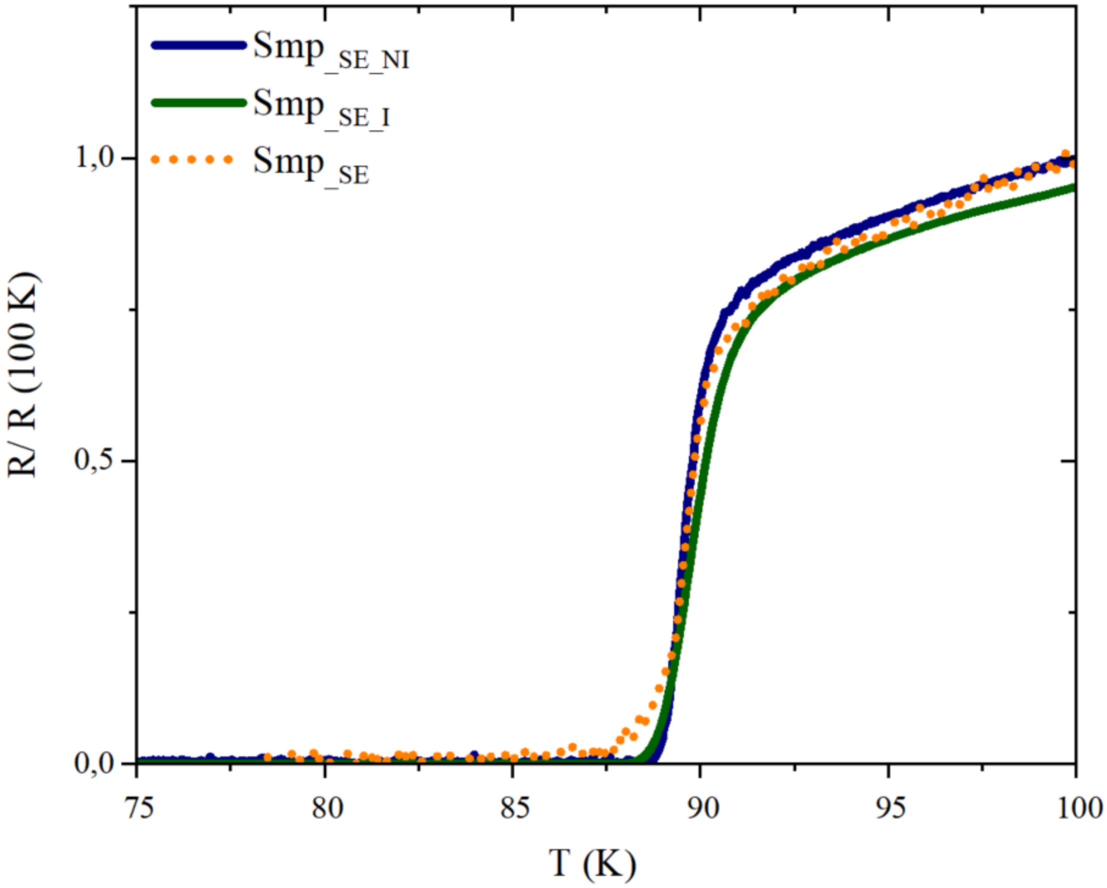

Graph. 3.4 Normalized resistivity at 100 K as a function of temperature for the Smp_SE sample before lithography (yellow dotted line), after lithography without irradiation (blue solid line), and after lithography with irradiation (green solid line).

The comparison between sample Smp$_{\_SE}$ without a bridge and the Smp$_{\mathbf{SE\_N.I.}}$ bridge and Smp$_{\mathbf{SE\_I}}$ bridge samples shows an increase in ΔT, attributable to the higher internal disorder in the film, in agreement with the expected behaviour.

However, after irradiation a reduction in T_c would also be expected [62]; instead, a slight increase was observed. This result can be ascribed to the fact that the material was not optimized, leading to a lack of homogeneity in the obtained measurements.

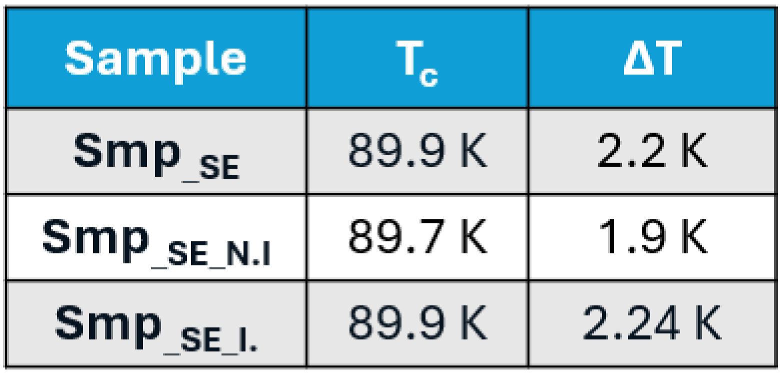

Sample	T_c	ΔT
Smp$_{\_SE}$	89.9 K	2.2 K
Smp$_{\_SE\_N.I}$	89.7 K	1.9 K
Smp$_{\_SE\_I.}$	89.9 K	2.24 K

Table 3.2 Critical temperature and ΔT for the three Smp_SE sample conditions: before lithography, after lithography without irradiation, and after lithography with irradiation

3.11 XRD

For the samples under investigation, X-ray diffraction measurements were routinely carried out in θ–2θ (Bragg–Brentano) geometry using a Panalytical X'Pert MRD PRO diffractometer in powder configuration. A dedicated sample holder mounted on the instrument allowed tilting of the specimen about an axis lying in the sample surface (ψ rotation, sometimes denoted χ) and rotation about the surface normal (φ rotation), covering ψ = 0°–90° (instrument- and holder-dependent) and φ = 0°–360°.

The obtained diffractogram is shown in Figure 3.5 and displays a comparison between the (00ℓ) reflections of Smp_$_{SE}$ (in black) and the signals of the STO substrate (in red), used as a reference for phase identification.

The YBCO peaks clearly indicate a pronounced **c-axis orientation**, aligned with the film’s growth direction. Moreover, the pattern shows no unassigned peaks or reflections attributable to phases other than YBCO or STO, which confirms the high phase purity of the deposited film. The film is thus characterized by **textured growth** with strong preferential orientation along the [001] direction.

To improve the precision in determining the lattice parameter *c*, a **Nelson–Riley plot** was constructed (Figure 3.6). In this graph, the *c* values calculated from the different (00ℓ) reflections are plotted as a function of the corresponding correction function *f(θ)*.

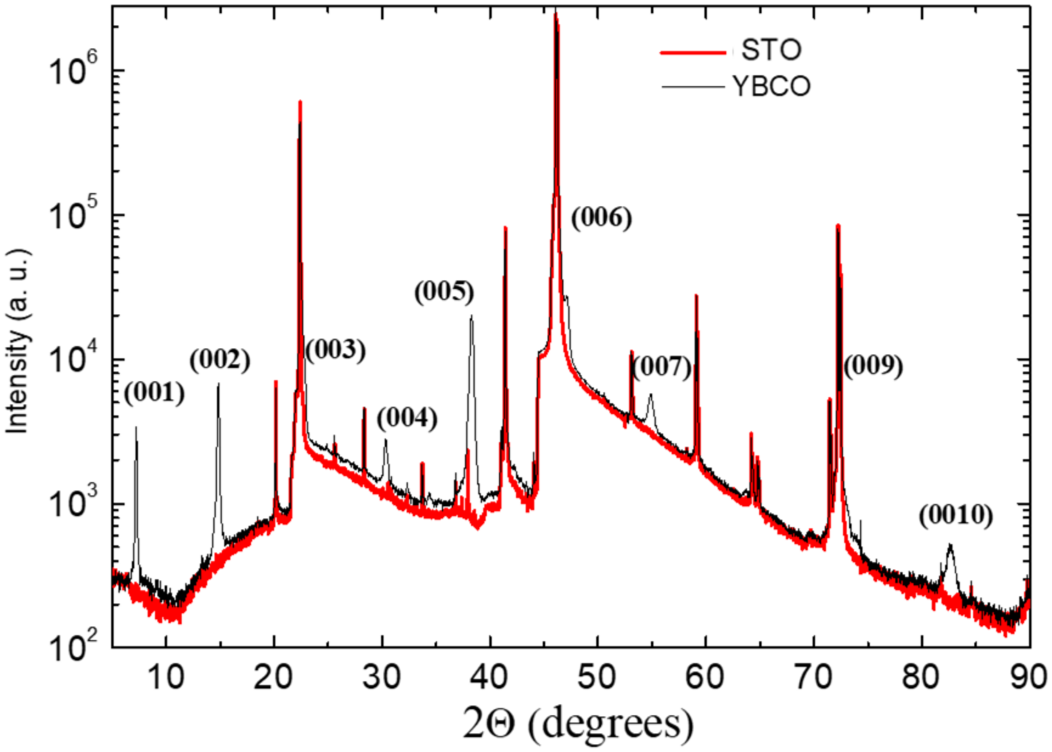

Figure 3.5 Comparison between the XRD pattern of the $SrTiO_3$ *substrate (red curve) and the characteristic reflections of the* $YBa_2Cu_3O_{7-x}$ *film (black peaks). The presence of (00l) reflections confirms the c-axis preferred orientation of the YBCO film.*

The good linearity of the experimental points allowed the extrapolation of the optimal *c* value at the intersection with the y-axis, thereby minimizing systematic errors related to instrumentation or measurement geometry. The resulting lattice parameter *c* is consistent with the expected value for well-oxygenated orthorhombic phase YBCO.

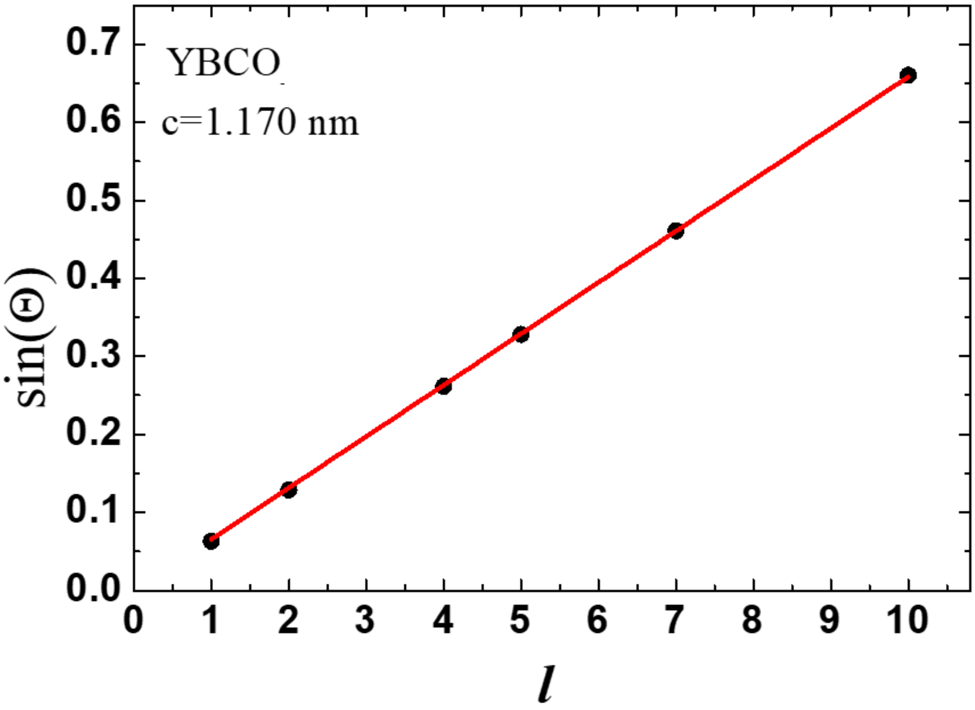

Figure 3.6 Nelson–Riley plot obtained from the (00l) reflections of $YBa_2Cu_3O_{7-x}$ *measured by X-ray diffraction in θ–2θ geometry. The linear extrapolation allows the accurate determination of the lattice parameter c by reducing angular-dependent systematic errors.*

3.12 Structural Analysis via SEM and TEM

To further investigate the morphological and structural properties of the YBCO film, SEM and TEM analyses were carried out on three selected samples. The choice of these samples, motivated by the results presented in Section 3.5, fell on those considered the most representative of the different growth conditions observed.

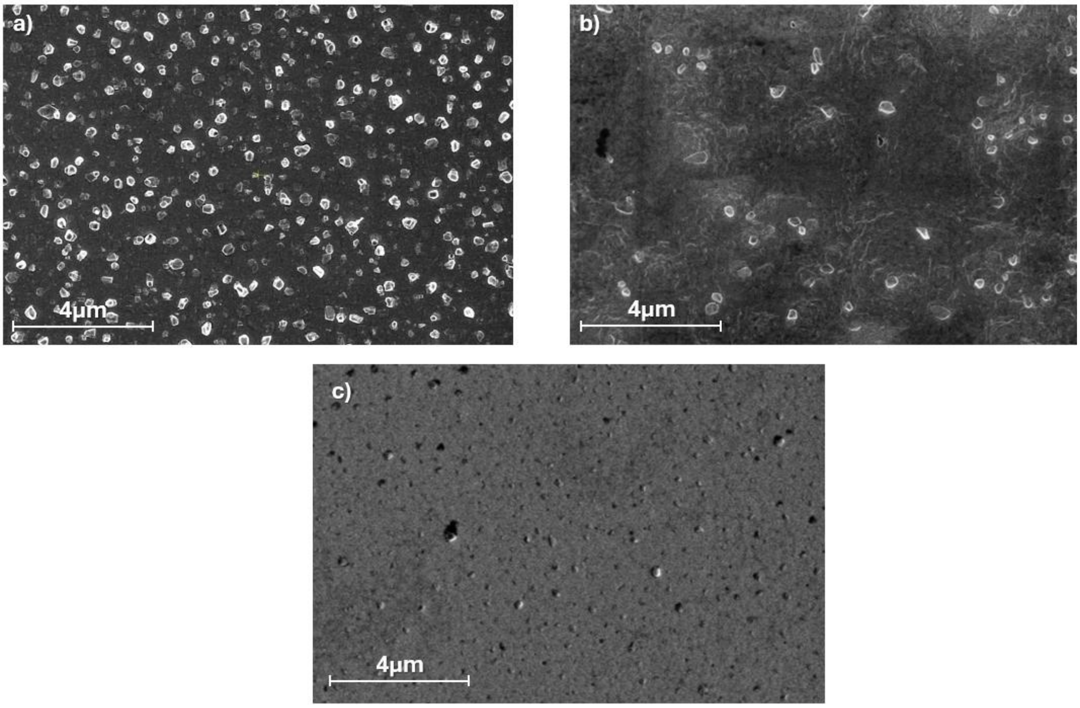

Figure 3.7 Top-view SEM images of the samples: a) non-etched sample (Smp$_{\_NE}$*), b) long-etched sample (Smp*$_{\_LE}$*),c) short-etched sample (Smp*$_{\_sE}$*).*

As shown in the SEM comparison of the surfaces of the three analysed samples (Fig. 3.7), in the **Smp$_{\_NE}$** sample (Fig. 3.7a) the YBCO film deposited on the unetched STO substrate exhibits a dense population of polycrystalline grains with jagged contours and irregular morphology. The grains appear well separated and non-uniformly distributed, while the film is overall continuous. The structural inhomogeneities observed at the micrometre scale are likely related to surface variations of the STO substrate.

In the **Smp_**$_{\mathrm{LE}}$ sample (Fig. 3.7b), the film surface appears more heterogeneous than in the previous case, with several high-contrast particles irregularly distributed. Pronounced surface terraces can also be observed, which are attributed to excessive substrate exfoliation caused by prolonged exposure to hydrofluoric acid during the etching process.

Finally, in the **Smp_**$_{\mathrm{SE}}$ sample, SEM images show a more homogeneous surface with a compact and regular background, resulting from the shorter HF exposure during etching. Numerous darker-contrast particles are visible, some irregularly aggregated; however, compared to **Smp_**$_{\mathrm{NE}}$ and **Smp_**$_{\mathrm{LE}}$, these particles are smaller, more uniformly distributed, and denser.

The average size and distribution of the particles in the three samples described above are reported in Table 3.3. The following sections will provide a more detailed discussion of the SEM and TEM analyses of the selected samples.

SAMPLE	AVERAGE PARTICLE SIZE (nm)	AVERAGE PARTICLE DENSITY (particles/μm^2)
$\mathrm{Smp}_{\_\mathrm{NE}}$	34,5	3,2
$\mathrm{Smp}_{\_\mathrm{LE}}$	22,2	0,7
$\mathrm{Smp}_{\_\mathrm{SE}}$	19,9	2,6

Table 3.2 Average particle size and average particle density of the three analysed samples, determined from SEM images

3.12.1 Smp$_{\_NE}$

Focusing on the analysed samples, in the **Smp$_{\_NE}$**, the 52°-tilted image (Fig. 3.8) highlights the three-dimensionality of the surface, showing pronounced surface islands indicative of incomplete epitaxial growth, characterized by varying heights and morphologies, in according to the Fig. 3.7a. This condition can be attributed to the random ratio of strontium oxide planes to titanium oxide planes on the substrate surface (SrO/TiO_2), which promotes the formation of multiple nucleation sites.

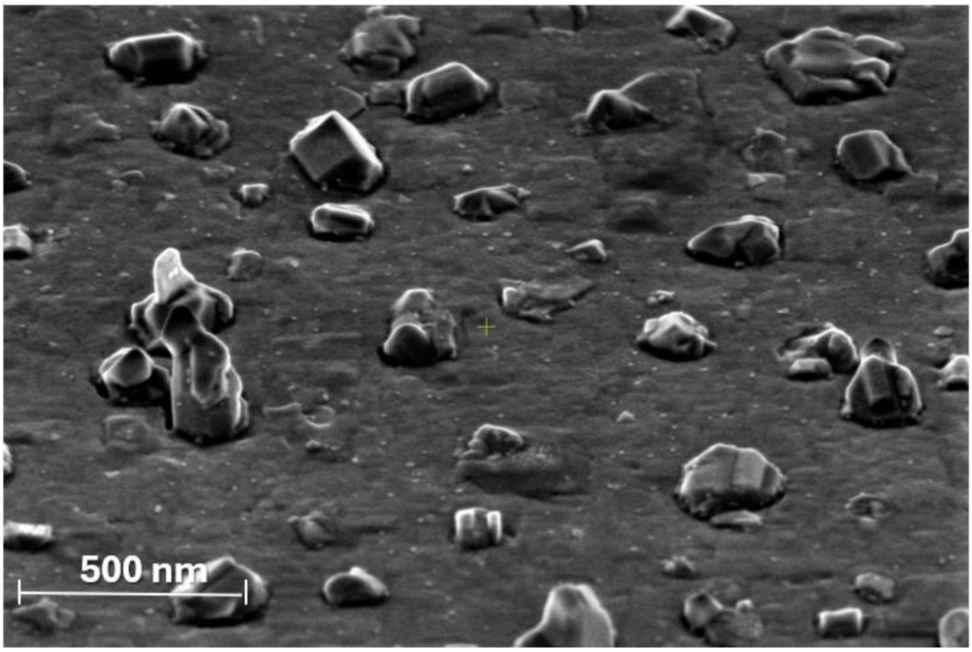

Figure 3.8 Tilted (52°) SEM image of the Smp$_{\_NE}$ sample surface. The inclination highlights the three-dimensional surface morphology.

Low-magnification TEM analysis made it possible to identify and characterize one of the grains observed in Fig. 3.8, located on the film surface. The identified grain (Fig. 3.9a) exhibits an irregular morphology. The selected-area electron diffraction pattern (SAED, in Figure 3.9b) reveals characteristic YBCO planes, such as [112] and [111]; however, the grain orientation is not consistent with the predominant epitaxial growth direction.

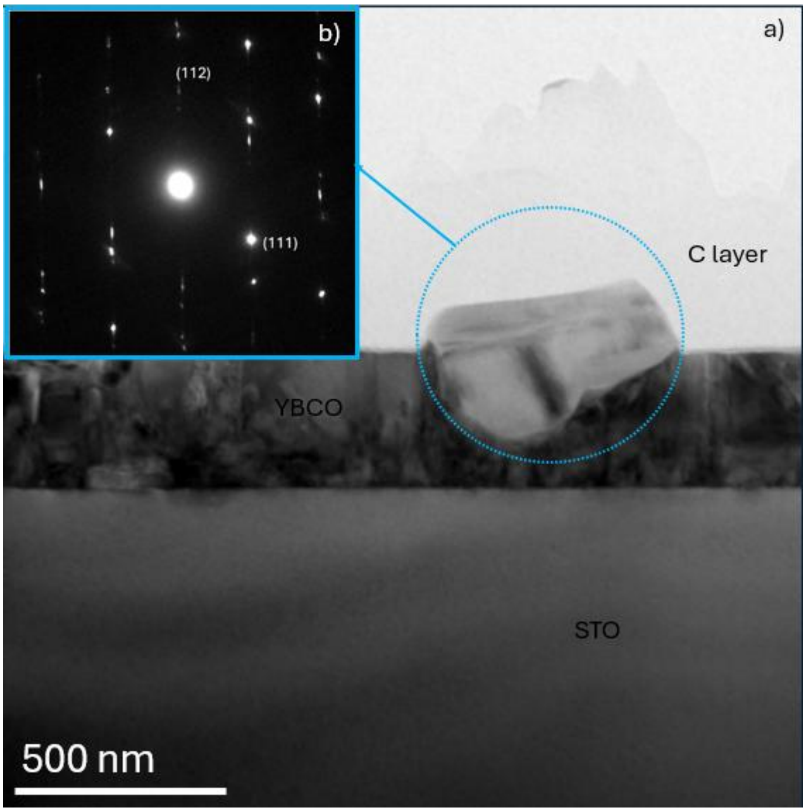

Figure 3.9 (a) TEM image showing the substrate, the film, and a grain located on the film surface. (b) Electron diffraction pattern of the grain with the corresponding plane indices.

From the lamella of the Smp$_{\_NE}$ sample (Fig. 3.10), it also emerges that the film is continuous and compact, with a thickness of approximately 170 nm. The slight local contrast variations can be attributed to columnar structures with different orientations.

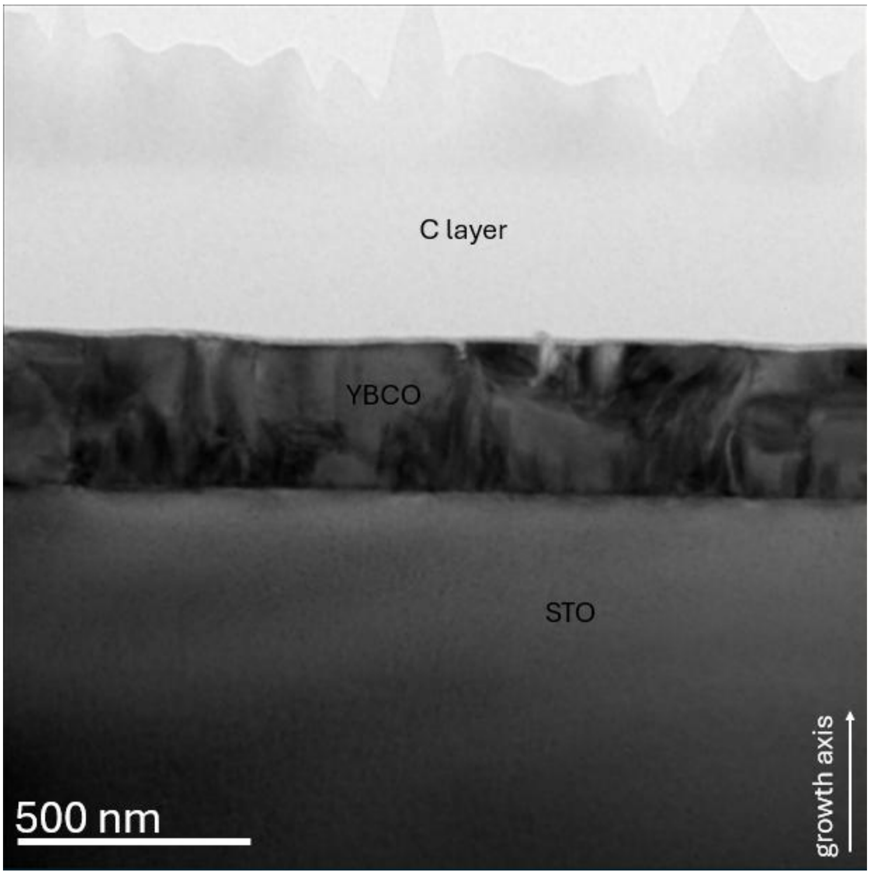

Figure 3.10 Cross-sectional TEM image at low magnification showing the substrate, the film, and the protective carbon layer (C layer). A good film–substrate adhesion is observed, with no evidence of interfacial defects or delamination.

At higher magnification, FFT analysis (Fig. 3.11) confirms the coexistence of multiple orientations at the nanoscale. Examination of these selected film regions allows distinguishing different crystallographic orientations: in some areas, the film shows the c-axis of YBCO crystal, aligned along the growth direction predominates (Fig. 3.11a), while in others the c-axis is orthogonal to the growth direction and lie on the film plane, and is aligned along the film/substrate interface as in fig (Fig. 3.11b) or along the e-beam direction. In some regions of the sample these two crystal orientations overlaps, as evidenced by the FFT patterns in Fig. 3.11c.

Despite the differences in orientation, regions with c-axis parallel or perpendicular to the growth direction, a correlation between the local crystal structure and the macroscopic film orientation is evident.

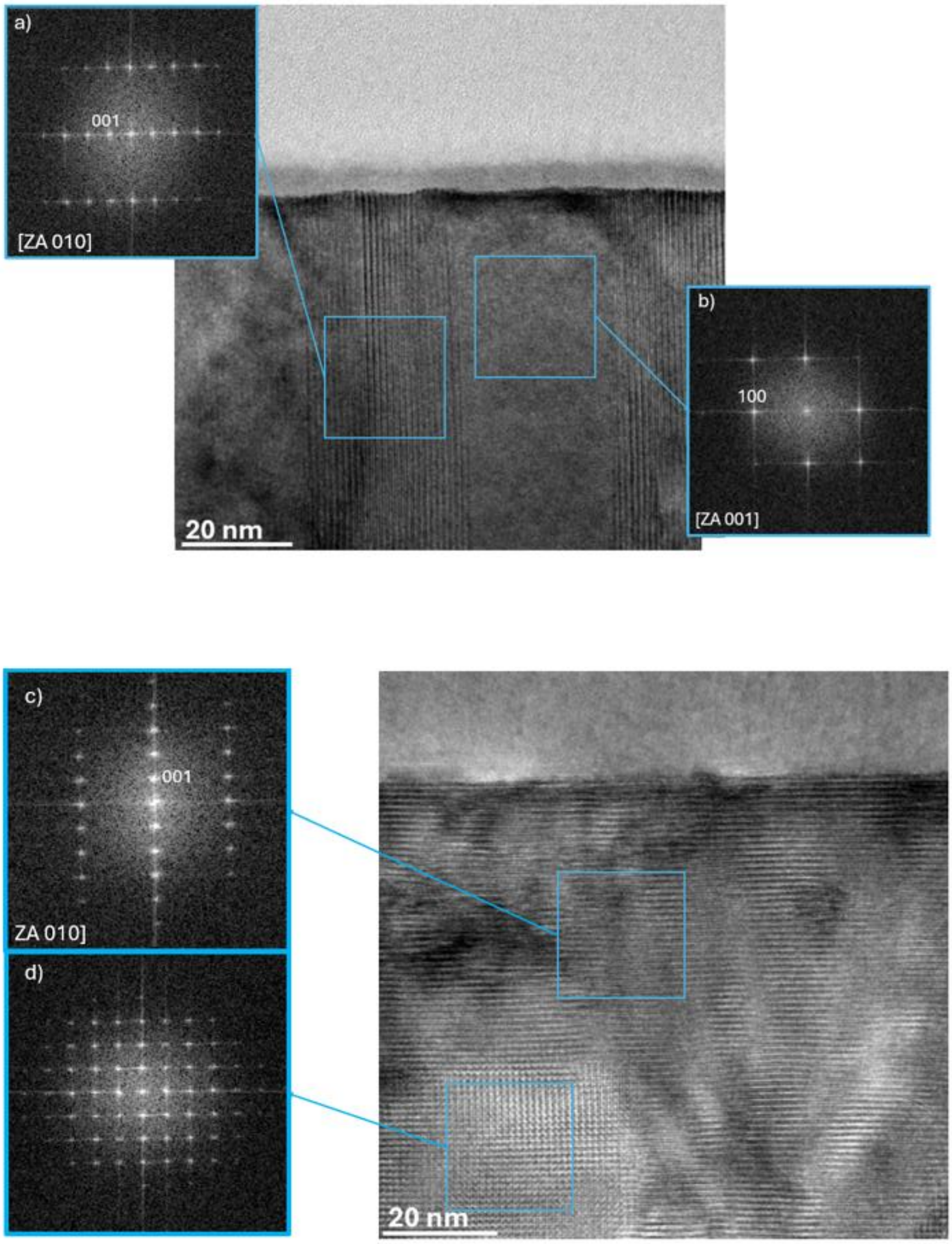

Figure 3.11 Fourier transform (FFT) analysis of different regions of the film:
(a) FFT of a film area from the TEM image at 20 nm (top), with zone axis [010];
(b) FFT of another region of the same film in the TEM image, with zone axis [001];
(c) FFT corresponding to a different area of the film, extracted from another TEM image at high magnification (bottom), showing a different film orientation while maintaining the same zone axis as (a) [010];
(d) FFT highlighting the superposition of two distinct atomic plane configurations within the film, indicative of local variations in crystallographic orientation.

3.12.2 Smp$_{\_LE}$

In the Smp$_{\_LE}$ sample, the film's non-planar morphology, already observed at low magnifications in the SEM (Fig. 3.7, paragraph 3.12), is also evident during the lamella fabrication (Fig. 3.12), which is indeed characterized by steps and surface irregularities attributable to excessive exfoliation from prolonged HF treatment (over 12 hours). Cross-sectional analysis reveals that, overall the film grew epitaxially on the STO substrate and its surface follows the non-planar substrate profile. Overall, the analysis indicates a continuous film with surface inhomogeneities that could affect electrical transport properties and superconductivity quality, particularly regarding pinning centre formation and oxygen diffusion.

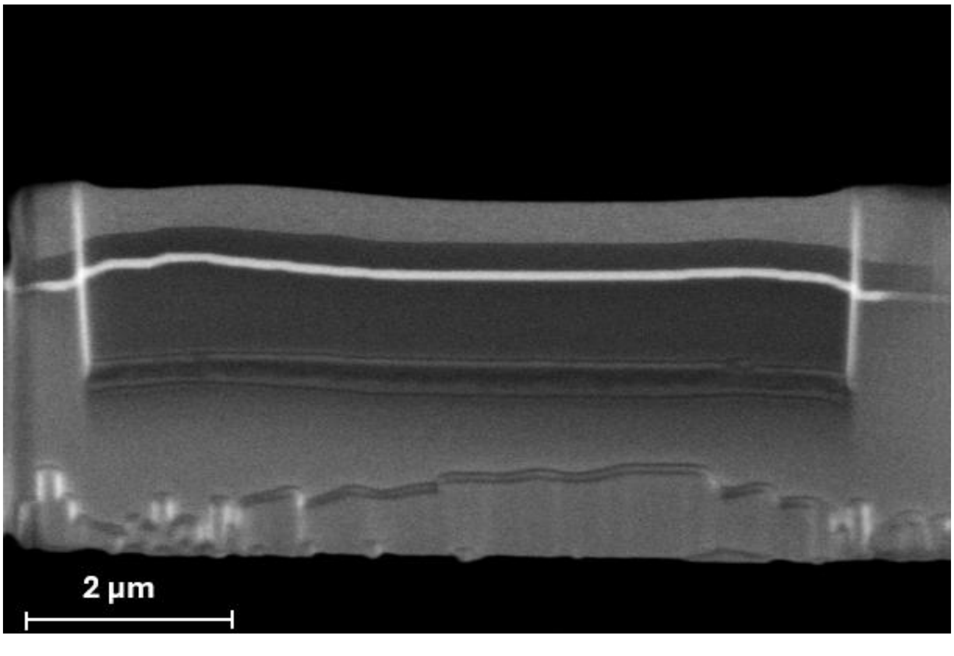

Figure 3.12 Final thinned lamella, where a pronounced wavy morphology is visible throughout the cross-section..

TEM observation of the lamella shows a film thickness of ≈160 nm. At low magnification, substrate alteration and its influence on film growth are clearly visible. The surface is not perfectly planar but exhibits terraces, visible in Fig. 3.13a (blue arrows) spaced between ~1 and 2 μm.

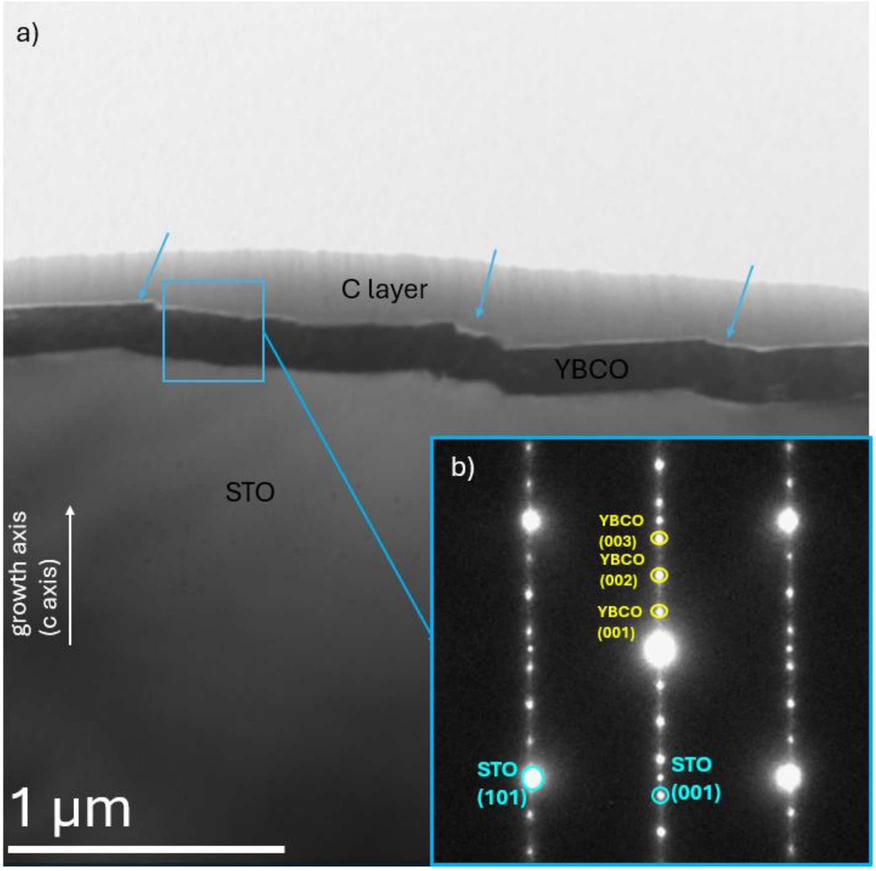

Figure 3.13 (a) TEM image at low magnification of the Smp$_{LE}$ sample, showing the surface steps previously identified by FIB analysis. (b) Inset: SAED pattern acquired from the region highlighted by the blue box, where diffraction spots from both the substrate and the YBCO film are visible.

Nonetheless, the diffraction pattern at the interface (Fig. 3.13b, inset) shows spots attributable to both STO and YBCO, confirming epitaxial film growth.

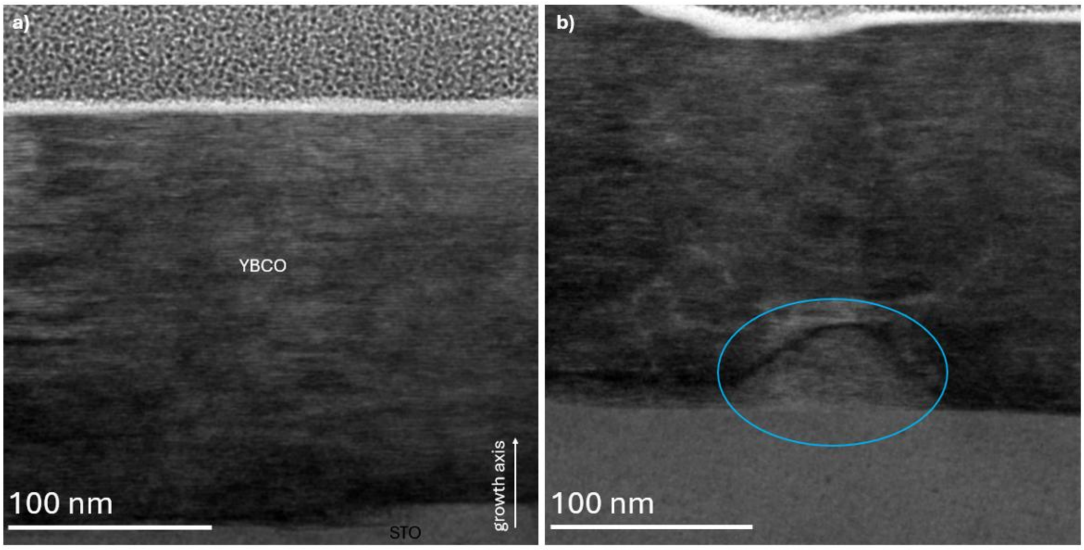

Figure 3.14 (a) TEM image of the YBCO film grown on STO, showing a flat surface without depressions or detectable defects. (b) TEM image of another region of the YBCO/STO interface, where a grain is visible at the film–substrate boundary, as highlighted by the blue circle.

In Figs. 3.14a–b the film appears free of obvious surface grains, in agreement with the low particle density detected by FIB, although some grain at the interface has been identified (Fig. 3.14b, blue circle). The contrast variations with a predominantly horizontal orientation are due to the crystalline matrix composed of superimposed domains. These domains exhibit a relative shift along the growth direction, attributable to the presence of antifaces boundaries (APB)**.**

APBs are stacking discontinuities of the crystal lattice in which one portion of the lattice is displaced with respect to the adjacent portion. In YBCO these defects appear as domains characterized by an atomic displacement that interrupts the continuity of crystal planes along the ab directions [63, 64]. Their formation can be associated with the presence of substrate step edges, stacking faults occurring during growth, or local misalignments at the film/substrate interface, which can nucleate APBs extending through the film thickness.

Functionally, such defects can interrupt the continuity of the CuO_2 planes, acting as scattering centers and causing, in cases of high density, a partial reduction of T_c and alterations in transport behaviour. However, several studies have shown that APBs can also serve as effective vortex-pinning centers, contributing to an increase in J_c and introducing directional anisotropies [65].

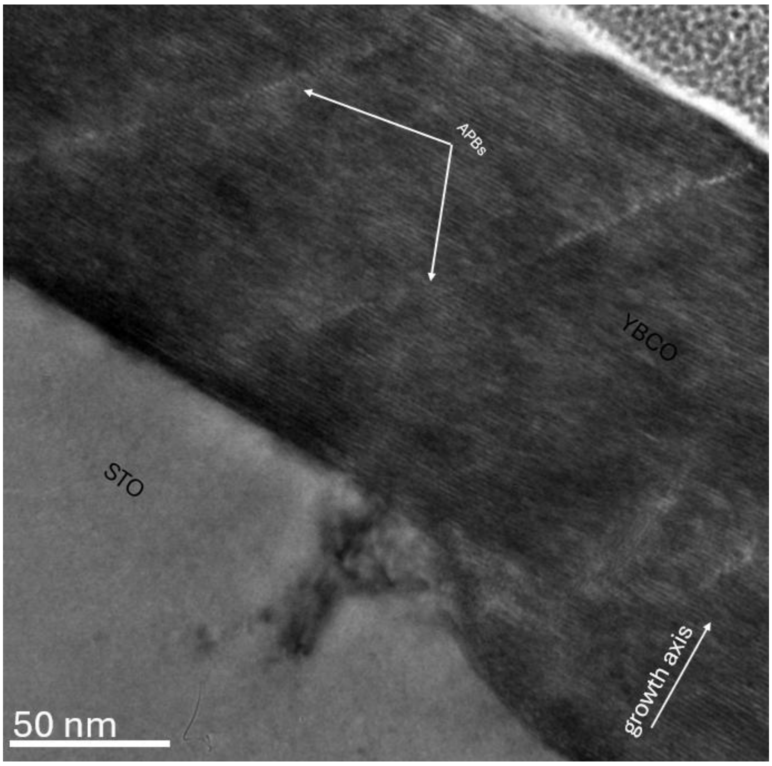

Figure 3.15 TEM image at high magnification of the YBCO film grown on an STO substrate. Anti-phase boundaries are visible within the film, as indicated by the white arrows.

As shown in Fig. 3.15, the presence of this class of defects, which converge into a single region and align along one direction, are shown in Fig. 3.15 and indicated by the white arrows.

3.12.3 Smp$_{\_SE}$

In Fig.3.16 a cross-sectional SEM observation of **Smp$_{\_SE}$** sample. At the bottom is the STO substrate, recognizable by light gray contrast. The YBCO film is visible at the interface, appearing as a continuous bright line with small rounded dark spots with irregular margins randomly distributed these spots correspond to the grains observable on the sample surface (Fig. 3.16b).

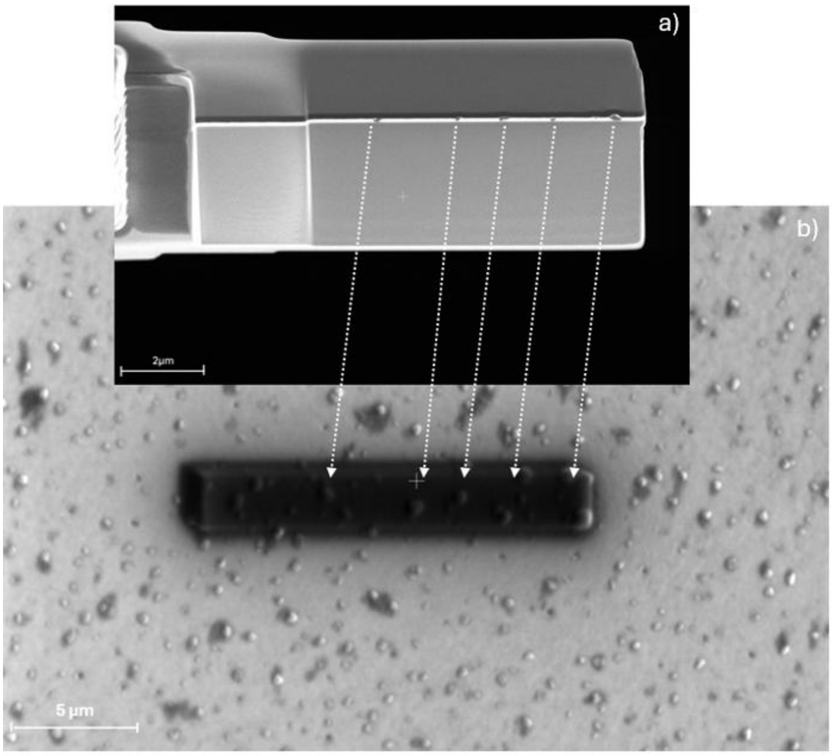

Figure 3.16 (a) SEM image of the FIB-prepared lamella from the Smp$_{\_SE}$ sample, showing dark spots distributed along the YBCO film. (b) SEM image at different magnification of the surface of the same sample, where surface particles are visible. These particles are correlated with the dark spots observed within the film in the lamella.

Finally, two carbon layers are distinguishable: the thin dark electron-beam-deposited carbon layer on the YBCO film surface, and the thicker carbon layer ion-beam-deposited both applied during FIB lamella preparation.

TEM analysis of the lamella (Fig. 3.17) at low magnification shows a homogeneous film on the STO surface, except for two grains (circled in blue) with contrast different from the surrounding film. These grains are the particles observed in FIB (Fig. 3.7c and 3.16a).

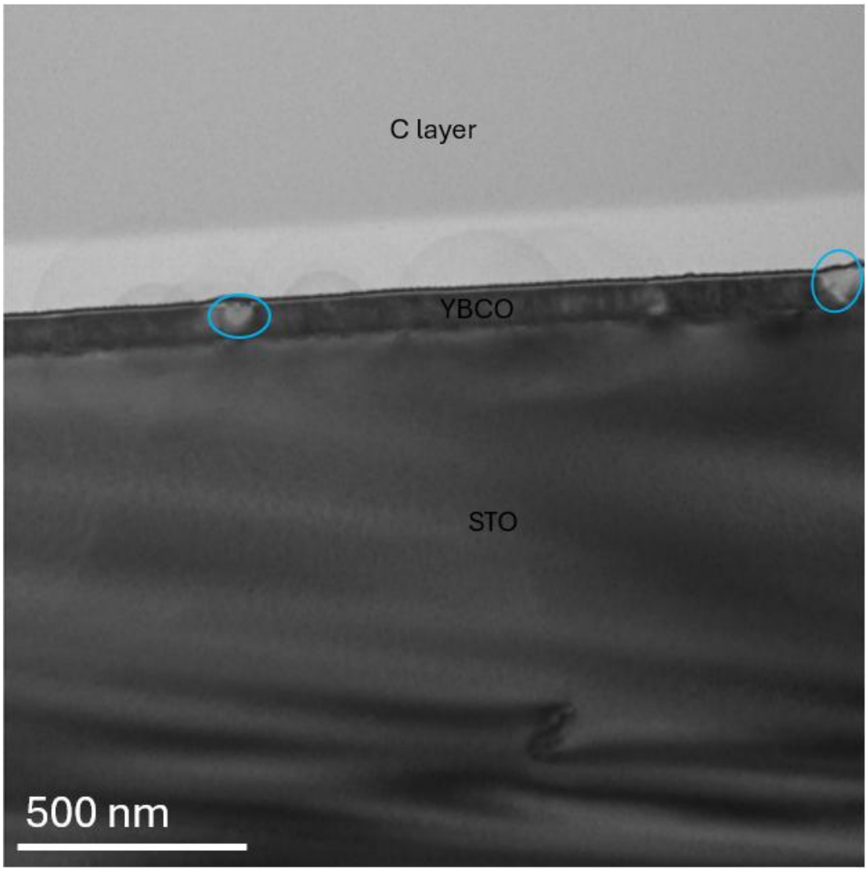

Figure 3.17 TEM image at low magnification showing the STO substrate, the YBCO film, and the protective C layer. Grains located within the film are highlighted by the blue circles.

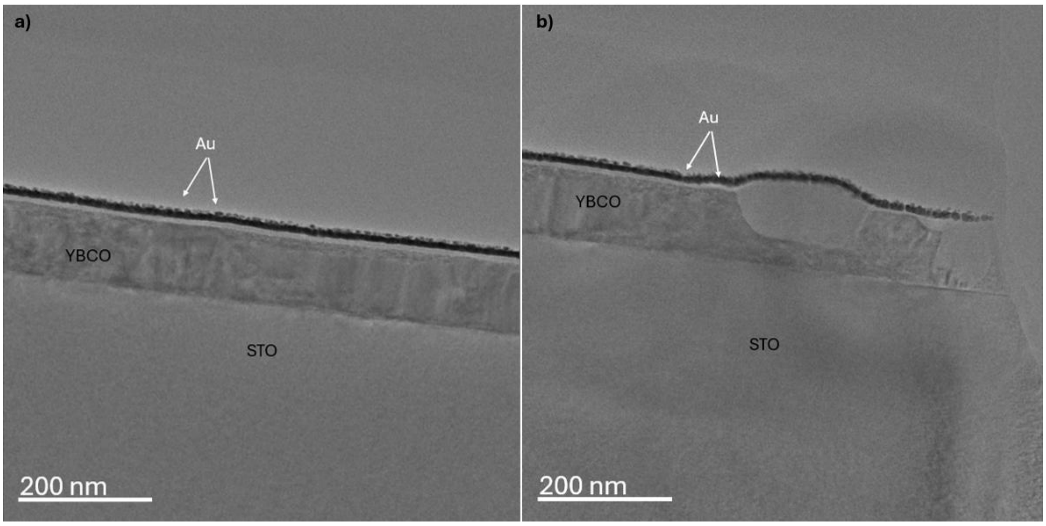

Figure 3.18 (a) TEM image of the YBCO film grown on STO, where a thin Au layer—deposited during the FIB preparation—is also visible on the film surface. (b) TEM image showing the end region of the lamella, where a grain is observed on the surface of the YBCO film.

The STO/YBCO interface appears well defined (Fig. 3.18a). The overall thickness is uniform, with weak periodic vertical contrasts due to strain generated at the YBCO/STO interface. The thin dark stripe above the film corresponds to the sputtered gold layer which was necessary to ensure electrical conduction and reduce charge accumulation during TEM lamella fabrication. In Fig. 3.18b, a surface irregularity associated with the previously identified grain is visible.

At higher magnifications (Fig. 3.19), the film predominantly shows the c-axis parallel to the growth direction, as confirmed by FFT (inset b). However, along the lamella, overlapping of zones with two different orientations are observed, similar to $\mathrm{Smp}_{\_\mathrm{NE}}$, as evidenced by the FFTs in the insets a.

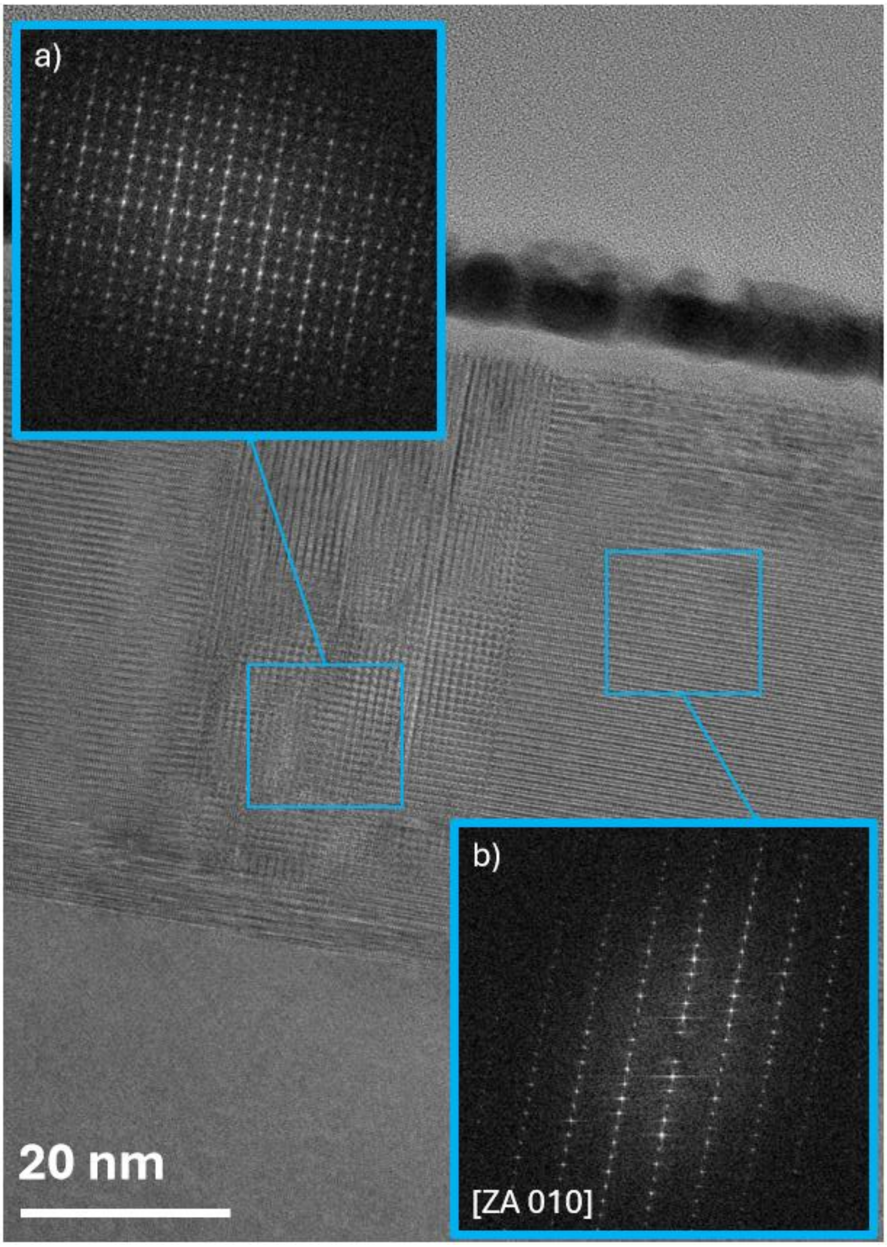

Figure 3.19 TEM image of the YBCO film, showing different atomic plane orientations within the film. (a, inset) Region where orientations intersect. (b, inset) FFT of the selected area, showing the c-axis perpendicular to the growth direction.

On this last type of samples ($Smp_{\_SE}$), which proved to be the most promising, we carried out more in-depth analyses. On Fig.3.20 the SEM cross-section and the TEM of an entire lamella show the presence of grains on the film surface, as observed previously; some grains are nearly indistinguishable from the surrounding film due to minimal contrast variation this because the orientations of these grains are not random, but follow preferential orientations. Indeed, detailed analysis of the grain indicated by the yellow arrow in Fig. 3.20b (shown in Fig. 3.21) reveals it is rotated 90° relative to the surrounding film and aligned with the c-axis along the interface.

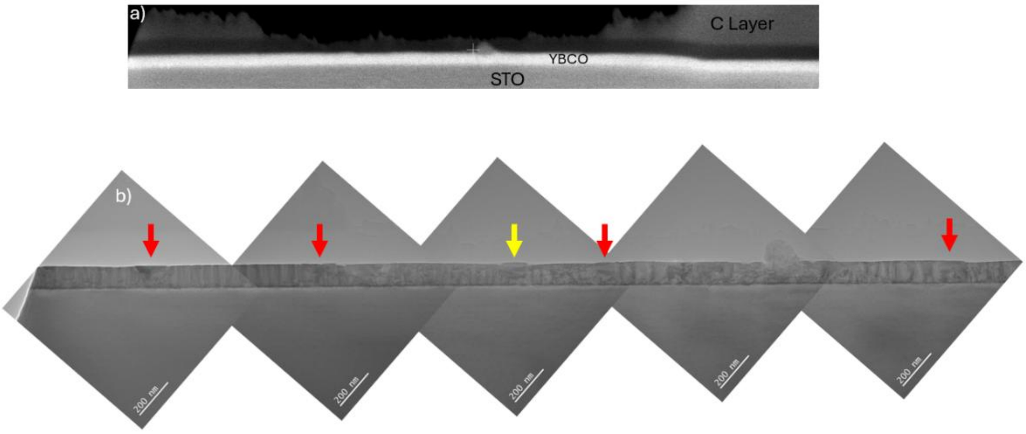

Figure 3.20 (a) SEM excerpt of the FIB-prepared lamella from the Smp_SE sample. (b) Reconstruction of the same lamella with the superposition of the corresponding TEM images. Arrows indicate the different grains observed on the film surface.

The grain size is approximately 76 nm in the shown direction, over a total film thickness of ≈100 nm. The boundary between the film and the grain appears sharp. Finally, focusing on the film, all contrast variations observed in the images are attributable to intrinsic film defects. These defects are predominantly located at the film–substrate interface and along the free surface, preferentially extending along lattice planes and consistent with stacking faults, possibly accompanied by local twins or accommodation dislocations, which disrupt layer regularity without introducing significant compositional differences.

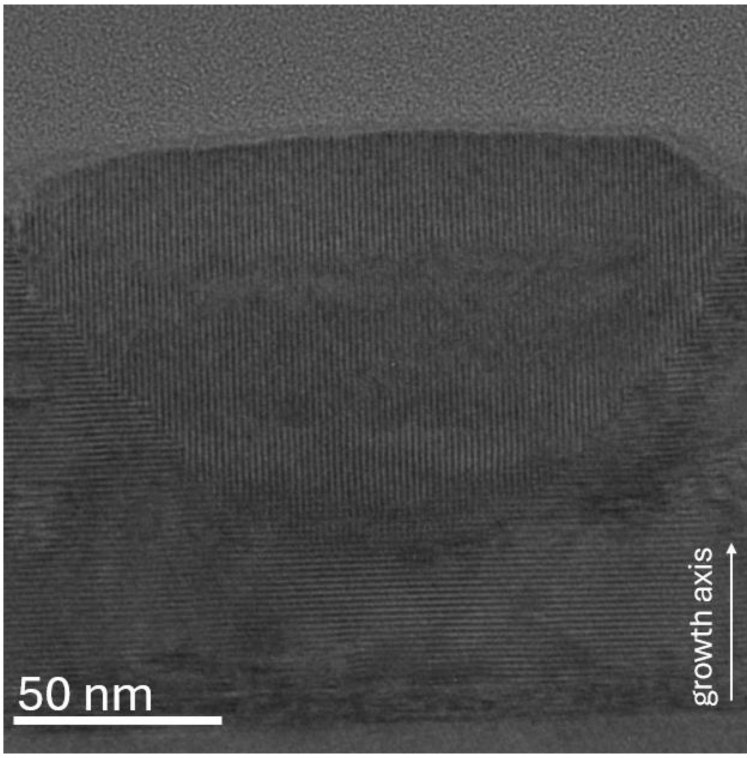

Figure 3.21 TEM image at high magnification of the YBCO film, showing a surface grain rotated by 90° relative to the surrounding film.

Overall, the three samples grown on STO substrates subjected to different treatments show a different evolution in growth quality: Smp$_{\_NE}$ exhibits more disordered, non-perfectly epitaxial growth with high grain density and multiple orientations, likely related to a mixed SrO/TiO_2 surface termination promoting nucleation at different sites; Smp$_{\_LE}$ shows a continuous film but with terraces and surface irregularities (steps) due to prolonged substrate etching, though growth remains epitaxial following the non-planar STO profile; Smp$_{\_SE}$ is the sample with the best quality, this because the etching process, compared to the non-etched sample, contributed to the removal of the mixed SrO_2 /TiO_2 termination present in the initial specimen. The etching duration was not long enough to affect the integrity of the substrate. In all samples, rotated grains relative to the main growth direction, but with different morphology, indicating that substrate terminations and surface roughness play a crucial role in determining nucleation sites and local crystallographic orientations. These results highlight the importance of controlling substrate preparation conditions to optimize film structural quality and, consequently, its transport and superconducting properties. A more detailed film characterization has been performed via STEM analysis and will be presented in the following sections.

The data discussed here were obtained using Focused Ion Beam (FIB) preparation systems, specifically the ***Helios 5 UC from Thermo Fisher*** at ***CNR-IMM in Catania*** and the ***Helios Nanolab 600***i from ***Thermo Fisher***

Scientific at CNRS-CEMES in Toulouse. TEM analyses were conducted using the ***JEOL 2010F*** transmission electron microscope at the ***CNR-IMM (HQ)*** laboratories in ***Catania***.

3.13 STEM Analysis

Among the different film growths that were investigated samples Smp$_{\_SE}$, proved to be the most promising, we carried out more in-depth analyses including atomic-scale investigation. STEM analysis was therefore employed to examine the interfacial structure and defects in more detail.

Attention was devoted to identifying and characterizing structural defects such as antiphase boundaries, stacking faults, and misoriented grains, with the aim of correlating these microstructural features with the observed electrical and superconducting properties. The following sections present the main findings from this detailed characterization.

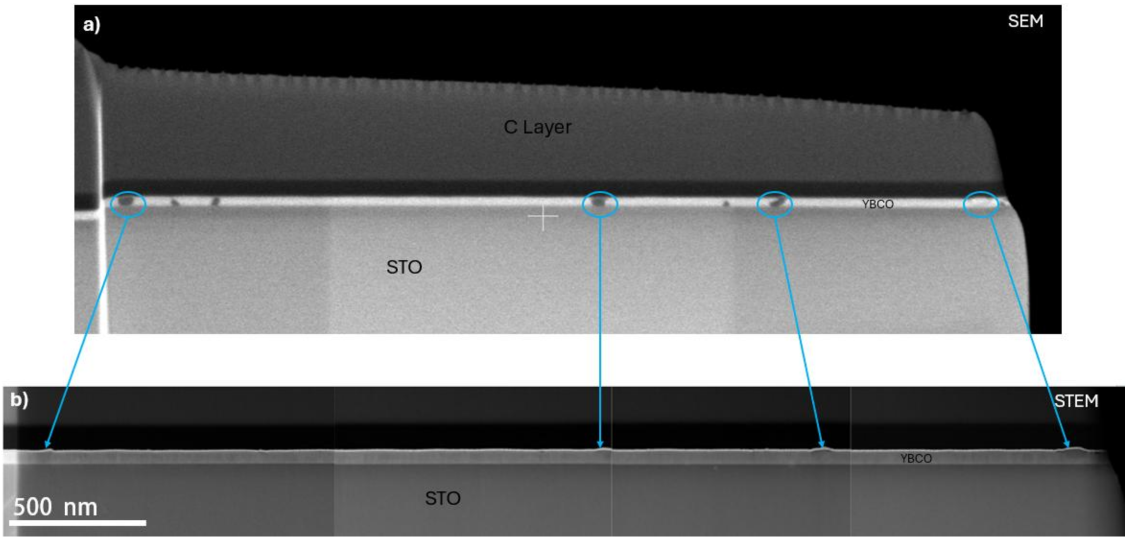

Figure 3.22 (a) SEM image of the YBCO lamella deposited on STO, showing darker grains distributed along the film.
(b) Reconstruction of the same lamella from STEM Z-contrast dark-field images, highlighting the arrangement and morphology of the grains observed in SEM.

The cross-sectional SEM micrograph (Fig. 3.22a) highlights the STO substrate at the bottom and the YBCO film as a bright, continuous line immediately above the interface. Along this line, small regular agglomerates can be observed, corresponding to the protrusions previously described. At the top of the lamella, a darker-contrast region and a thin surface film are present; these are the protective carbon layers deposited during FIB lamella preparation.

The grains identified in the SEM micrograph are consistent with the protrusions observed along the lamella reconstructed by overlaying low-magnification STEM dark-field and Z-contrast images (Fig. 3.22b), as indicated by the light-blue arrows.

The magnified STEM z-contrast view of a portion of the lamella highlights the overall morphology of the YBCO film on the STO substrate in a region where one of the previously mentioned grains is present (Fig. 3.23b).

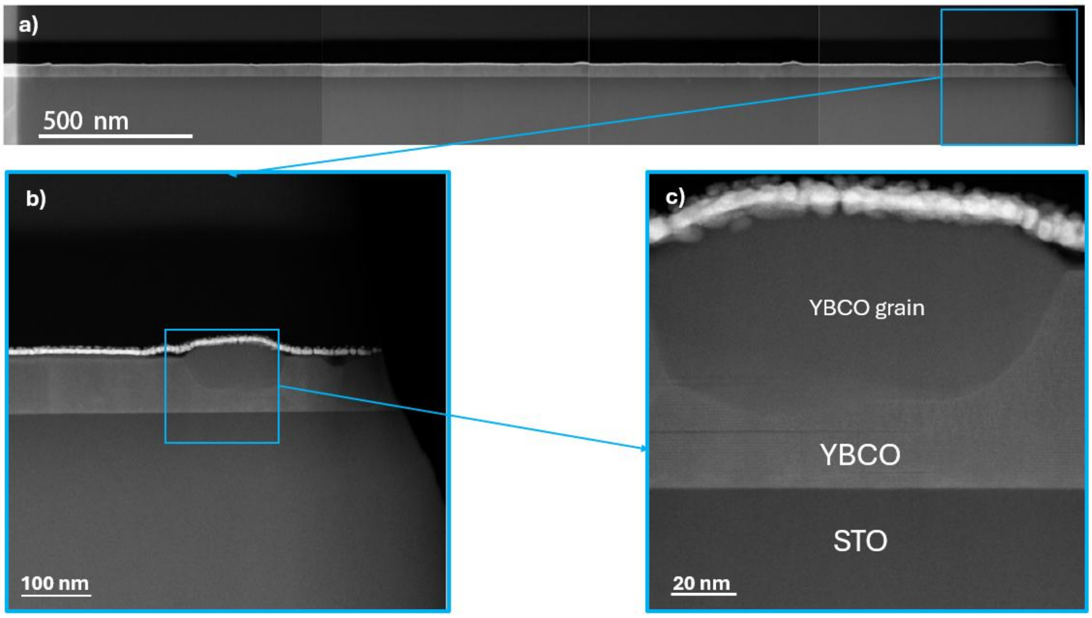

Figure 3.23 (a) Reconstruction of the YBCO lamella from STEM Z-contrast dark-field images; the blue box highlights the terminal region of the lamella.
(b) Enlargement of the blue box in (a), showing a prominent surface grain.
(c) Further enlargement of the grain highlighted in (b), revealing finer morphological details.

Fig. 3.23c shows the clearly the STO substrate and the YBCO film, on the top of the YBCO film the Au layer deposited by sputtering during FIB lamella Preparation, and the presence of an isolated grain within the film. This grain exhibits a well-defined grain boundary and a rounded shape.

Examining the bottom-left portion of this grain, the high-resolution image (Fig. 3.24a) reveals the presence of three grain boundaries within the selected region, highlighted by the white dashed lines. The three identified areas exhibit distinct crystallographic orientations.

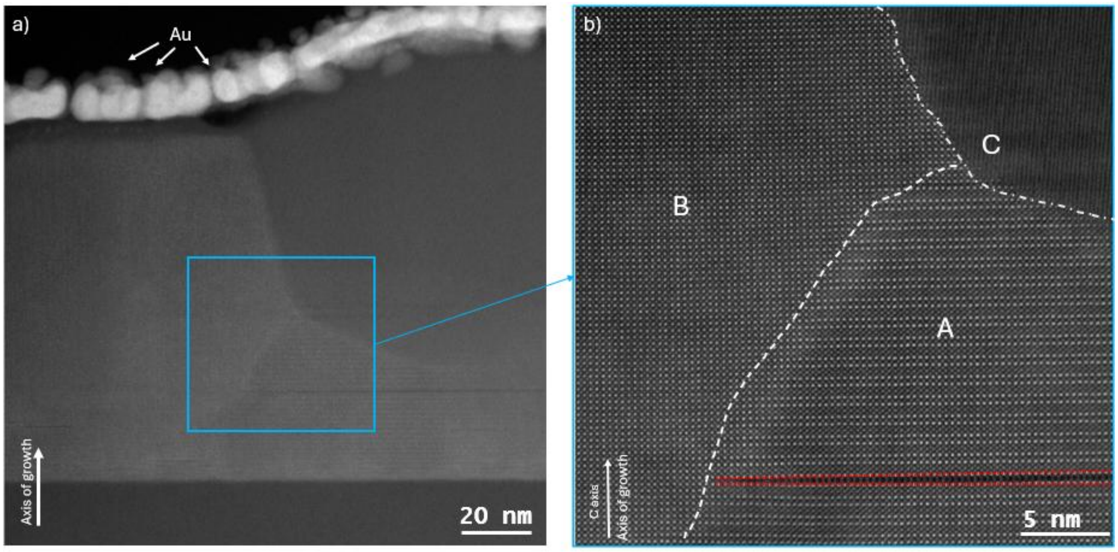

Figure 3.24 (a) Enlargement of the YBCO film surface where the grain was identified; a thin sputtered Au layer is visible.
(b) Enlargement of the box in (a), showing the coexistence of three distinct grains.

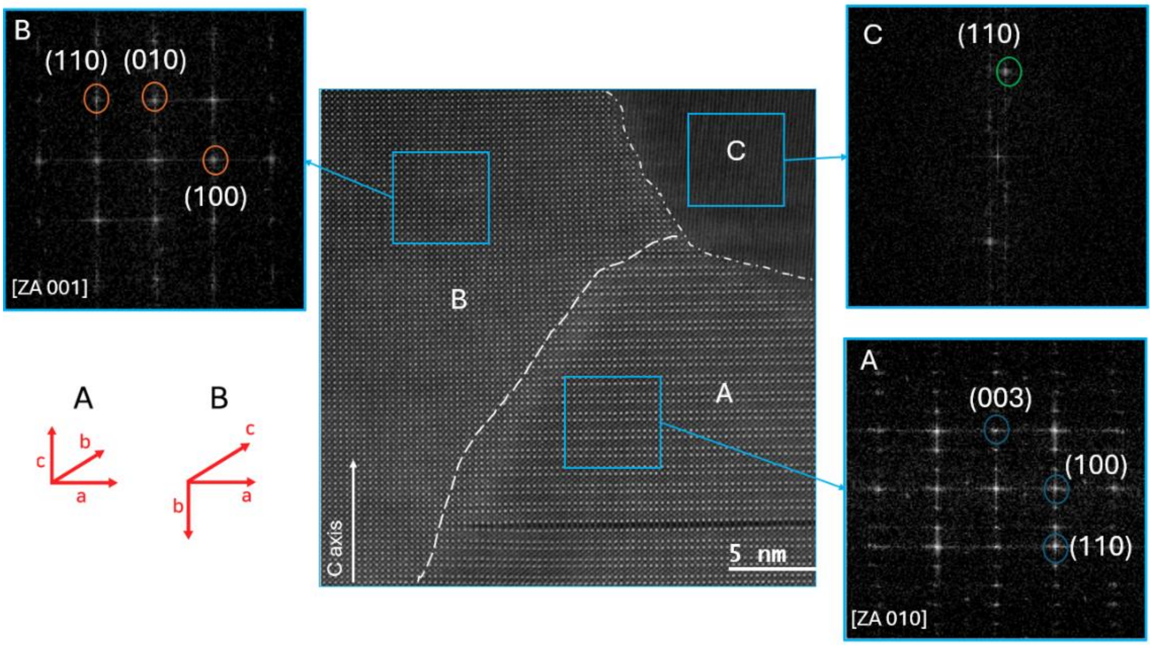

Figure 3.25 Central image: STEM Z-contrast dark-field at 5 nm of the three adjacent grains. Two distinct grain boundaries are identified. Inset B (top) shows the FFT of grain B, inset C (top right) shows the FFT of grain C, and inset A (bottom right) shows the FFT of grain A.

The analysis performed using FFT provided information on the local crystal structure of each grain.

In **grain A**, the zone axis was identified as [010], with well-defined reflections corresponding to the (100), (103), and (003) planes, consistent with the orthorhombic structure of YBCO.

Grain B, is oriented along [001] direction, characterized by the (100), (010), and (110) reflections. This indicates a 90° rotation of the lattice with respect to region A.

As for **grain C**, it was not possible to tilt the grain into a specific zone axis: only two main high-intensity diffraction spots are clearly resolved, which can be indexed as the (110) reflection of YBCO.

The information obtained also makes it possible to identify, in the case of the grain labeled A, the defect highlighted by the two red lines in Fig. 3.25b as an intercalation of YBCO 124 in the YBCO 123 matrix. The so-called YBCO 124 intergrowths (planar defects of $YBa_2Cu_4O_8$) are among the most common extended defects in YBCO films. Structurally, these intergrowths consist of an additional Cu–O chain layer inserted into the YBCO 123 lattice structure, locally generating a Y124-type stacking sequence.

Since YBCO 124 exhibits a lower T_c (~80–85 K) compared to YBCO 123 (~92–93 K), regions containing 124 intergrowths can locally reduce T_c, causing a broadening of the resistive transition in thick films. From the perspective of vortex pinning, the strain fields induced by Y124 defects act as strong pinning centers, enhancing the in-field J_c, when a moderate density of 124 intergrowths is present [66].

The structure of Y124 may be described as comprised of blocks related to the Y123 matrix, with an additional Cu–O chain layer relative to Y123 and a modified stacking sequence along the b direction [67].

Finally, examining the STO/YBCO interface, a slight "step" can be observed between the substrate and the film (Fig. 3.26a). This phenomenon had already been reported in the TEM analysis of sample $\mathrm{Smp}_{\_\mathrm{LE}}$ (Section 3.12.2), although in that case it referred to macroscopic steps associated with surface irregularities induced by prolonged etching, whereas here it corresponds to the absence of a single atomic plane. This type of interfacial defect can be attributed to local fluctuations in the surface termination of the STO substrate or to slight non-uniformities in the morphology of the atomic terraces present on the surface prior to deposition.

In this context, it is important to highlight that the pre-deposition etching step was specifically implemented to homogenize the surface termination of the STO substrate and minimize precisely this type of interfacial defect. The ability to detect these atomic-scale defects using high-resolution STEM demonstrates the effectiveness of the characterization technique employed.

Moreover, the low frequency of such atomic steps observed in sample Smp$_{\_SE}$ provides experimental validation of the effectiveness of the adopted surface-treatment procedure, confirming that the optimized etching protocol used for this sample successfully produced a more uniform and well-controlled substrate termination.

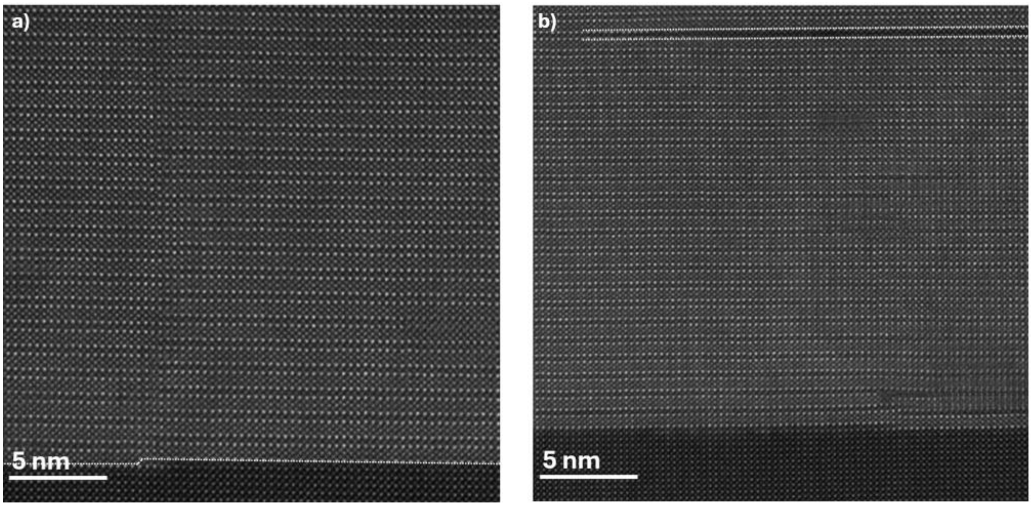

Figure 3.26 (a) STEM at 5 nm of the STO/YBCO interface, clearly showing the atomic planes of both materials.
(b) STEM at 5 nm of the STO/YBCO interface, highlighting the presence of defects within the film.

As shown in Fig. 3.26, this atomic step at the interface generates an APB that propagates into the overlying film. The APB originates from the misalignment of a single atomic plane at the STO/YBCO interface and manifests as a discontinuity in the stacking sequence of the crystallographic planes. This type of planar defect, clearly visible in the Z-contrast STEM image, introduces a local translation of the crystal structure that disrupts the phase periodicity with respect to the surrounding matrix. APBs can influence the transport properties of the film by acting as barriers to current flow and locally modifying the superconducting characteristics.

Overall, the STEM analyses confirm that the film grew epitaxially on the STO substrate during deposition. This behaviour is enabled by the good lattice matching between STO and YBCO: the cubic lattice parameter of $SrTiO_3$ is approximately 3.905 Å, while the in-plane lattice constants of YBCO, a and b, are about 3.82 Å and 3.88 Å, respectively. The resulting lattice mismatch, slightly above 1%, is sufficiently low to allow high-quality epitaxial growth without the formation of structural discontinuities or delamination at the interface.

However, as shown in Fig. 3.26b, Y124 inclusions are present.

The analyses were carried out using a sub-ångström ***ARM200F (JEOL)*** microscope at the ***CNR-IMM laboratories in Catania.***

3.14 Irradiation of YBCO superconducting films

Among the available samples, the YBCO film on an STO substrate, labelled Smp$_{\_SE}$ and previously subjected to a lithographic process (Paragraph 3.10), was selected for irradiation.

The irradiation of the sample was carried out under vacuum, using an ion beam perpendicular to the sample surface and keeping the sample at room temperature throughout the process. The sample was bombarded with heavy lead (Pb) ions at an energy of 1.2 GeV, and a fluence corresponding to a matching field of 3 T. This type of irradiation induces the formation of columnar defects, whose specific size and distribution make them particularly effective at capturing Abrikosov vortices, characteristic of HTS materials. The expected effect of this process is an increase in the critical current in the presence of a magnetic field, resulting in improved transport performance under operating conditions. However, the introduction of structural disorder due to irradiation-induced defects may also have undesirable effects: T_c tends to decrease, and the superconducting transition broadens, indicating a less homogeneous superconducting behaviour.

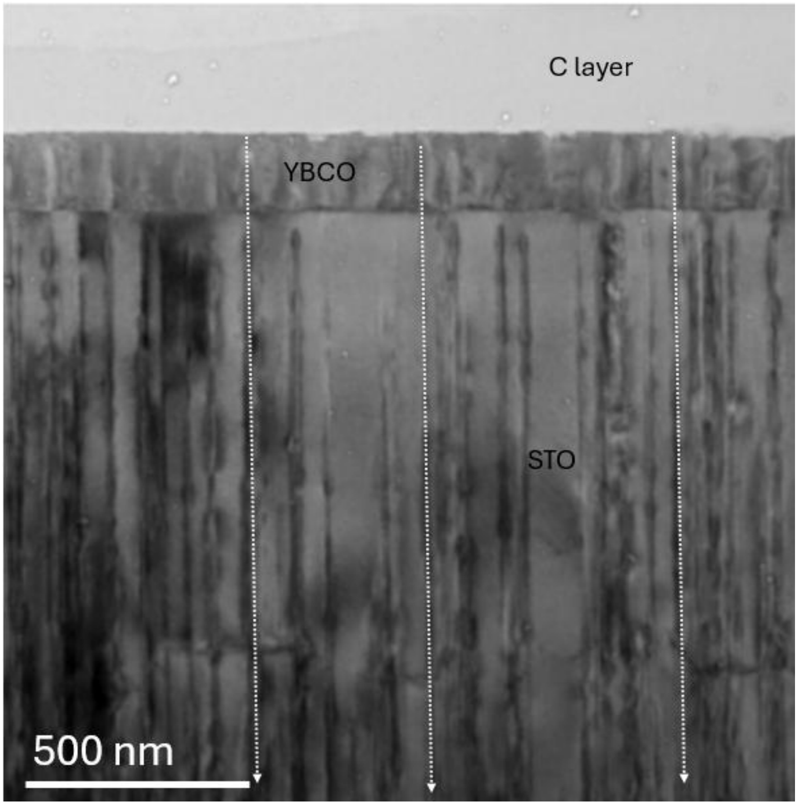

Figure 3.27 TEM image of the irradiated Smp_SE YBCO film. Ion tracks penetrating the film are clearly visible as columnar tunnels, illustrating the path of individual high-energy ions through the material.

As highlighted in Fig. 3.27 (white arrows), the interaction of the ions with the sample is clearly visible both within the superconducting film and in the substrate, producing tracks that traverse the entire thickness and act as artificial pinning centres. In the analysed area an average density of 2.68×10^{10} tracks$\cdot$cm^{-2} was measured. This number is consistent with the nominal fluence ($\Phi = 1.45\times10^{11}$ ions$\cdot$cm^{-2}).

A more detailed analysis of the sample microstructure, as shown in Fig. 3.28, reveals that the interaction between the incoming ions and the material varies depending on the region considered. On the surface of YBCO, tunnels of significantly larger size are observed compared to those in the STO substrate, with widths ranging from 5.08 to 12.43 nm for YBCO and from 2 to 4.59 nm for STO.

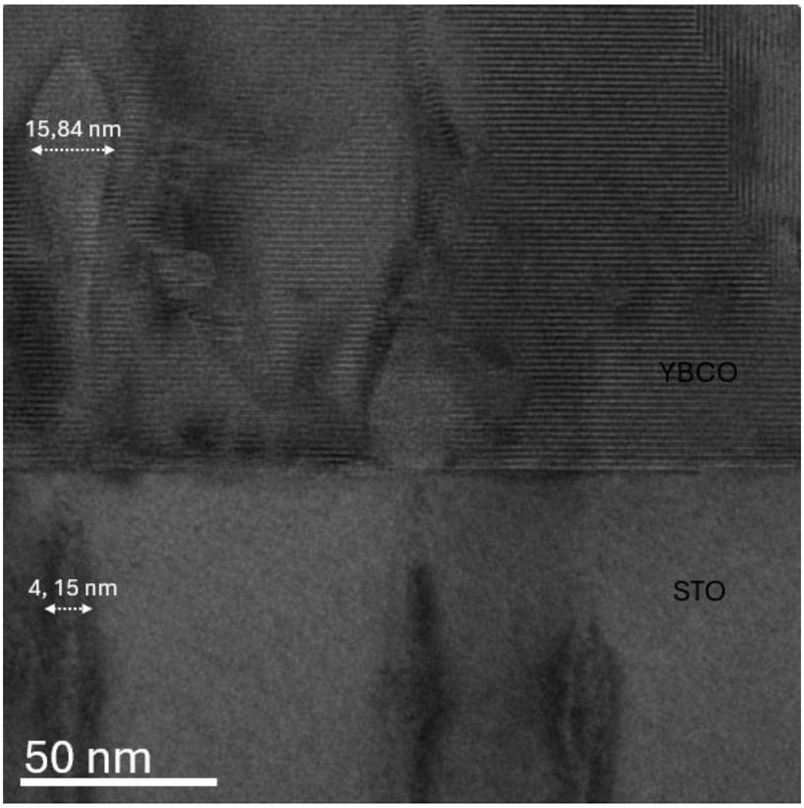

Figure 3.28 TEM image of the YBCO/STO interface, showing ion-induced channels of varying dimensions created by Pb ion irradiation. The contrast highlights the morphology and size distribution of the defect tracks at the film–substrate boundary.

STO and YBCO respond differently to ion bombardment due to a combination of factors: differences in composition and crystal structure, differing balances between electronic and nuclear stopping, different threshold energies for atomic displacement, and thermal dissipation effects. These aspects explain why the ion tracks and resulting defects have different sizes and visibility in the two materials [68, 69].

It should also be noted that ion tracks are not always visible, due to the lamella thickness and the tracks' position relative to the observation plane.

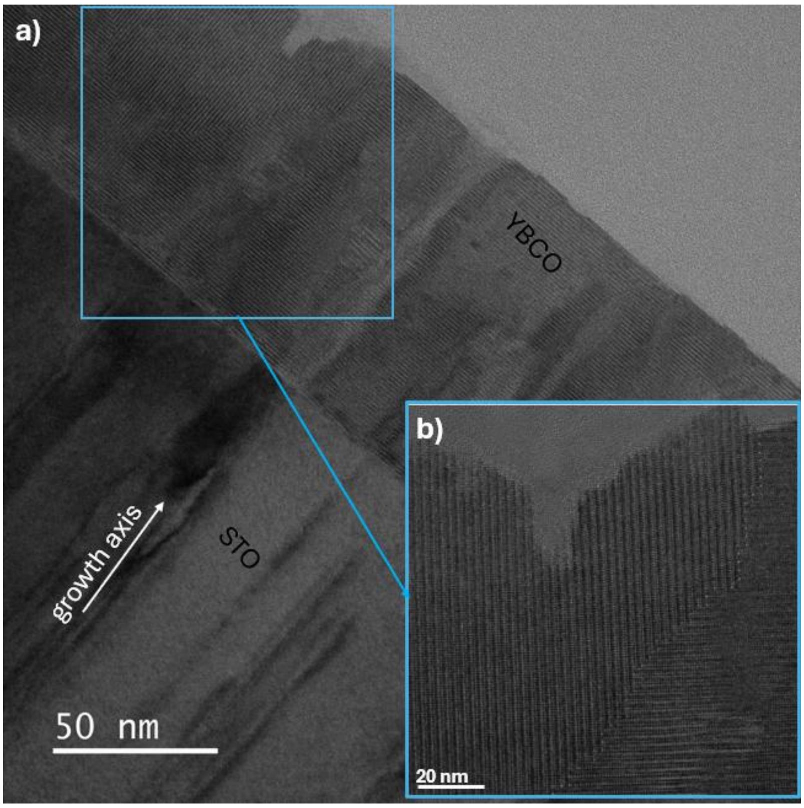

Figure 3.29 TEM micrograph (bright-field) of the YBCO/STO interface post-irradiation. Irradiation-induced channels are visible (arrows). Inset b —detail showing a grain rotated relative to the matrix.

It is also observed that the morphology of the ion track depends on the crystallographic orientation of the grains. As shown in Fig. 3.29a, irradiation produces different effects depending on whether the ion interacts with grains oriented parallel or perpendicular to the growth axis; as highlighted in the inset of Fig. 3.29b, in the presence of grains with orientation parallel to the growth axis, a predominantly amorphization phenomenon is observed on the grain surface.

The extent of amorphization is also correlated with the lamella thickness, as shown in Figs. 3.30a and 3.30b: when the diameter of the amorphous column is comparable to the lamella thickness, as indicated in the schematic in Fig. 3.30c, the region traversed by the ion becomes completely amorphous.

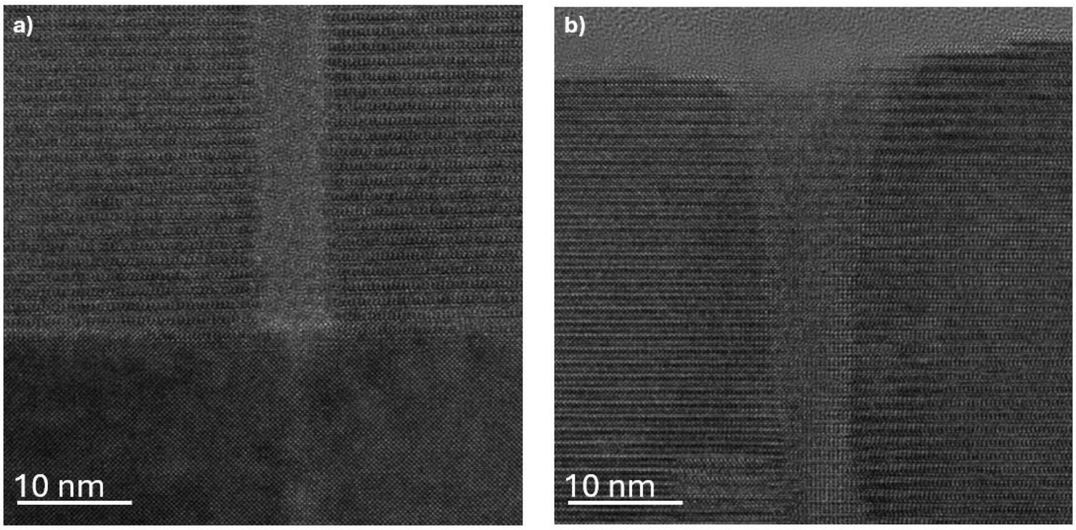

Figure 3.30 (a) TEM micrograph showing the Pb-ion track within the YBCO film. (b) TEM micrograph displaying another ion-induced track in the YBCO film, where clear amorphization around the tunnel is observed.
(c) Schematic illustration of the formation of a tunnel when the incident ion traverses a particularly thin region of the film, leading to local fracture.
(d) Schematic representation of the same process in a thicker region of the film, where no fracture occurs and amorphization remains confined around the tunnel.

The irradiation was carried out at the ***Politecnico di Torino*** in collaboration with ***INFN Legnaro***, while TEM analyses were performed at ***CNR-IMM in Catania***.

3.15 Discussion: Correlation Between Microstructure and Superconducting Properties

The TEM analysis provides direct evidence for the relationship between substrate surface chemistry, film microstructure, and superconducting behavior. Several key correlations emerge from this study:

1. Surface Termination and Nucleation: The mixed SrO/TiO_2 termination in non-etched substrates leads to multiple nucleation sites, resulting in high grain density and misoriented domains. This microstructural disorder directly causes the broadened superconducting transition and reduced T_c observed in Smp_{NE}.

2. Substrate Roughness Effects: Excessive etching (Smp_{LE}) creates surface terraces and irregularities that, while allowing epitaxial growth, introduce strain fields and defects that slightly degrade superconducting properties. The intermediate approach (Smp_{SE}) balances surface termination control with minimal roughness.

3. Role of Structural Defects: The antiphase boundaries, stacking faults, and misoriented grains observed in all samples act as weak links that can suppress J_c and modify flux pinning behavior. However, in the optimized sample (Smp_{SE}), these defects are minimized, leading to superior superconducting performance.

4. Implications for Applications: These findings indicate that careful substrate preparation is essential for fabricating YBCO films suitable for high-field magnet applications in fusion reactors. The optimized etching protocol established in this work provides a pathway for producing high-quality superconducting films with enhanced radiation tolerance.

4. IRON BASED SUPERCONDUCTING FILM

4.1 Superconducting Materials

FeSeTe is an iron chalcogenide belonging to one of the eight families of Iron-Based Superconductors (IBS), a class of recently discovered superconducting materials that are also part of the HTS category [70].

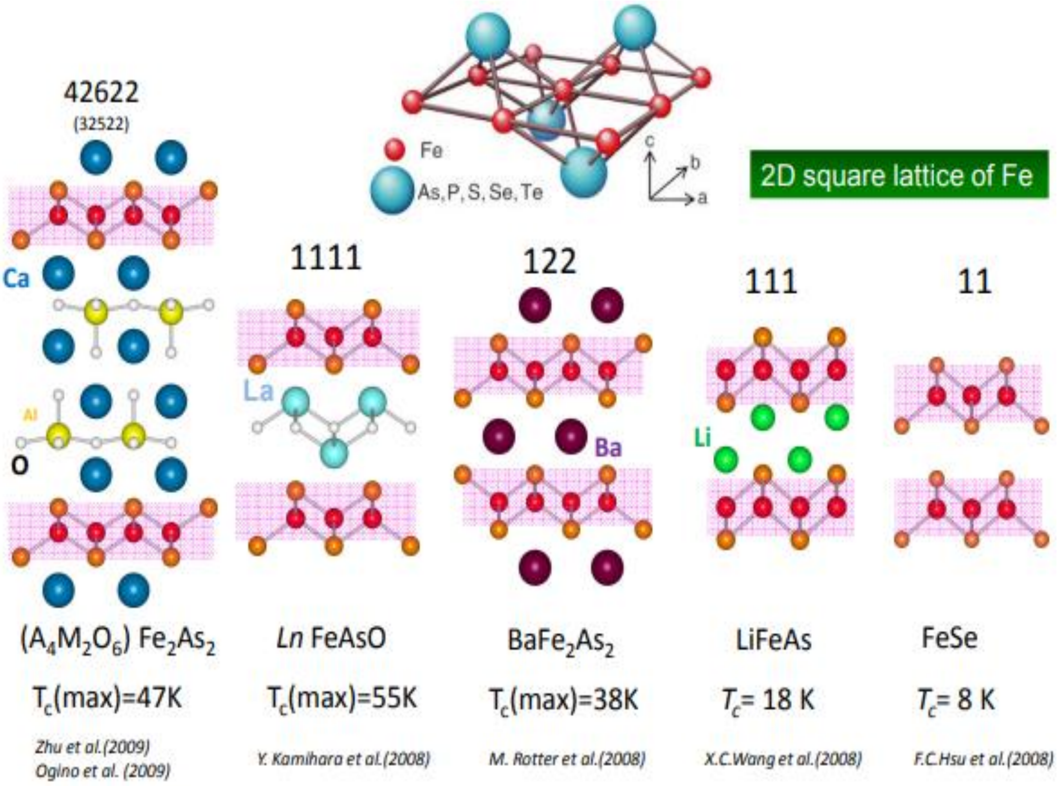

Figure 4.1 Overview of the principal families of iron-based superconductors—42622, 1111, 122, 111, and 11—showing their characteristic layered crystal structures, the Fe square lattice, and the corresponding maximum critical temperatures $T_c$reported in the literatur

The different constituent families, shown in Fig. 4.1, differ in their chemical composition and crystal structure; although many of these contain arsenic, current focus is shifting towards iron-based materials free of this element. This is the case for iron chalcogenides, which are also highly sensitive to stoichiometry, chemical doping, synthesis conditions, and external pressure.

Among the iron chalcogenides, we focus on FeSeTe (or $FeSe_{0.5}Te_{0.5}$), a composition with a 50:50 ratio between selenium (Se) and tellurium (Te).

Pure FeSe has a simple crystal structure, which makes it attractive both for fundamental studies and applications. It exhibits a T_c of approximately 9 K and a very high upper critical field (H_{c2}) of up to 50 T. Interestingly, the partial substitution of Te for Se in FeSe leads to a significant enhancement of superconducting properties, with an increase of T_c up to 75%.

FeSeTe typically exhibits a T_c around 14 K, but under certain conditions or specific treatments, it can reach up to 15 K. T. Taen et al. successfully grew high-quality FeSeTe single crystals, reporting a T_c of ~14 K and a J_c exceeding 1×10^5 A/cm^2 at 5 K in zero field. [71, 72]

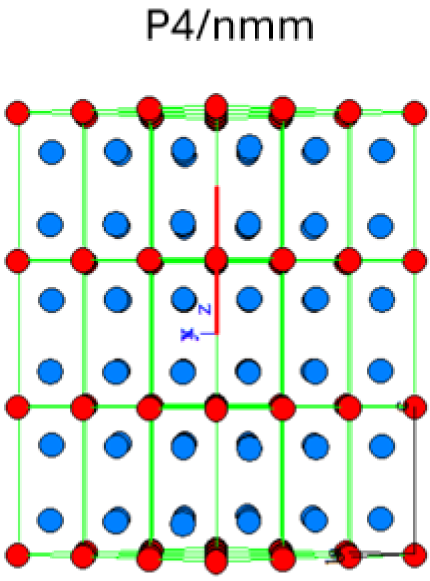

Figure A.8 Phase difference map obtained by off-axis electron holography on a YBCO/STO film. The image shows the phase variation (in radians) between 1 T and 2 T. Ice formation on the sample is clearly visible, particularly in the lower region, affecting the interpretation of the local magnetic response.

An interesting aspect lies in their simple crystal structure, shown in Fig. 4.2; it consists of Fe ions tetrahedrally coordinated by Se and Te, arranged in layers stacked along the c-axis in the tetragonal lattice, without other intercalated cations as found, for example, in pnictides. However, it has recently been recognized that in Fe(Se,Te), Fe ions can also occupy interstitial 2c positions within the anion plane [27].

4.2 Substrates

In the context of thin film growth of iron-based superconductors, such as Fe(Se,Te), YSZ (Yttria-Stabilized Zirconia) is among the most widely used substrates due to its excellent structural and chemical properties. Pure ZrO_2 exhibits a tetragonal phase at room temperature but tends to transform into a monoclinic phase at lower temperatures. The addition of yttrium oxide (Y_2O_3) stabilizes the tetragonal phase, maintaining it at room temperature and providing greater resistance to thermal shock, with a lattice parameter of 3.637 Å.

Although YSZ is primarily known for its high compatibility with oxide superconductors, it has also been widely used for the growth of iron-based superconductors. Its thermal and chemical stability makes it suitable for the high-temperature processes required for the deposition of FeSeTe thin films. The structure of YSZ is shown in Fig. 4.3.

The main limitation of using YSZ for the growth of FeSeTe is the lattice mismatch between the substrate and the film. This mismatch can promote the formation of defects and crystalline disorder, which can degrade the superconducting properties. However, proper optimization of the deposition conditions can mitigate these effects and enable the fabrication of higher-quality films.

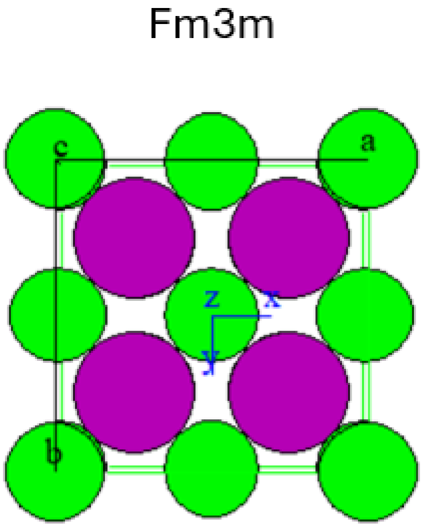

Figure 4.3 YSZ structure

.

The main criteria considered for the selection of YSZ as a substrate are:

1. **A** relatively small lattice mismatch with respect to the typical in-plane parameters of iron-based superconductors, which range between 3.77 and 4.02 Å.
2. The absence of chemical reactions at the interface during growth.

Additionally, YSZ offers further advantages such as mechanical robustness, dielectric stability, and good commercial availability, which strengthen its use in the growth of (001)-oriented epitaxial films of iron-based superconducting materials.

4.3 Auxiliary Materials

Recent studies have shown that the use of Zr-doped cerium oxide (CZO) as a buffer layer can significantly enhance the epitaxial growth of Fe(Se,Te) films on YSZ, by overcoming the crystalline mismatch issue [73].

CZO provides the necessary biaxial texture to promote epitaxial alignment and acts as a barrier against ion diffusion from the underlying substrate, thanks to its excellent lattice compatibility with both the superconducting film and the YSZ crystal structure, as shown in Fig. 4.4.

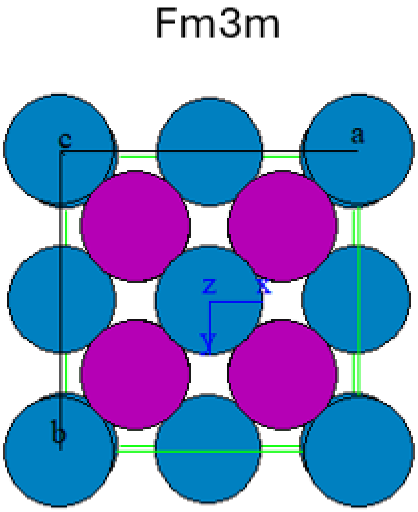

Figure 4.4 CZO structure

Zirconium doping plays a crucial role by stabilizing the oxygen content in CeO_2 and reducing its surface roughness [74].

CZO is grown in ENEA on YSZ single crystals using metal-organic decomposition (MOD) by dissolving stoichiometric amounts of Ce (III) acetate hydrate and 5mol.% Zr (IV) acetylacetonate in propionic acid. Water and excess of solvent are removed by rotary evaporation: a total metal concentration [Ce]+[Zr] = 0.3 M is needed. The solution is then deposited on YSZ single crystal substrate by spin coating and dried for 5 minutes at 120°C in air. Finally, samples are thermally treated in flowing 5% $Ar{-}H_2$ (pyrolysis in air for 30 minutes at 450° C and crystallization for 30 minutes at 950° C in 0.5l/min $Ar - H_2$). The thickness of the obtained samples is around 30 nm [75].

4.4 Fe(Se,Te) seed

It has been observed, as reported in the literature [76], hat the growth of a seed layer between the substrate and the superconducting film improves both the crystal and chemical alignment, and allows a lower deposition temperature of the phase. In the case of the IBS samples studied here, the seed layer consists of a $FeSe_{0.5}Te_{0.5}$ film which exhibits poor superconducting properties compared to the film of interest. However, it possesses a high-quality structure, and the growth of the film on the seed layer can be considered substantially homoepitaxial.

The properties of the phase as a function of the deposition temperature were analysed with the aim of optimizing the seed layer. A preliminary analysis shows that the T_c is highest when the deposition temperature is 300 °C, while it decreases both with lower and higher temperatures. Moreover, it was observed that the out-of-plane orientation is strongly influenced by the deposition temperature: the higher the temperature, the better the orientation.

After several trials, the optimal deposition conditions for the seed layer were found to be a deposition temperature of 400 °C and a laser frequency of 10 Hz.

On the seed layer, films were also deposited at 220 °C using two different procedures:

(i) deposition of the seed layer followed by cooling of the substrate and subsequent deposition of the film.

(ii) deposition of the seed layers immediately followed by the film deposition during the cooling phase.

In the latter case, it is possible to assume that an intermediate layer forms between the seed layer and the superconducting film during the cooling of the substrate; this second approach proved to be more effective in improving the superconducting properties of the films.

In addition to promoting crystallinity and lattice matching, the seed layer also plays a crucial role in preserving stoichiometric transfer from target to film, especially when low deposition temperatures, such as 220 °C, are used. This dual function makes the seed layer essential for optimizing both the structural and superconducting properties of Fe(Se,Te) thin films.

4.5 Evaluation of Superconducting Properties

For the evaluation of the superconducting properties of the samples, the transport measurements reported in this section were taken from previous studies [36], in these studies, the films were characterized using a cryogen-free cryostat equipped with an 18 T superconducting magnet. Electrical resistance and critical current density measurements were carried out as a function of temperature and applied field, employing a rotating probe to acquire the angular dependence of the critical current density while keeping the current always perpendicular to the field (maximum Lorentz force configuration). All measurements were performed in a four-probe configuration, using the standard 1 μV cm^{-1} electric criterion.

Among the various measurements available, Graph. 4.1 shows the resistance–temperature curves, which were used to extract the parameters T_c^{onset}, T_c^0, and the width of the superconducting transition. In this image we can observed the comparison between the transport measurements of the two studied films and a reference film grown on a single-crystal CaF_2 substrate: the film deposited on CZO without a seed layer (solid symbols) exhibits a broad superconducting transition, with $T_c^{onset} = 9.5$ K and $T_c^0 = 6.3$ K ($\Delta T_c = 2.6$ K), whereas the film grown with a seed layer (open symbols) shows a much sharper transition, of about 0.5 K, with T_c^{onset}= 17.2

K and T_c^0= 16.7 K, a behavior comparable to the reference CaF_2 film, indicated by black squares, which has T_c^{onset} = 18.6 K and T_c^0= 17.6 K.

Overall, these results highlight that the introduction of a seed layer significantly improves the superconducting quality of the film, reducing the transition width and bringing its performance closer to that obtained on single-crystal substrates, as reported in several studies. [74].

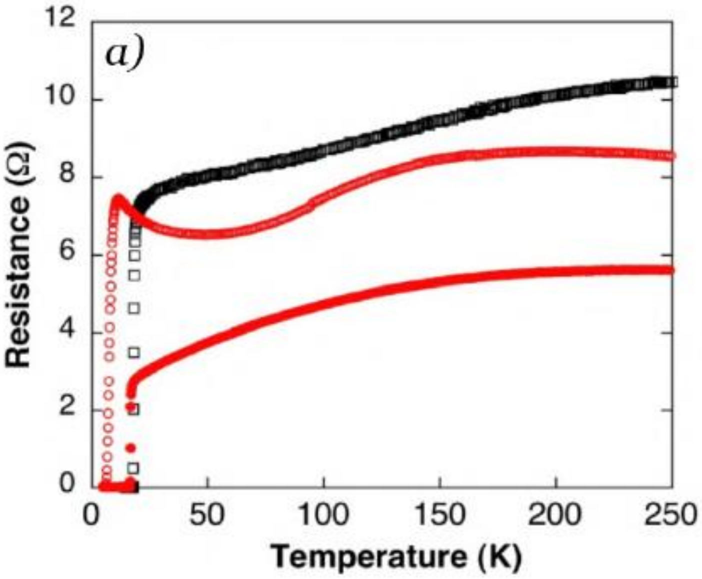

Graph. 4.1 Behaviour of the electrical resistance as a function of the temperature of Fe(Se,Te) film deposited without (open symbol) or with (full symbol) CZO-buffered YSZ substrate (red circle). Reference Fe(Se,Te) film deposited on CaF_2 single crystal substrate (black square) is shown for comparison. Image from [66]

4.6 Lithography

The as-grown film, described in the previous section, was subsequently patterned into two microbridges with a length of 1 mm and a nominal width of 50 µm.

The geometry was defined using conventional UV lithography, followed by an ion milling process with water-cooled Ar ions (energy of 500 eV). At the end of the etching, the samples underwent a brief acetone cleaning via gentle sonication and were then dried with a nitrogen flow.

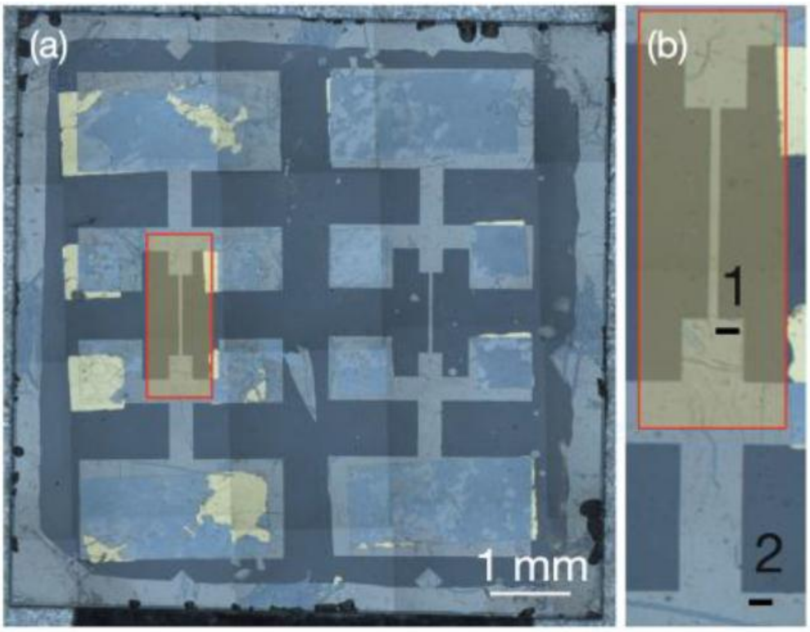

Figure 4.5 (a) Image of the patterned sample with two microbridges, where the right-side bridge was irradiated with Au ions (red rectangle). (b) Enlarged view of the irradiated microbridge highlighting the extraction regions for two TEM lamellae: irradiated (1) and non-irradiated (2). Image from [67]

Gold contacts were finally deposited on the pads dedicated to current injection and voltage measurement, to optimize the signal-to-noise ratio during electrical measurements.

The bridge subjected to irradiation — highlighted in Figure 4.5a by a red box — was used for the preparation of cross-sectional FIB lamellae.

The inset in Figure 4.5b shows the two regions selected for extraction: one belonging to the irradiated area and the other to the part not exposed to the beam [77].

4.7 XRD

Building on the results reported in previous studies [36], a comparative analysis was carried out on the structural properties of two Fe(Se,Te) thin films grown on YSZ substrates with a CZO buffer layer, one deposited directly and the other employing a seed layer. Figure 4.6 presents the corresponding θ–2θ XRD diffraction patterns. In both cases, only the (00l) reflections of Fe(Se,Te) are detected, together with the CZO peaks, indicating highly oriented epitaxial growth. The diffraction peaks associated with the buffer layer are slightly shifted toward lower angles (by approximately 0.1°), in agreement with literature reports and commonly attributed to a minor oxygen deficiency induced by deposition under ultra-high vacuum conditions [74].

Noticeable differences are observed in the angular positions of the Fe(Se,Te) reflections between the two samples, pointing to the presence of phases with different lattice parameters. As the interplanar spacing decreases with increasing selenium content, these shifts can be directly related to variations in the Se:Te ratio. In the film grown with a seed layer, the reflection at the highest angle is attributed to the seed layer itself; furthermore, increasing the deposition temperature up to 400 °C enhances the peak shift, suggesting a selenium-rich composition in this region. This behavior is consistent with the higher volatility of tellurium at temperatures above ~350 °C, where its sticking coefficient on the substrate surface is significantly reduced.

In contrast, films deposited at lower temperatures display diffraction peaks shifted toward lower angles, close to the bulk reference positions, indicating a stoichiometry closer to that of the target material. Overall, these findings demonstrate that the introduction of a seed layer not only improves the crystalline alignment and overall film quality but also contributes to maintaining the intended stoichiometry during growth, particularly at relatively low deposition temperatures (around 220 °C).

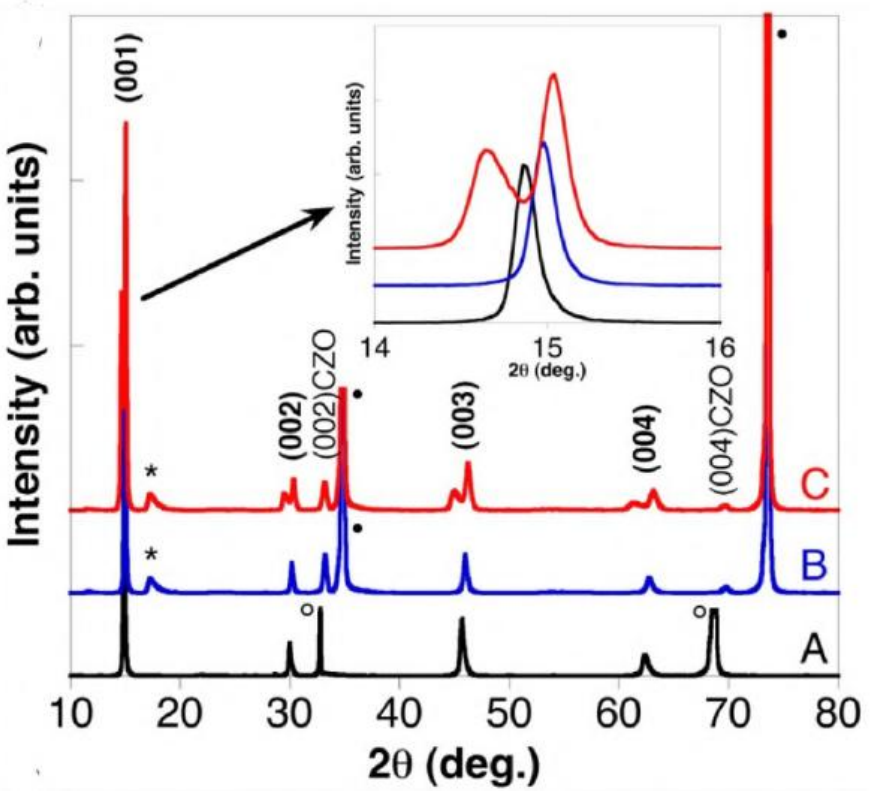

Figure 4.6 XRD analysis of Fe(Se,Te) films grown on CZO-buffered YSZ substrate without (blue, B) or with (red, C) seed layer. Reference Fe(Se,Te) film deposited on CaF_2 (black,A) is shown for comparison [61, 66]

4.8 Structural Analysis via STEM

The cross-sectional STEM image acquired in Z-contrast mode and shown in Fig. 4.7 clearly highlights the layered structure of the non-irradiated sample. The YSZ substrate, the CZO buffer layer, and the two layers composing the Fe(Se,Te) film—the non-superconducting seed layer and the upper superconducting layer—can be distinctly identified. The buffer layer exhibits pronounced surface roughness, characteristic of the deposition technique employed and previously reported in the literature [74], with an average thickness of approximately 20 nm.

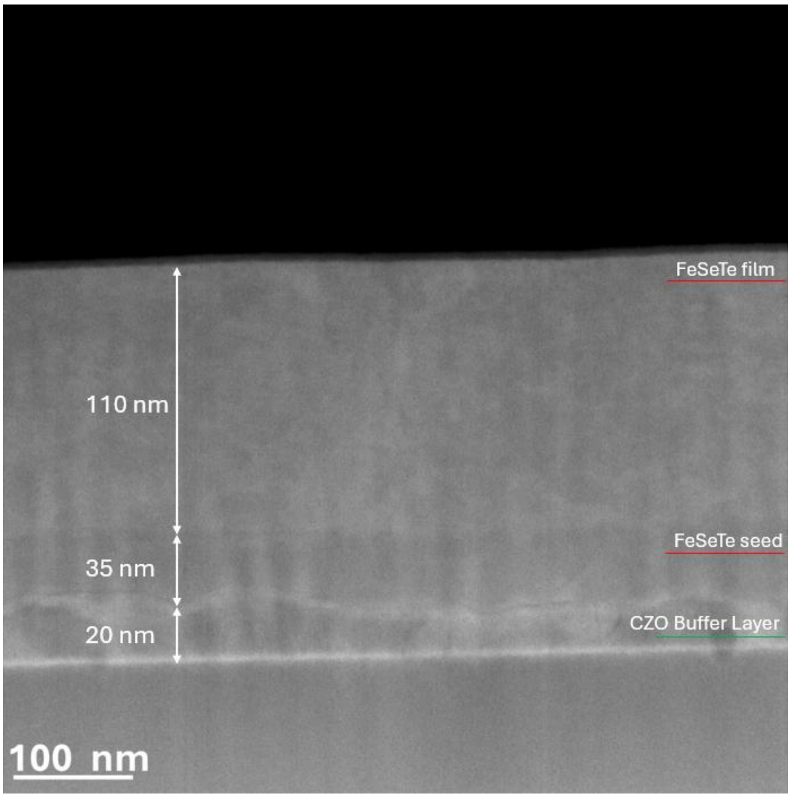

Figure 4.7 Z-contrast dark-field STEM cross-section of the Fe(Se,Te) film grown on a CZO buffer layer and YSZ substrate.

The seed and top layers measure roughly 35 nm and 110 nm, respectively, resulting in a total film thickness of about 165 nm, including the buffer.

Previous studies investigating compositional variations in similar systems have shown that the seed layer generally contains a lower tellurium (Te) content compared to the top layer. This compositional gradient, resulting from variations in growth conditions during the two-step deposition process, plays a crucial role in the superconducting behaviour, with superconductivity confined to the upper layer [73]. Vertical contrast modulations are also observed throughout the entire thickness of the Fe(Se,Te) film, presumably associated with strain fields induced by lattice mismatch between the different layers.

As observed in the high-magnification Z-contrast STEM image in Fig. 4.8, the multilayer system comprises three distinct crystalline phases, each characterized by well-defined structural and symmetry properties that strongly influence the quality of heteroepitaxial growth. The comparative scheme presented in the figure summarizes the crystal structures and space groups of the three materials, confirming the correct layering, high crystallinity, and lattice compatibility between the layers—key factors for the superconducting properties of the Fe(Se,Te) film.

To further support these observations, high-resolution STEM analysis was used to resolve the crystal structure of each layer at the atomic scale. By applying Fast Fourier Transform (FFT), the lattice parameters and crystallographic orientation of each phase was precisely determined, as illustrated in Fig. 4.9a–c. The FFT analysis reveals good lattice alignment between FeSeTe and CZO, despite the difference in crystal symmetry (tetragonal vs cubic). This favorable lattice matching is promoted by the small mismatch in lattice parameters along the key growth directions. The continuity of lattice planes across the FeSeTe/CZO interface indicates the absence of extended defects, suggesting high-quality heteroepitaxial growth, which is crucial for the superconducting properties of the film.

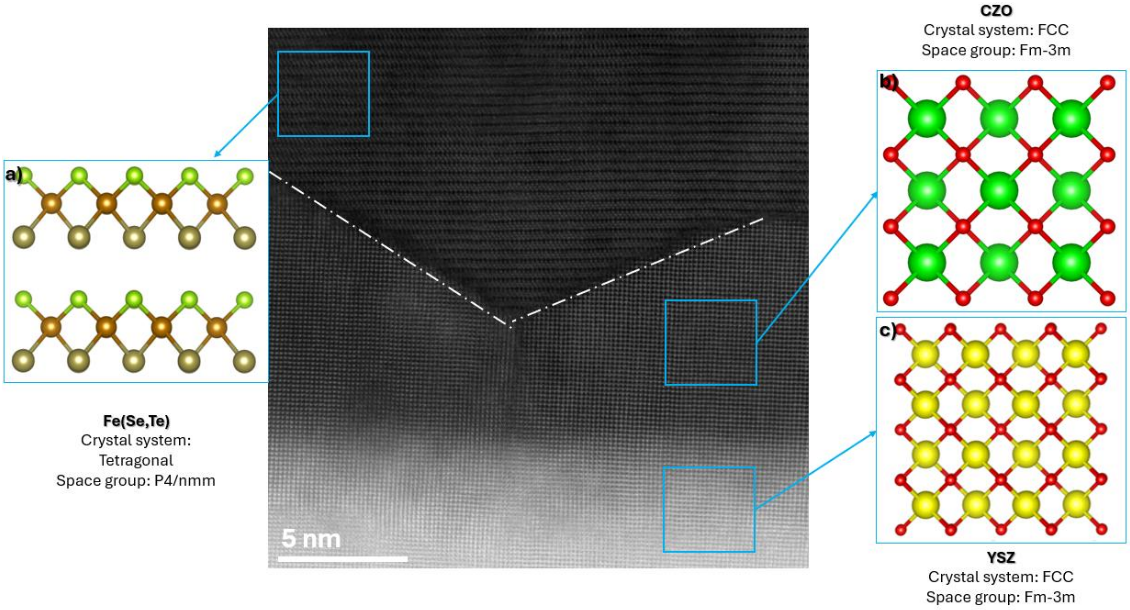

Figure 4.8 High-resolution STEM image of the Fe(Se,Te)/buffer substrate interface with CZO and YSZ. (a) Structure along the c-axis of the Fe(Se,Te) film. On the right: atomic structure of the buffer unit cells (b) CZO and (c) YSZ, both FC.

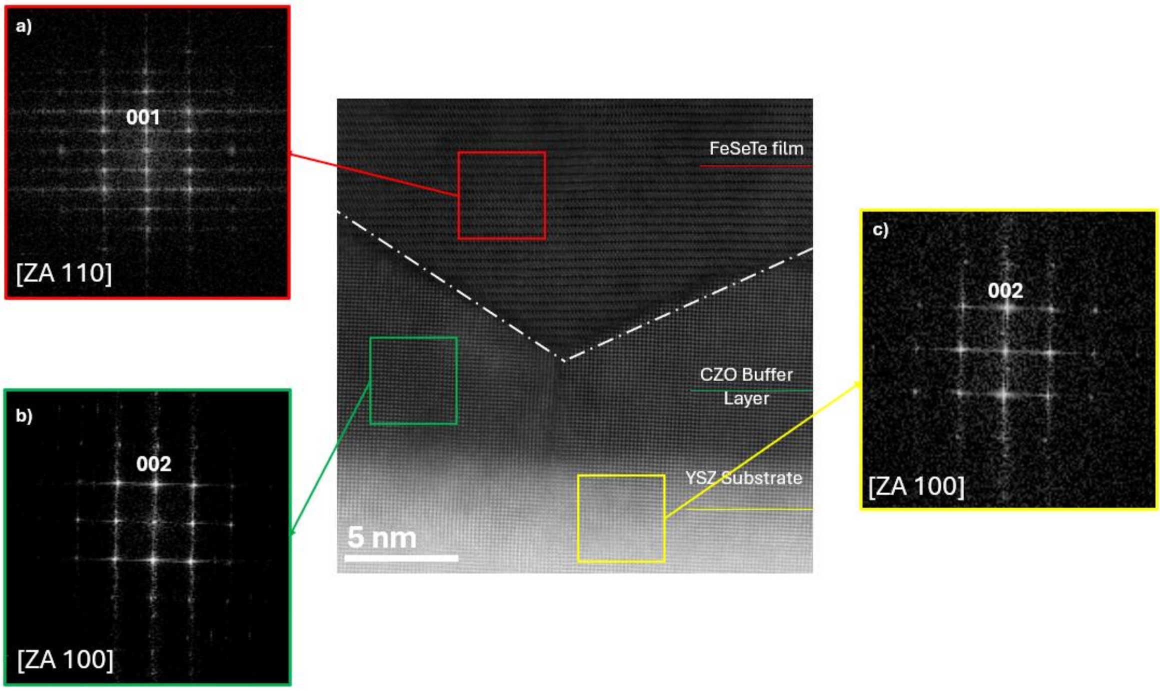

Figure 4.9 a) FFT acquired from the FeSeTe film region, showing the characteristic diffraction spots of its crystalline structure. b) FFT from the CZO buffer layer, where the 002 reflection represents the first allowed order for the fluorite structure. c) FFT from the YSZ substrate, also consistent with the stabilized cubic phase. In the center, the high-resolution STEM cross-section image highlights the FeSeTe/CZO/YSZ layer sequence.

While detailed STEM-HAADF analysis focused on the CZO/FeSeTe seed layer interface, additional investigations of the superconducting top layer reveal:

1. Epitaxial Relationship: The superconducting FeSeTe layer maintains coherent epitaxy with the underlying seed layer, as evidenced by continuous lattice fringes across the interface.

2. Defect Density: The top layer exhibits lower defect density compared to direct deposition on CZO, supporting the role of the seed layer as a structural template.

To quantify the crystal lattice deformation along the x and y (growth) directions, Geometric Phase Analysis (GPA) was applied to high-resolution STEM images. This methodology allows mapping the ε_{xx} and $\varepsilon_{\gamma\gamma}$ components of the strain tensor with nanometric resolution [78,79].

The results of the GPA analysis, Fig. 4.10c e 4.10d, reveal favorable matching at the CZO/Fe(Se,Te) interface, where no significant discontinuities are observed in the ε_{xx} strain map. In contrast, at the CZO/YSZ interface, a distinct step is observed in the strain map, indicative of greater lattice mismatch. This result underscores the beneficial role played by the CZO buffer layer in accommodating the mismatch between the YSZ substrate and the superconducting film.

The strain between CZO and YSZ is relieved through the presence of misfit dislocations located near the CZO/YSZ interface, as indicated by the red circles in Fig. 4.10a.

By examining the diffraction pattern of the analysed area (Fig. 4.10b), the spots associated with the two different lattice steps along the c-axis can be clearly distinguished in the orthogonal growth direction. Along the lateral axis, instead, the presence of separated spots reveals a lattice misalignment, whereas overlapping spots—particularly between CZO and Fe(Se,Te)—indicate good lattice matching between the two materials. The GPA maps (ε_{xx} and $\varepsilon_{\gamma\gamma}$) overlaid on the STEM image confirm these observations, highlighting regions of good compatibility along the x-direction and the presence of dislocations localized at the CZO/YSZ interface.

In contrast, the lattice mismatch between Fe(Se,Te) and CZO is very small, and no extended defects contributing to strain relaxation are observed at their interface. This favourable lattice compatibility is essential for promoting the epitaxial growth of the superconducting film.

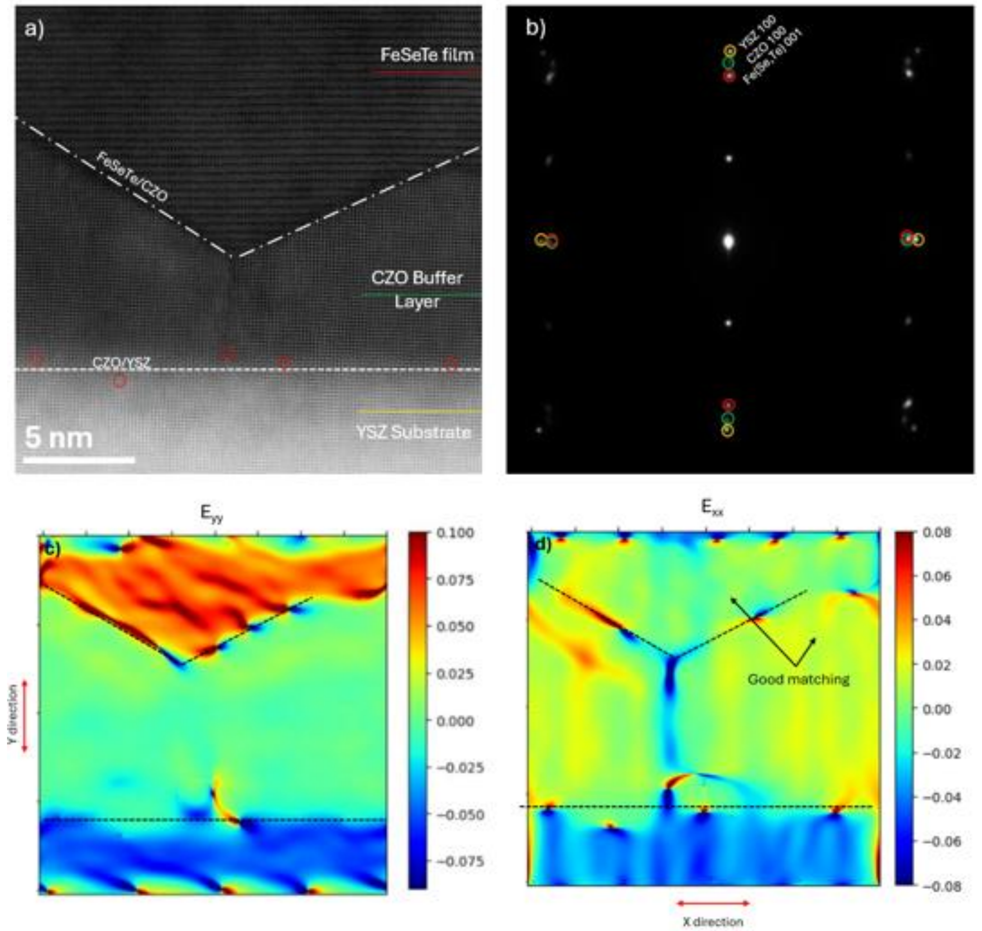

Figure 4.10 (a) High-resolution STEM image of the FeSeTe/CZO/YSZ heterostructure, showing the FeSeTe film, the CZO buffer layer, and the YSZ substrate. The FeSeTe/CZO and CZO/YSZ interfaces are clearly visible. (b) Fast Fourier Transform (FFT) of the STEM image highlighting the diffraction spots corresponding to the different layers. (c) Geometric Phase Analysis (GPA) strain map along the y-direction (ε_{yy}), revealing strain distribution across the interfaces. (d) GPA strain map along the x-direction (ε_{xx}), showing good lattice matching at the FeSeTe/CZO interface and misfit dislocations at the CZO/YSZ interface.

4.9 Irradiation of Fe(Se,Te) superconducting films

Very few studies have investigated the effect of irradiation on the superconducting properties of iron–selenium–tellurium thin films. In this work, Fe(Se,Te)/CZO/YSZ was irradiated with 230 MeV Au ions.

Irradiation with heavy ions such as Pb or Au generates correlated defects along the ion trajectory, as well as a cloud of point-like defects produced by secondary electrons generated during ion–atom collisions. Columnar defects contribute to vortex pinning and can enhance both the critical current and the irreversibility field, whereas point-like defects are mainly responsible for the increase in resistivity. Atomic-scale observations of $FeSe_xTe_{1-x}$ irradiated with 230 MeV Au ions indeed show nanometre-sized regions of crystal disorder ("columnar defects"), together with a high density of single-site atomic defects caused by secondary scattering.

Recently studies demonstrated the effectiveness of columnar defects induced by 1.15 GeV Pb-ion irradiation in tuning the critical current density of $FeSe_{0.5}Te_{0.5}$ films grown on CaF_2 crystalline substrates [80].

Conversely, it was shown that Au ions with energies of a few hundred MeV—although capable of producing columnar tracks in cuprates—induce only discontinuous tracks with a metallic core in iron-based superconductors. Based on these results, the present work investigates the effect of 230 MeV Au-ion irradiation on the pinning properties of $FeSe_{0.5}Te_{0.5}$ films grown on YSZ substrates buffered with Zr–CeO_2.

One of the two strips on the sample was irradiated at room temperature with 230 MeV Au ions at the ***Tandem accelerator*** of ***INFN–Legnaro National Laboratories*** (Italy), using two different fluences. The irradiation was performed in vacuum with the ion beam oriented perpendicular to the film surface.

The bridge area was exposed to the beam, while the current and voltage pads, as well as the second strip, were shielded using a steel mask. The first fluence was $\Phi = 2.90 \times 10^{11}\ \mathrm{cm}^{-2}$, corresponding to a dose-equivalent field of $B_{\Phi} = 6\mathrm{T}$. After characterization, the bridge was re-irradiated up to a total fluence of $\Phi = 4.84 \times 10^{11}\ \mathrm{cm}^{-2}(B_{\Phi} = 10\ \mathrm{T})$. According to Monte Carlo simulations performed with SRIM, the ions are expected to generate primarily anisotropic correlated defects along the beam direction, resulting from inelastic scattering with the target atom electrons (ionization), surrounded by a cloud of point defects produced by secondary collisions, as we can observe in Fig. 4.11.

SRIM Simulations: Monte Carlo simulations using SRIM were performed to estimate the ion stopping powers and damage distribution. The calculations predict the nuclear stopping power, the electronic stopping power, the peak damage depth and estimated displacement per atom (dpa).

It must be emphasized that SRIM provides only energy loss predictions and does not determine actual defect types (point defects, dislocations, amorphous zones, etc.). Direct TEM characterization is necessary to identify the specific damage structures.

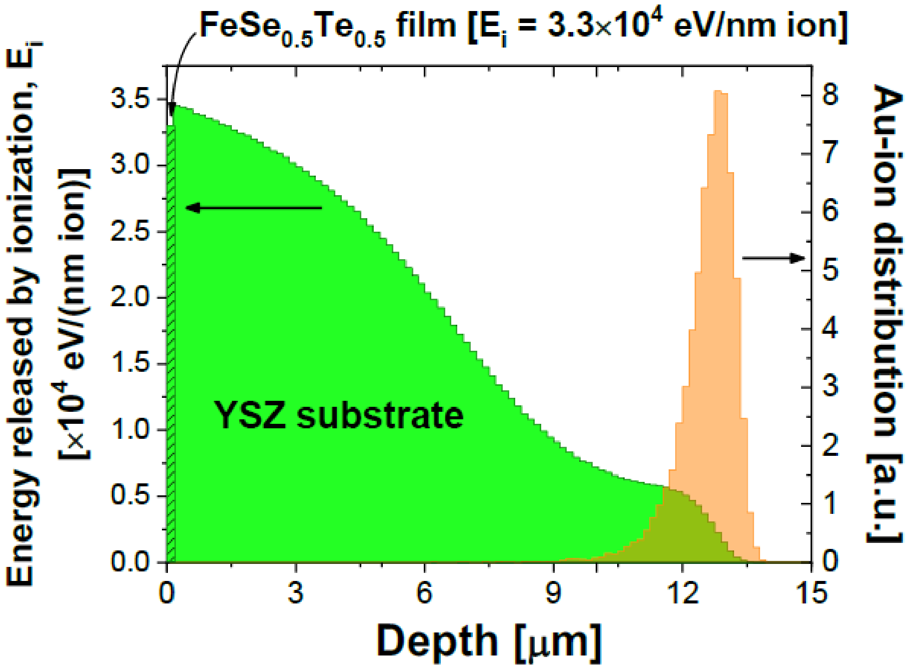

Figure 4.11 Profile of energy released by ionization and Au-ion implantation profile calculated with SRIM, showing the FST film, CZO buffer, and YSZ substrate. [65]

By comparing the pre- and post-irradiation samples, it is possible to observe how a MAADF-STEM image of the non-irradiated sample, Fig.4.12a-b, highlights the microstructural complexity of the material, composed of a multilayer system as already described in paragraph 4.8.

Contrast variations reveal point defects and low-angle grain boundaries. The point defects correspond to individual defects or small clusters that generate highly localized strain fields, enhancing the MAADF contrast. Linear contrast features identify grain boundaries, where strain modifies the local diffraction conditions.

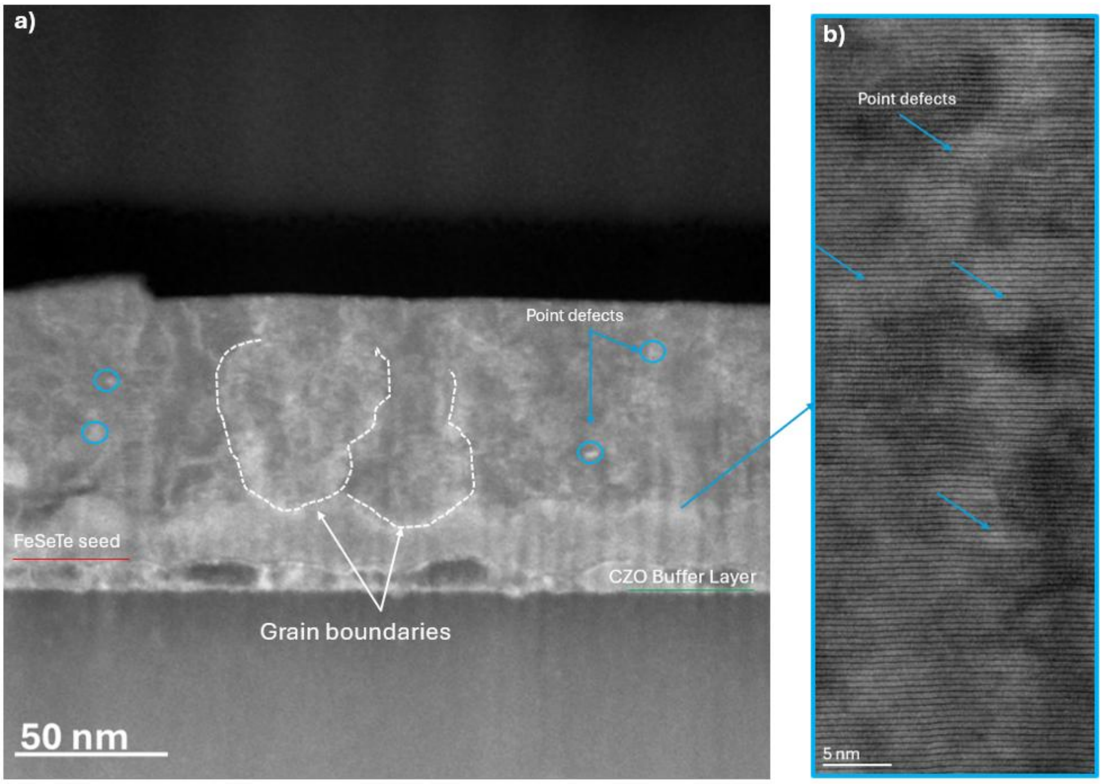

Figure 4.12 MAADF-STEM images of the CZO buffer layer. (a) Low-magnification view showing grain boundaries (dashed lines) and several point defects (circled). (b) High-magnification image of the region highlighted in (a), where isolated bright spots corresponding to point defects or small defect clusters are clearly visible.

In the irradiated sample, Fig. 4.13, structural deformations are clearly more pronounced. STEM images show both surface and interfacial protrusions, particularly evident at the FST/CZO interface and on the film surface, attributable to the impact of high-energy ions, especially in regions with abrupt variations in density and mechanical properties.

Vertically extended defect tracks are also observed, propagating from the surface into the film interior. These tracks originate near the protrusions and follow slightly tortuous paths. Rather than being perfectly linear, they exhibit a zigzag pattern, resulting from the sequence of collisions between the incident ions and lattice atoms, involving both inelastic scattering and subsequent atomic displacements.

High-magnification STEM observations reveal that these tracks are composed of chains of dislocations arranged in a staggered configuration along the ion trajectory. Despite the presence of extended defects, the overall crystalline structure of the film remains largely preserved. The defect configuration induced by irradiation can thus be described as vertically oriented dislocation arrays forming planar defects aligned along the ion beam direction.

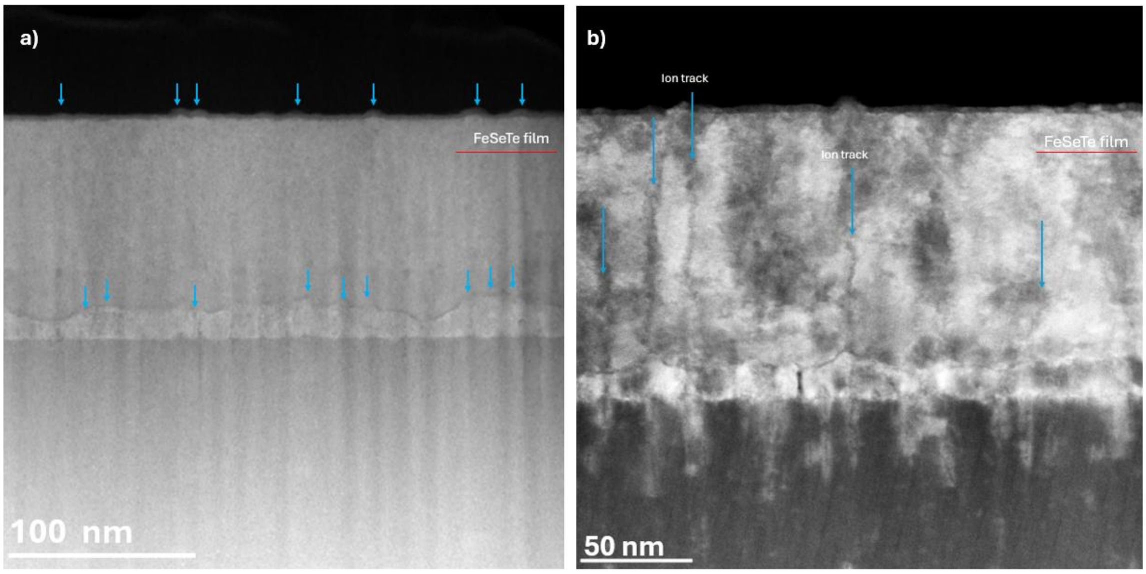

Figure 4.13 a): Z-contrast STEM image of the irradiated sample showing surface and interfacial protrusions indicated by the blue arrows. b): MAADF image of the irradiated sample showing vertical defect tracks extending through the film.

Transport measurements corroborate the microstructural observations, demonstrating the effectiveness of the irradiation-induced defects in modifying the pinning landscape. At low temperatures (T ≤ 6 K), a significant enhancement of the in-field critical current density is observed compared to the as-grown film, with $J_{c(\text{irradiated})}/J_{c(\text{as-grown})}$ ratios reaching up to 2 at 6 T and 4.2 K for samples irradiated at an equivalent fluence of 10 T. At the same time, the peak of the normalized pinning force shifts toward lower reduced field values, from h ≈ 0.32–0.33 to h ≈ 0.19–0.26, indicating a transition from point-defect-dominated pinning to a surface-core pinning mechanism. Additionally, a reduction of the angular anisotropy of J_c is observed, particularly at 6 K and 4.2 K for magnetic fields above 5 T, accompanied by the appearance of a moderate bump when the field direction is parallel to the ion tracks. These findings are fully consistent with the STEM observations, confirming that 230 MeV Au-ion irradiation introduces correlated pinning centers active in the low-temperature, intermediate-to-high-field regime. Overall, these results demonstrate that irradiation with heavy ions at intermediate energies (a few hundred MeV) represents an effective approach for defect and pinning engineering in iron-based superconductors, even though the induced defects are discontinuous and do not form continuous columnar tracks as observed in cuprate systems.

4.10 Discussion and Correlation of Microstructure with Superconducting Properties

The comprehensive structural and electrical characterization of FeSeTe thin films reveals several important insights:

1. Seed Layer Benefits: The non-superconducting FeSeTe seed layer acts as a structural template, accommodating lattice mismatch and reducing defect density in the superconducting top layer. This is reflected in sharper XRD peaks and improved superconducting transition characteristics.

2. Strain Effects: GPA strain mapping indicates compressive strain at the CZO/seed interface, which relaxes progressively through the seed layer. This strain accommodation is crucial for achieving high-quality epitaxial growth of the superconducting layer.

3. Radiation Tolerance: The relatively modest degradation of superconducting properties after ion irradiation suggests intrinsic radiation tolerance. This may be related to the layered structure of FeSeTe, which can accommodate point defects without catastrophic disruption of superconductivity.

4. Comparison with YBCO: While YBCO films (Chapter 3) achieve higher T_c values, FeSeTe offers advantages in terms of simpler crystal structure and potentially better mechanical stability. Both material systems require further optimization for fusion reactor applications.

5. CONCLUSIONS

The experimental activities presented in this work highlight the importance of optimizing every stage of the fabrication and characterization of superconducting thin films. From substrate pretreatment to deposition, oxygenation, contamination control, and post-deposition handling, each step significantly affects the final properties of the material. Special attention is also required for sample preparation for advanced analyses, such as holography, where surface flatness and controlled protective layers are essential. Cooling procedures during holography revealed that liquid nitrogen induces ice formation, suggesting the need for alternative cryogens such as helium to obtain reliable measurements.

The requirements for the use of HTS in a fusion reactor, as well as the main goals of this work, are the following:

- Being able to obtain a conductor with the desired phase;
- Assessing whether the material can withstand proximity to the plasma, i.e., in a highly radioactive environment.

My thesis mainly focused on these aspects:

- Demonstrating the feasibility of a simple coated conductor using both well-known superconductors (such as YBCO) and new families of superconductors (such as IBS, specifically FeSeTe);
- Characterizing its intrinsic properties both before and after irradiation;

- Testing the robustness of this material against irradiation with charged and neutral particles at different energies.

YBCO thin films were fabricated on STO substrates by DC sputtering as part of the experimental activities carried out on this thesis. Optimized substrate pretreatment, oxygenation, and post-deposition handling were crucial to achieve sharp superconducting transitions. Only four samples reached T_c values close to the expected range (~90–92 K), confirming the sensitivity of reproducibility to process parameters.

High-resolution structural characterization revealed a strong c-axis orientation and fully oxygenated orthorhombic YBCO. TEM analyses showed heterogeneities such as islands, particles, misoriented grains, and Y124 intergrowths, which locally influence T_c but also act as pinning centres.

Ion irradiation introduced columnar defects that served as additional pinning sites. While the superconducting transition was broadened and T_c slightly suppressed, the overall crystalline integrity was maintained. These results demonstrate the feasibility of reproducibly obtaining near-optimal T_c values by DC sputtering and highlight the key parameters requiring optimization to improve film performance and defect engineering.

FeSeTe thin films were made available through collaborating research groups and were prepared using a single CZO buffer layer. Technical substrates originally developed for ReBCO were employed, and film growth was first optimized on single crystals to simplify the architecture and ensure good lattice matching and scalable deposition. The CZO buffer was deposited using a chemical method and plays a crucial role in accommodating lattice mismatch.

In-depth STEM/TEM analysis revealed a well-defined layered structure, with a total Fe(Se,Te) thickness of ~145 nm (seed + top layer) on a 20 nm CZO buffer. Excellent lattice matching was observed at the Fe(Se,Te)/CZO interface, with local lattice deformations at morphological irregularities of the buffer that can influence superconducting properties.

Irradiation with 230 MeV Au ions produced vertically aligned defect tracks composed of dislocation chains acting as correlated planar defects. Despite the introduction of these defects, the crystalline structure remained largely intact. The induced defects significantly enhanced vortex pinning reduced the angular anisotropy of J_c, and improved in-field transport performance at low temperatures. These results confirm the feasibility of defect and pinning engineering in Fe(Se,Te) films and provide insights into the relationship between microstructure and superconducting behaviour.

Overall, the results obtained in this work indicate that both YBCO and FeSeTe thin films possess promising properties for the fabrication of HTS coils for plasma confinement in fusion reactors. High critical temperatures, well-controlled microstructure, and the possibility of engineering correlated defects to enhance vortex pinning suggest that these materials can maintain high performance even in high-field and radiation-rich environments. The optimization of buffer layers and epitaxial interfaces, particularly in FeSeTe, demonstrates the potential for constructing multi-layer coated conductors with improved structural integrity. Furthermore, the low-cost deposition methods and thin buffers explored here support the scalability of these films for technological applications. Future studies should focus on neutron and proton irradiation, large-scale mechanical and thermal stability, and the integration of these materials into full-scale coil architectures. Altogether, these findings provide outline a pathway for developing robust, high-performance superconducting conductors suitable for the demanding conditions of fusion plasma confinement.

APPENDIX AND PERSPECTIVES

Electron-optical methods for YBCO/STO

In recent years, numerous TEM techniques have been developed to investigate the magnetic properties of materials, since many magnetic characteristics — especially those relevant for technological applications — depend critically on the local microstructure and composition of the material.

Among these, two main approaches, illustrated in Fig. A.1, are:

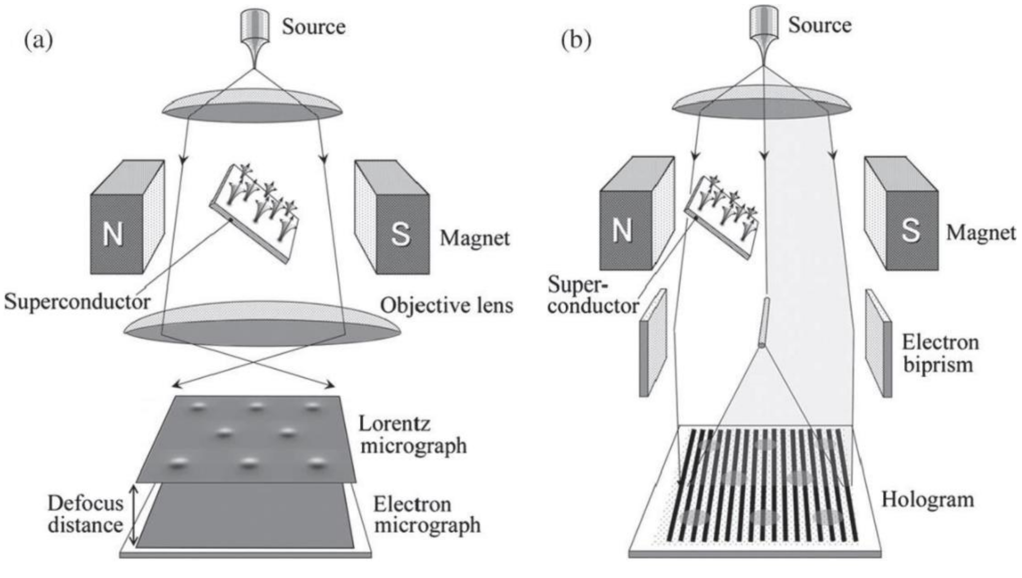

Figure A.1 Simplified diagrams of experimental setups used to study magnetic vortices in superconducting materials via transmission electron microscopy. (a) Lorentz-TEM technique: an out-of-focus image reveals beam deflection due to local magnetic fields (vortices), resulting in a Lorentz micrograph. (b) Off-axis electron holography: an electron biprism splits the beam into two coherent waves, one of which passes through the superconducting sample, enabling magnetic field reconstruction via wavefront analysis

- **Lorentz microscopy**, which focuses on analysing magnetic fields and electromagnetic phenomena within the specimen by exploiting beam deflection produced by magnetic fields or other phase-modulation methods.

- **Off-axis electron holography**, aimed at the detailed three-dimensional reconstruction of the electron wavefunction, without being limited exclusively to magnetic fields.

This thesis will focus exclusively on the latter.

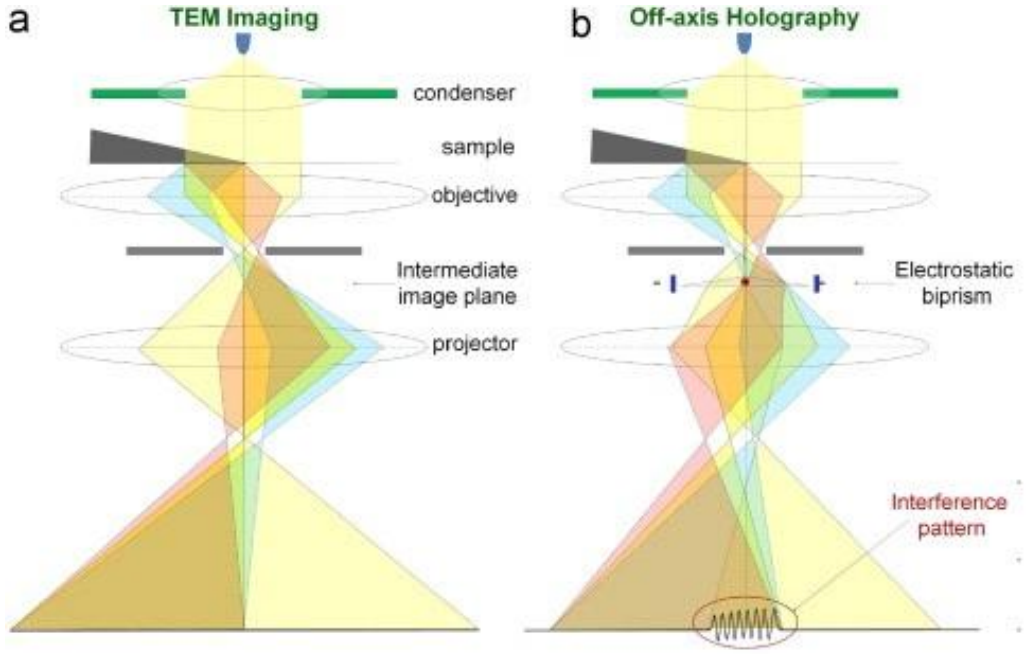

Figure A.2 Optical schemes in a TEM for (a) conventional imaging and (b) off-axis electron holography. (a) The electron beam, focused by the condenser lens, passes through the sample, is collected by the objective lens, and formed into an image at the intermediate image plane before projection. (b) In the off-axis setup, an electrostatic biprism generates a coherent reference wave that interferes with the wave transmitted through the sample, yielding an interference pattern at the projection plane, which encodes phase information (and thus electrostatic/magnetic fields)

Off-axis electron holography, first introduced by Tonomura in 1982 [81], overcomes the limitations of conventional TEM — which records only the intensity of the electron beam — by providing access to phase information, essential for studying internal electric and magnetic potentials, as shown in Fig. A.2.

This technique employs an electrostatic biprism, typically positioned between the intermediate and projector lenses of a TEM operating at 200–300 kV. The biprism deflects both the object and reference waves until they overlap with a known angle (β), generating an interferogram.

This interference pattern, characterized by fringes with a typical spacing of 5–10 nm, is magnified by the lenses and recorded as a hologram.

In this way, the analysis is carried out in Fourier space, as illustrated in the schematic in Fig. A.3, where the hologram contains three main contributions:

- **Central band**, which corresponds essentially to the conventional TEM image. It contains elastic and inelastic electrons but no phase information and is therefore discarded in holographic analysis.

- **±1 sidebands**, which contain the full Fourier spectrum of the image wave.

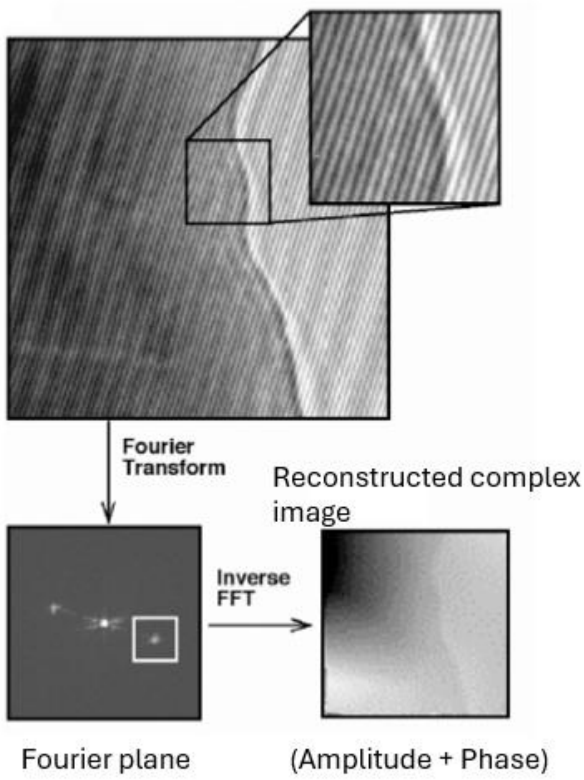

Fast Fourier Transform (IFFT) is then applied to extract the reconstructed complex image, which contains both amplitude and phase information

These bands have the advantage of including only elastic electrons, with amplitude and phase linearly related to the object’s properties. Since the two sidebands are complex conjugates, they are equivalent and redundant: either one alone contains all the required information, including quantum noise. Typically, the +1 sideband, centered at q = 0 (the spatial frequency vector), is selected using an aperture, and from it the numerical reconstruction of the complex wavefunction (amplitude + phase) is obtained [82].

With this method, two main contributions to the modulation of the object wave can be distinguished:

1. **Amplitude modulation**, arising from elastic and inelastic scattering, multiple interference, loss of coherence, and absorption contrast.
2. **Phase modulation**, associated with the phase shifts accumulated by the electron beam as it passes through electric and magnetic potentials, thereby enabling the direct mapping of the material's internal properties.

The resulting phase maps allow for the quantitative determination of the mean inner potential and of the magnetic fields integrated along the beam direction. The reliability of these results depends strongly on the fidelity of the reconstructed wavefunction relative to the actual wavefunction in the microscope, as well as on the accurate correction of optical and geometric aberrations [83].

Overall, off-axis electron holography is an extremely powerful tool for the quantitative characterization of the structural and magnetic properties of materials at the nanometer scale, providing a direct and high-resolution view of the internal phenomena that govern the functional behaviours of advanced materials.

To investigate the magnetic behaviours of the YBCO films deposited on STO and the effect of the etching treatment, we selected the samples Smp$_{\_LE}$, Smp$_{\_SE}$, and Smp$_{\_SE.I}$ for off-axis electron holography analysis. The measurements will be carried out both at room temperature and at temperatures close to T_c, to highlight variations in vortex distribution and pinning mechanisms induced by the etching process.

The analyses were performed at the ***CNRS-CEMES*** laboratories in Toulouse (France) using a ***HITACHI HF3300C-I2 TEM*** equipped with a biprism.

The use of two biprisms makes it possible to:

– improve the spectral separation between the central band and the sidebands, allowing a clearer isolation of phase and amplitude information;

– reduce artifacts caused by Fresnel fringes, typically introduced by the biprism electrode.

– optimize the stability of the interferometer, compensating for any residual vibrations or system instabilities that could compromise the holographic reconstruction [84].

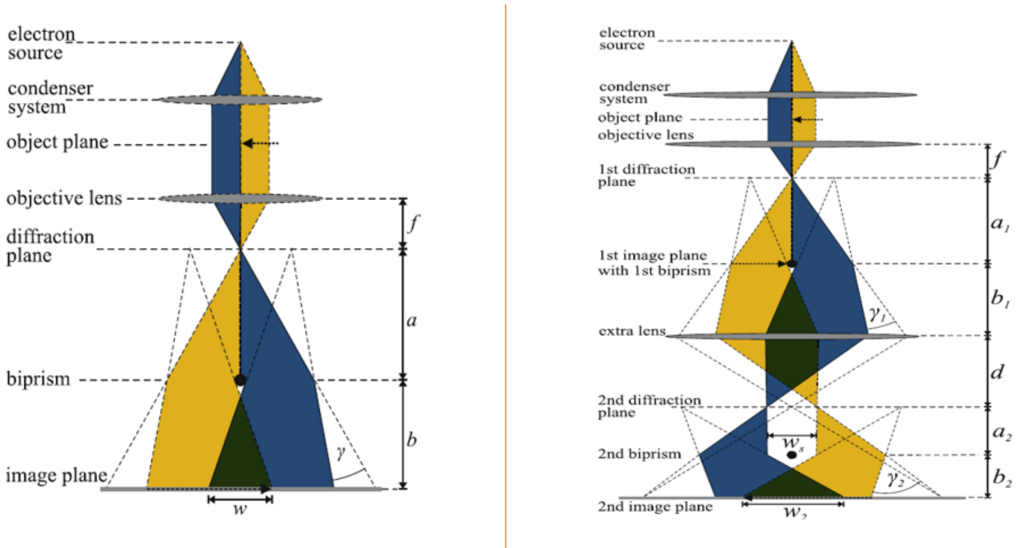

1 BIPRISMA

2 BIPRISMA

Figure A.3 Workflow of off-axis electron holography reconstruction. The recorded hologram undergoes a Fourier Transform to isolate one of the sidebands in the Fourier plane. An Inverse Fast Fourier Transform (IFFT) is then applied to extract the reconstructed complex image, which contains both amplitude and phase information

Analyses using this technique were also made possible thanks to the use of a double-tilt sample holder, which allows the specimen to be tilted along two orthogonal axes. This capability facilitates observation from multiple orientations and improves the three-dimensional characterization of the structures.

The measurements were initially carried out at room temperature and in zero magnetic field, and only later at low temperature and under magnetic fields up to 2 T, to observe the material's behaviours as a function of temperature.

Thin YBCO films grown on substrates such as STO are generally in the normal state at temperatures above their critical temperature ($T_c \approx 90–93$ K). In this regime, they do not exhibit long-range intrinsic magnetic order, while any weak paramagnetic signatures are typically attributable to structural defects, impurities, or substrate contributions. As the temperature approaches T_c, pairing fluctuations and partial magnetic shielding begin to appear; the transition can be relatively sharp, although its width depends on film quality, homogeneity, and doping.

Below T_c (e.g., at 77 K), the film enters the fully superconducting state and exhibits perfect diamagnetism, completely expelling the applied magnetic field in accordance with the Meissner effect [85].

The $Smp_{\_SE}$ sample was analysed using off-axis electron holography, producing pairs of color-coded phase maps labelled "up" and "down" depending on the orientation of the specimen relative to the beam. By comparing the two maps, the electrostatic components (Mean Inner Potential, MIP) can be separated from the magnetic contributions, and variations in thickness as well as local defects can be assessed.

In practice, the electrostatic component is obtained as reported in Eq.A.1

$$\varphi_{\mathrm{elec}} = (\varphi_{\mathrm{up}} + \varphi_{\mathrm{down}})/2 \quad \text{(eq.A.1)}$$

while the magnetic component (which changes sign upon sample reversal) is obtained from Eq. A.2.

$$\varphi_{\mathrm{mag}} = (\varphi_{\mathrm{up}} - \varphi_{\mathrm{down}})/2. \quad \text{(eq.A.2)}$$

An average value of the phase difference Δφ close to zero in the analysed region indicates the absence of a resolvable magnetic signal under the experimental conditions (i.e., no detectable domains/vortices above the noise level and spatial resolution of the measurement). However, this does not completely rule out the presence of weak or sub-resolution magnetic structures.

For the $\mathrm{Smp}_{\_\mathrm{SE}}$ sample, however, some issues emerged due to the surface irregularities. The technique is extremely sensitive to the thickness of the carbon (C) layer: a thickness exceeding 50–60 nm can introduce artefacts that prevent an accurate analysis, as it increases the characteristic beam angle, which no longer fully illuminates the region of interest.

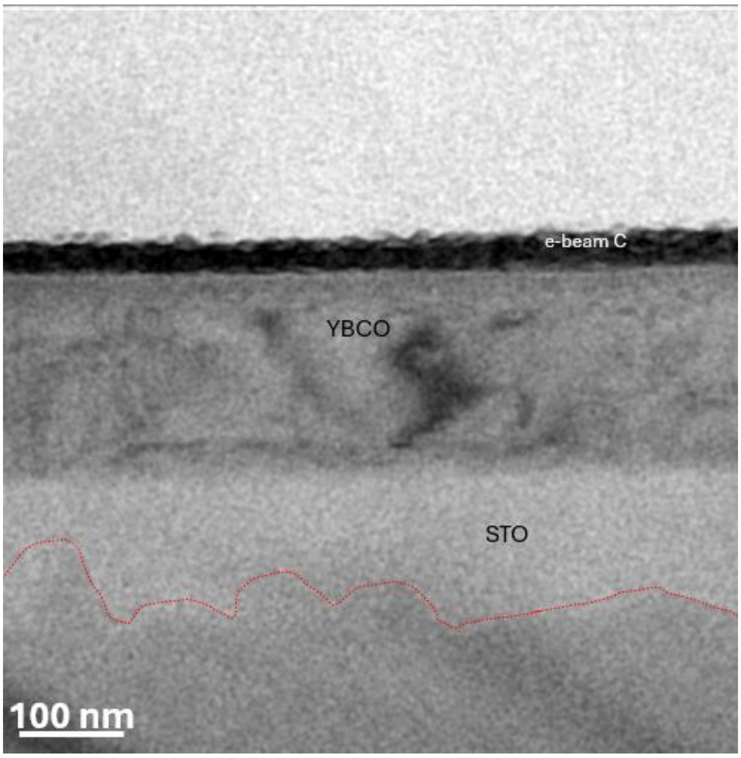

Figure A.5 Off-axis TEM image of a cross-sectional view of the sample. The protective carbon layer (C layer), the superconducting YBCO film, and the $SrTiO_3$ (STO) substrate are clearly visible. The red dashed line highlights the formation of a shadow on the substrate, attributed to an excessive thickness of the C layer, which can introduce artifacts and distortions in the reconstruction of the electron hologram.

Moreover, a thicker carbon layer increases the mean inner potential and contributes to the measured phase shift, causing phase delays and possible artefacts arising from beam–sample interaction, as highlighted by the pronounced shadow observed on the specimen (Fig. A.5). For this sample, the up and down phase maps (Fig. A.6) show that the material does not exhibit any significant detectable magnetic flux. Negative phase values may indicate slight residual polarization or surface-charge effects rather than a genuine magnetic signal.

In addition, the surface irregularities introduce distortions and unwanted diffraction, further complicating the interpretation of the data.

The subsequent samples were analysed using two differential interferometric approaches:

– ΔT: comparison between room temperature and temperatures close to that of liquid nitrogen (77 K);

– ΔB: comparison between measurements acquired at magnetic fields of B = 1 T and B = 2 T, with the specimen tilted by 20° relative to the beam.

Low-temperature measurements were carried out using a cryogenic sample holder (cryo-TEM holder). This system is typically cooled using liquid nitrogen or liquid helium (or closed-cycle systems) and is equipped with temperature sensors and resistive heaters for thermal stabilization.

The cryo-holder used allows tilting along two axes, enabling acquisitions from multiple orientations to rule out projection effects.

For each pair of conditions (ΔT or ΔB), repeated interferometric phase maps were acquired, spatially aligned, and converted into differential maps by performing pixel-by-pixel subtraction after proper phase unwrapping and background gradient correction.

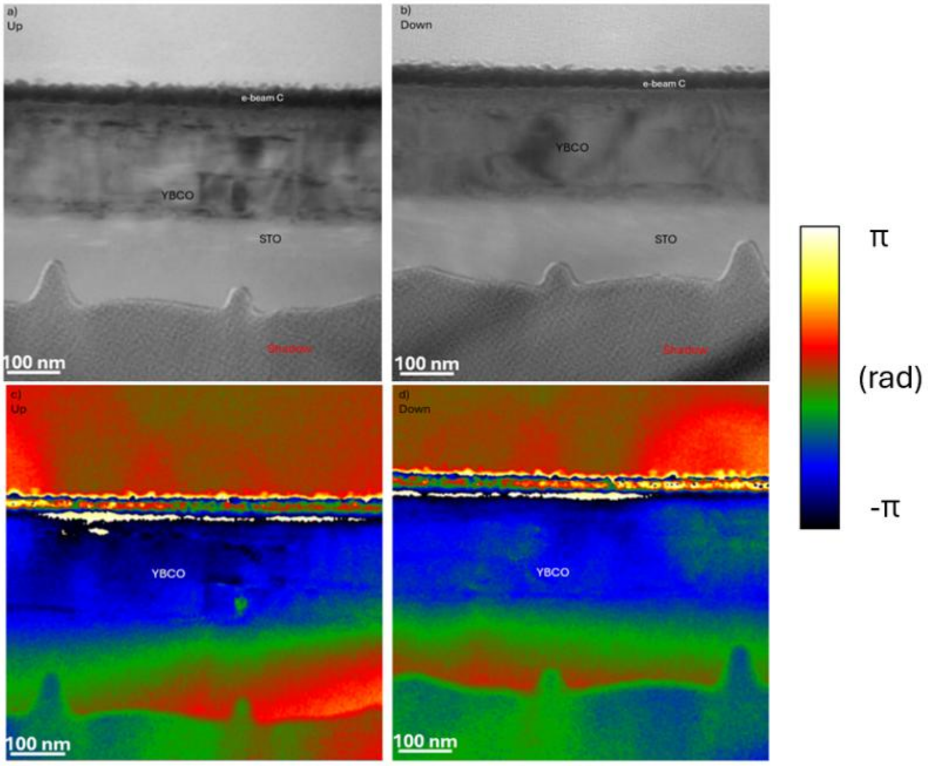

Figure A.6 TEM images (left) and corresponding phase maps (right) acquired via off-axis electron holography, obtained by observing the sample from two opposite orientations ('up' and 'down'). The YBCO superconducting film deposited on an STO substrate is clearly visible. The color-coded phase maps highlight the contribution of the mean inner potential (MIP) and residual fields of the microscope. The colour scale represents the phase shift in radians, ranging from –π (blue) to +π (yellow/red). The absence of significant differences between the two acquisitions indicates that no measurable magnetic flux is present in the sample under these conditions.

This subtraction removes common components (e.g., MIP or lens gradients) and highlights the variations between the conditions, while still requiring caution regarding possible artefacts arising from drift, thermal contraction, or registration mismatches.

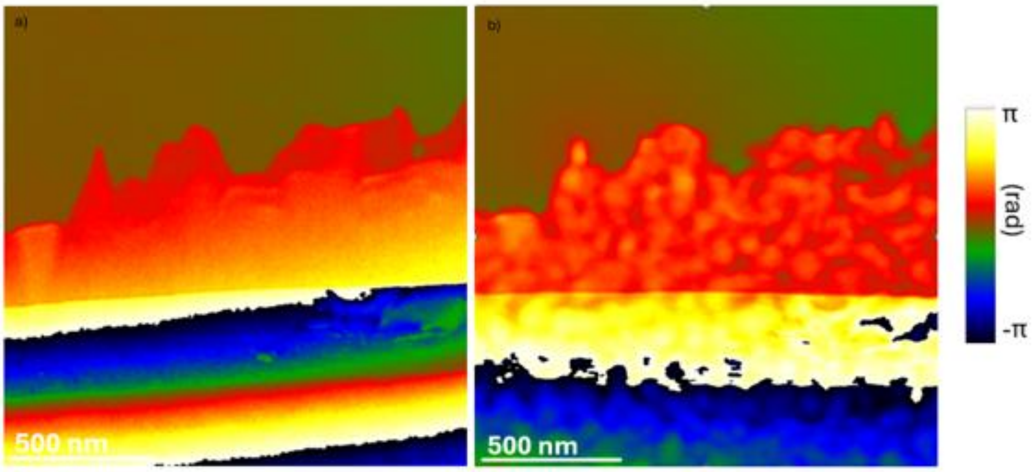

T= 23°C T= -161 °C

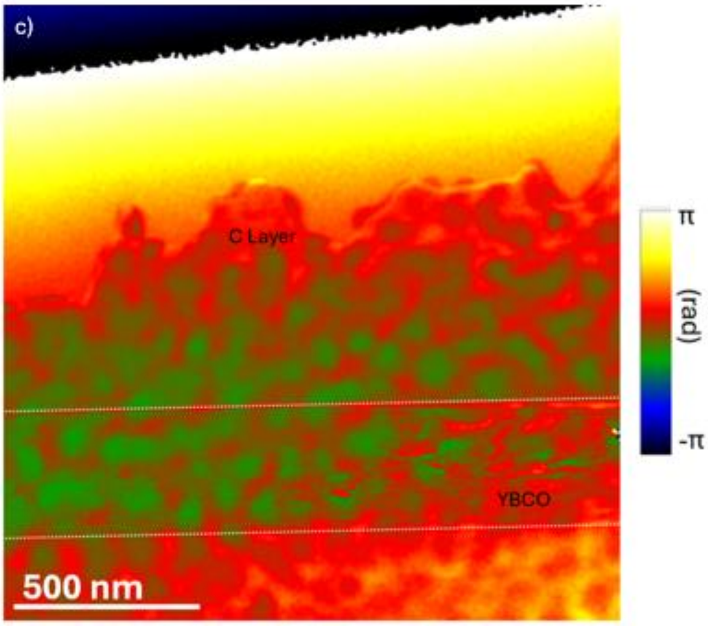

Figure A.7 Color-coded phase maps acquired via off-axis electron holography at room temperature (T = 23 °C, top left) and at low temperature (T = –161 °C, top right), together with the differential phase map (bottom) obtained by subtracting the two acquisitions. The colour scale represents the phase shift in radians, from –π (blue) to +π (yellow/white). The differential map highlights local changes potentially associated with magnetic flux behaviour; however, the presence of strong phase noise and shadowing effects, possibly due to ice formation and sample contamination, significantly affects the reliability of the interpretation.

In the case of the non-irradiated sample, as shown in image C of Fig. A.7, it was not possible to detect any magnetic phase shift associated with flux induction in the sample.

Conversely, it is very likely that the analysis was compromised by the presence of ice formations, clearly visible in image B of Fig. A.7, which reduce the reliability of the result.

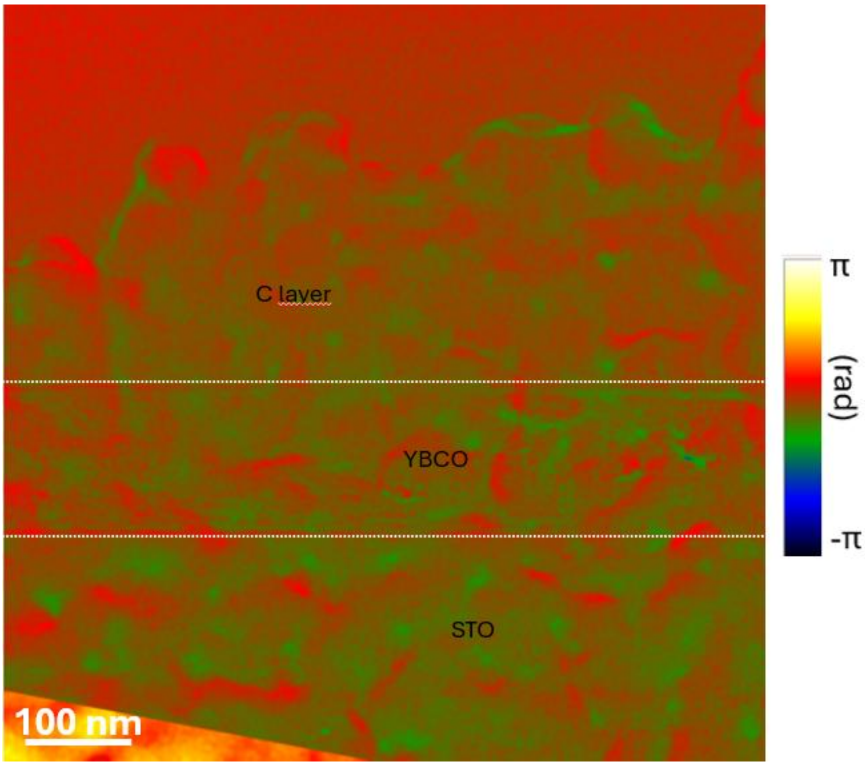

Figure A.8 Phase difference map obtained by off-axis electron holography on a YBCO/STO film. The image shows the phase variation (in radians) between 1 T and 2 T. Ice formation on the sample is clearly visible, particularly in the lower region, affecting the interpretation of the local magnetic response.

These ice formations, already present at 128.15 K, also prevented further cooling down to the actual liquid nitrogen temperature (77 K). Even when applying two different magnetic fields, 1 T and 2 T respectively, the subtraction image (Fig. A.8) does not reveal any significant information for assessing the behaviour of the superconductor at low temperature. The presence of ice, in fact, alters the Mean Inner Potential (MIP) and introduces local phase distortions, preventing a reliable quantitative analysis of the sample.

In the Smp_$_{\mathrm{SE.I.}}$ sample as well, ice formation prevented the extraction of reliable information from the specimen. This issue, combined with the inability to reach the material’s critical temperature — since the cooling system operated exclusively with liquid nitrogen — made it particularly challenging to complete the analyses using off-axis electron holography.

REFERENCES

[1] V. Shafranov, “On the history of the research into controlled thermonuclear fusion” Journal of the Russian Academy of Sciences, vol. 44, no. 8, p. 835–865, 2001.

[2] M. Zucchetti et al., “Neutronics Scoping Studies for Experimental Fusion Devices” FUSION SCIENCE AND TECHNOLO, vol. 75, no. 5, pp. 423-428, 2019.

[3] D. Larbalestier et al, “Isotropic round-wire multifilament cuprate superconductor for generation of magnetic fields above 30 T” Nature Mater, vol. 13, pp. 375-381, 20014.

[4] D. Larbalestier et al, “High-T_c superconducting materials for electric power applications” Nature, vol. 414, pp. 368-377, 2001.

[5] R. Fuger et al., “YBCO Coated Conductors for Fusion Magnets” IEEE TRANSACTIONS ON APPLIED SUPERCONDUCTIVITY, vol. 19, no. 3, pp. 1532-1535, 2009.

[6] G. G. P. Parravicini, Solid State Physics, Elvesier, 2014.

[7] E.Dagotto, “Correlated electrons in high temperature superconductors” Rewviews of Modern Physics, vol. 66, no. 3, pp. 763-840, 1994.

[8] J. Bardeen, “Theory of Superconductivity” Physical Review , pp. 1175-1204, 1957.

[9] M. Tinkham, Introduction to Superconductivity, New York: Dover Books on Physics, 1996.

[10] G. Blatter et al., "Vortices in high temperature superconductors" Reviews of Modern Physics, vol. 66, no. 4, pp. 1125-1388, 1994.

[11] D. Dew-Hughes, "Flux pinning mechanisms in type II superconducotrs" The Philosophical Magazine: A Journal of Theoretical Experimental and Applied Physics., vol. 30, no. 2, pp. 292-305, 1974.

[12] L. Civale et al., "Vortex confinement by columnar defects in $YBa_2Cu_3O_7$ crystal: Enhanced pinninh at high field and temperatures" Physical Review, vol. 65, no. 9, pp. 1164-1167, 1990.

[13] D Daghero et al., "Decoupling of critical temperature and superconducting gaps in irradiated film of a Fe-based superconductor" Supercond.Sci. Technol., 2018.

[14] J. Fogt et al., "Effect of Proton Irradiation on Thin-Film $YBa_2Cu_3O_{7-\delta}$ Superconductor" Materials , 2024.

[15] National Academies of Sciences, Bringing Fusion to the U.S . Grid, 2021.

[16] G. M. B. S. e. a. Creely AJ, "Overview of the SPARC tokamak" Journal of Plasma Physics, vol. 86, no. 5, 2020.

[17] "First Online," 29 ottobre 2024. [Online]. Available: https://www.firstonline.info/eni-e-mit-ottengono-il-via-libera-per-sparc-il-prototipo-di-fusione-nucleare-che-promette-energia-pulita-e-illimitata/.

[18] A. Rathi, "Quartz," 21 July 2022. [Online]. Available: https://qz.com/1402282/in-search-of-clean-energy-investments-in-nuclear-fusion-startups-are-heating-up.

[19] D. Clery, “Science,” 3 Marzo 2021. [Online]. Available: https://www.science.org/content/article/fusion-startup-plans-reactor-small-powerful-superconducting-magnets.

[20] “Torino News 24.it,” 23 marzo 2023. [Online].

[21] D. Dijkkamp et al., “Preparation of Y-Ba-Cu oxide superconductor thin films using pulsed laser evaporation from high Tc bulk material” Applied Physics Letters, vol. 51, no. 8, 1987

[22] L. Piperno et al,. “Interaction between untreated $SrTiO_3$ substrates and solution-derived $YBa_2Cu_3O_7$-δ films”. Applied Surface Science,2020, 528, 146402.

[23] Domínguez et al.,”$YBa_2Cu_3O_7$ films grown onto $SrTiO_3$ and YSZ substrates by chemical solution deposition of trifluoroacetates”, Journal of Electroceramics 47, 15–22 (2021)

[24] S.K. Shrivastava et al., “Preparation and characterization of superconducting YBCO thin films deposited by magnetron sputtering technique”. International Journal of Research in Engineering and Science, 2024, 12(4), 175–184.

[25] Y. Kamihara, et al. “Iron-based layered superconductor $La[O_{1-x}F_x]FeAs$ (x = 0.05–0.12) with T_n = 26 K”. Journal of the American Chemical Society, 2008, 130, 3296–3297.

[26] Yeh, K.-W., et al. “Tellurium substitution effect on superconductivity of the alpha-phase iron selenide $FeSe_{1-x}Te_x$”. Europhysics Letters, 2008, arXiv:0808.0474.

[27] L. Piperno, “High-performance Fe(Se,Te) films on chemical CeO_2-based buffer layers” Scientific Reports, vol. 13, no. 1, 2023.

[28] S. M. George, “Atomic Layer Deposition: An Overview” Chemical Reviews, vol. 110, 2009.

[29] Prof. Dr. Toivo T. Kodas, The Chemistry of Metal CVD, 1994.

[30] G. W. Scherer et al., Sol-Gel Science, 1990.

[31] E. Bellingeri et al., “High quality epitaxial $FeSe_{0.5}Te_{0.5}$ thin films grown on $SrTiO_3$ substrates by pulsed laser deposition” Superconductor Science and Technology, vol. 22, no. 10, 2009.

[32] Y. Uzun, et al., Fabrication of Superconducting $YBa_2Cu_3O_{7-x}$ Thin Films on Si Wafer via YSZ/CeO_2 buffer layers. *J Supercond Nov Magn* **30**, 2335–2340 (2017).

[33] Gupta, A. K., & Singh, D. (2024). *Optimizing deposition techniques and parameters for high-Tc YBCO thin films*. Journal of Advances and Scholarly Researches in Allied Education, *21*(1), 394–406.

[34] M.Iebole, Study of the Irradiation Effects on Superconducting Films of Iron-Based Superconductors., Genova: PhD Thesis, 2024

[35] F. Rizzo et al., “Correlated Defect Formation and Pinning Enhancement in 230 MeV Au-Ion-Irradiated Superconducting Fe(Se,Te) Thin Films” Science and Technology of Advanced Materials", **submitted**, 2025.

[36] M. Fracasso et al., “Effects of high-energy Pb-ion irradiation on critical current and flux pinning in Fe(Se,Te) thin films” Supercond. Sci. Technol., 2025.

[37] J. Mayer, et al. “TEM Sample Preparation and FIB-Induced Damage” MRS Bulletin, vol. 32, pp. 400-407, 2007.

[38] M. K. Wu et al., “Superconductivity at 93 K in a new mixed-phase Y-Ba-Cu-O compound system at ambient pressure” Phys. Rev. Lett., vol. 58, 1987.

[39] J. F. Ziegler, et al. “SRIM – The Stopping and Range of Ions in Matter (2010)”, *Nuclear Instruments and Methods in Physics Research Section B*, 268 (2010) 1818-1823

[40] J.D. Pedarnig et al., “Surface planarization and masked ion-beam structuring of $YBa_2Cu_3O_7$ thin films” Thin Solid Films, vol. 518, pp. 7075-7080, 2010.

[41] J. Hua et al., “Vortex pinning by compound defects in $YBa_2Cu_3O_{7-\delta}$” Physical Rewiew B, 2010.

[42] J.D. Jorgensen et al., “Structural properties of oxygen-deficient $YBa_2Cu_3O_{7-\delta}$” Phys Rev B Condens Matter, vol. 41, no. 4, 1990.

[43] J. L. Tallon, “Oxygen in High-T_c Cuprate Superconductors” in Frontiers in Superconducting Materials., Springer, 2005.

[44] J. P. Locquet et al., “Doubling the critical temperature of $La_{1.9}Sr_{0.1}CuO_4$ using epitaxial strain” Nature, pp. 453-456, 1998.

[45] S. I. Bondarenko et al., “High-temperature superconductors of the family $(RE)Ba_2Cu_3O_7$-δ and their application (Review Article)”. Low Temperature Physics, 2018, 43(10), 1125–1139.

[46] J.Mannhart & Schlom, D. G. “Oxide interfaces—An opportunity for electronics”. Science, 2010, 327(5973), 1607–1611.

[47] **M.** Bluschke et al., “Stabilization of three-dimensional charge order in $YBa_2Cu_3O_{6+x}$ via epitaxial growth”. Nat Commun., 2018 Jul 30 ;9(1):2978.

[48] A. Perrin, et al. “D.C. sputtering elaboration of thin films of the high-Tc superconductor $YBa_2Cu_3O_7$-x: evidence for strong film-substrate interactions”, Rev. Phys. Appl. 23, 1988, 257–264

[49] J. Zhang, et al. “Progress in the Study of Vortex Pinning Centers in High-Temperature Superconducting Films”. Nanomaterials 2022, 12, 4000.

[50] J. Zhang, et al. “A Review on Strain Study of Cuprate Superconductors”. Nanomaterials (Basel). 2022 Sep 25;12(19):3340.

[51] S. R. Foltyn, et al. “Materials science challenges for high-temperature superconducting wire”. Nature Materials,2007, 6(9), 631–642.

[52] G. Blatter, et al. “Vortices in high-temperature superconductors”. Reviews of Modern Physics, 1994 66, 1125–1388.

[53] M. Varela, et al., “Direct correlation between Tc and CuO_2 bilayer spacing in $YBa_2Cu_3O_7$-x,” arXiv:cond-mat/0208584, 2002. [Online].

[54] “Stanford Advanced Materials,” [Online]. Available: https://www.samaterials.it/crystal-substrates/2429-strontium-titanate-sto-crystal-substrates.html.

[55] F. V. E. Hensling et al., “$SrTiO_3$ termination control: a method to tailor the oxygen exchange kinetics” Materials Research Letters, vol. 8, no. 1, pp. 31-40, 2019

[56] A. Plaza et al., “The role of etching anisotropy in the fabrication of freestanding oxide microstructures on $SrTiO_3$(100), $SrTiO_3$ (110), and $SrTiO_3$ (111) substrates” Applied Physics Letters, 2021.

[57] M. Kawasaki et al., “Atomic Control of the $SrTiO_3$ Crystal Surface” Science, 1994.

[58] G. Koster et al., “Surface Morphology Determined by (001) Single-Crystal $SrTiO_3$ Termination” Physica C: Superconductivity, pp. 215-230, 2000.

[59] S. K. Shrivastava et al., “Preparation And Charaterisation of Superconducting YBCO Thin Films Deposited By Magnetron Sputtering Technique” International Journal of Research in Engineering and Science, pp. 175-184, 2024.

[60] A.Gupta et al., “$YBa_2Cu_3O_{7-\delta}$ Thin Films Grown by a Simple Spray Deposition Technique” Applied Physics Letters, pp. 163-165, 1988.

[61] S. K. Mishra et al., “Lithographic patterning of superconducting YBCO films” Journal of Superconductivity, vol. 5, pp. 445-449, 1992.

[62] C. H. Chen et al., “Antiphase domain boundaries in the superconducting phase of the Y-Ba-Cu-O system,” Phys. Rev. B , no. 35, pp. 8767-8773, 1987.

[63] C. L. Jia et al., “A study of antiphase boundaries and "223" planar faults in epitaxial $YBa_2Cu_3O_7$ films by high resolution electron microscopy” Physica C: Superconductivity and its Applications, vol. 182, pp. 163-170, 1991.

[64] J. Garcia-Barriocanal et al., “Disorder-controlled superconductivity at $YBa_2Cu_3O_{7-}$/$SrTiO_3$ interfaces” Phys. Rev. B, no. 87, 2013.

[65] P. Romano et al., “Tunnel spectroscopy into the $YBa_2Cu_4O_8$ compound” Il Nuovo Cimento D, vol. 16, p. 1885–1888, 1994.

[66] A. Trajnerowicz et al., “Isotope effect on the optical phonons of $YBa_2Cu_4O_8$ studied by far-infrared ellipsometry and Raman scattering” Physical Review B, vol. 74, 2006.

[67] Tonomura A, “Applications of electron holography” Reviews of Modern Physics, no. 59, pp. 639-669, 1987.

with high energy heavy ions” Appl. Phys. Lett., vol. 63, pp. 1573-1575, 1993.

[68] S. Ashish Kumar Gupta et al., “Nanoscale core–shell structure and recrystallization of swift heavy ion tracks in $SrTiO_3$” Nanoscale, vol. 16, pp. 14366-14377, 2024.

[69] G. R. Stewart, “Superconductivity in iron compounds” Rev. Mod. Phys, vol. 83, pp. 1589-1652, 2011.

[70] M. H. Fang et al., “Superconductivity close to magnetic instability in $Fe(Se_{1-x}Te_x)_{0.82}$” Phys. Rev. B , vol. 78, 2008.

[71] T. Taen et al,, “Superconductivity at T_c~14K in single-crystalline $FeTe_{0.61}Se_{0.39}$” Physical Review B, vol. 80, 2009.

[72] W. Lynn et al., “Neutron studies of the iron-based family of high T_C magnetic superconductor” Physica C, p. 469–476, 2009.

[73] L. Piperno, “Chemical CeO_2-based buffer layers for Fe(Se,Te) films”, IEEE transactions on applied superconductivity , vol. 32, 2022.

[74] S. Molatta et al., “Interface control by homoepitaxial growth in pulsed laser deposited iron chalcogenide thin films” Sci. Rep., vol. 5, 2015.

[75] “Pulsed laser deposition- Wikipedia,” [Online]. Available: https://en.wikipedia.org/wiki/Pulsed_laser_deposition.

[76] M. Iebole et al., “Fe(Se,Te) Thin Films Deposited through Pulsed Laser Ablation from Spark Plasma Sintered Targets” Materials, vol. 17, no. 11, 2024.

[77] M. Hÿtch et al., “Quantitative measurement of displacement and strain fields from HREM micrographs”, Ultramicroscopy, vol. 74, pp. 131-146, 1998.

[78] A.Vannozzi and e. al, “Epitaxial Zr-doped CeO_2 films by chemical solution deposition as buffer layers for Fe(Se,Te) film growth”, Superconductor science & technology, vol. 33, 2020.

[79] A.M. Sanchez et al., “Quantitative Strain Mapping Applied to Aberration-Corrected HAADF Images”, Microscopy and Microanalysis, vol. 12, p. 285–294, 2006.

[80] D. Torsello et al., “Proton Irradiation Effects on the Superconducting Properties of Fe(Se,Te) Thin Films”, IEEE Transactions on Applied Superconductivity, vol. 32, no. 4, pp. 1-5, 2022.

[81] K. Harada, “Interference and interferometry in electron holography” Microscopy, vol. 70, pp. 3-16, 2021.

[82] R. Dunin-Borkowski et al., “Off-axis electron holography of magnetic nanowires and chains, rings, and planar arrays of magnetic nanoparticles” Microsc Res Tech, vol. 64, pp. 390-402, 2004.

[83] F. Genz et al., “Advanced double-biprism holography with atomic resolution,” Ultramicroscopy, vol. 145, pp. 1-6, 2014.

[84] M. K. Wu et al., "Superconductivity at 93 K in a new mixed-phase Y-Ba-Cu-O compound system at ambient pressure" Phys. Rev. Lett, vol. 58, pp. 908-910, 1987.

[85] R. Wheeler et al., "Columnar defects in $YBa_2Cu_3O_{7-\delta}$ induced by irradiation